Cellulose biomaterials for bone tissue engineering

Maxime Leblanc Latour

A thesis submitted in partial fulfillment of the requirements for the degree of Doctor of Philosophy in Physics.

Department of Physics
Faculty of Science
University of Ottawa
Ottawa, Canada

Dédié à Éli Latour,
Ne cesse jamais d'être curieux

Abstract

Designing artificial tissue is an essential part of modern-day medicine. This is also true for bone tissue repair. Work presented in this thesis shows the steps and development of novel cellulose-based biomaterials for bone tissue engineering (BTE). Cellulose is used as the core component in these biomaterials. This work begins with an overview of the thesis, followed by a background review of the relevant biological and physical concepts. Thereafter, original research on the biomechanical properties of apple-derived cellulose are carried out *in vitro* and *in vivo*. Afterward, relevant physical forces are applied to the same type of material, to investigate the osteogenic response. Finally, cellulose nanofibrils were chemically modified to create scaffolds through UV crosslinking. These were mechanically characterized and used as scaffolds for osteogenic cell culture. As demonstrated in this work, the use of cellulose-sourced biomaterials is certainly a promising alternative compared to the industry standard. Numerous studies have demonstrated how cellulose-based biomaterials can be employed in several branches of reconstructive medicine. However, uncertainties still exist in the application of these materials for bone tissue reconstruction such as their performance under physical stress, and in their scalability. The research presented in this thesis attempts to address these gaps in knowledge. Specifically, the results presented here show how these materials can be promising candidates for low-load BTE applications. Furthermore, it is also demonstrates that mechanosensitive pathways that regulate osteogenesis remain functional on these materials. Finally, UV-curable cellulose-derived scaffolds create a more scalable and controllable biomaterial for BTE implants, notably using light-based three-dimensional printing technologies.

Statement of Originality

At the time of submission of this thesis, to the best of author's knowledge, this work is new and original. This work was performed under the supervision of Dr. Andrew E. Pelling, who provided guidance with protocol development, experimentation, and analysis of results. Chapter 1 & 2 contains an introduction section where relevant concepts are highlighted. Chapters 3, 4, and 5 included in this work contain adaptations of manuscripts that have been submitted or published in peer-reviewed scientific journals.

Manuscript included in this thesis:

- Leblanc Latour, M., Tarar, M., Hickey, R. J., Cuerrier, C. M., Catelas, I., & Pelling, A. E. Biomechanical study of cellulose scaffolds for bone tissue engineering in vivo and in vitro. *bioRxiv* 2021.07.07.451476 (2021). doi:10.1101/2021.07.07.451476
- Leblanc Latour, M. & Pelling, A. E. Mechanosensitive osteogenesis on native cellulose scaffolds for bone tissue engineering. *J. Biomech.* **135,** 111030 (2022).
- Leblanc Latour, M., Augusto Tischer, C., L. Harden, J. & E. Pelling. Nanofibrillar Cellulose Derivative: UV curable Hydrogel and aerogel for Bone Tissue Engineering. *In preparation for submission.*

Statement of Contributions

I, Maxime Leblanc Latour, am the main author and contributor of this thesis. Chapters 1 & 2 contain a review of the physics and biology concepts relevant to this work, of which I am the sole author. Chapters 3, 4, and 5 included in this work contain adaptation of manuscripts of which I am the first author amongst collaborators. The *in vitro* experiments in Chapter 3 were designed and developed with the assistance of student Maryam Tatar with the advice of Dr. Isabelle Catelas. Dr. Charles Cuerrier and Dr. Ryan J. Hickey participated and assisted in the *in vivo* studies included presented in Chapter 3. Dr. Cesar Augusto Tischer provided guidance and help for the experimentation and analysis for the results included in Chapter 5. Concluding remarks are presented in Chapter 6, of which I am the sole author.

Contribution to other manuscripts

- Modulevsky, D. J., Cuerrier, C. M., Leblanc Latour, M., Hickey, R. J., Obhi, R.-J. K., Shore, I., Galuta, A., Walker, K. L. A., Tsai, E. C., & Pelling, A. E. Plant Scaffolds Support Motor Recovery and Regeneration in Rats after Traumatic Spinal Cord Injury. bioRxiv 2020.10.21.347807 (2022). doi:10.1101/2020.10.21.347807
- Holmes, J. T., Jaberansari, Z., Collins, W., Latour, M. L., Modulevsky, D. J., & Pelling, A. E. Homemade bread: Repurposing an ancient technology for in vitro tissue engineering. Biomaterials 280, 121267 (2022).
- Hickey, R. J., Latour, M. L., Harden, J. L. & Pelling, A. E. Designer Scaffolds for Interfacial Bioengineering. bioRxiv 2020.11.06.371278 (2021). doi:10.1101/2020.11.06.371278
- Leblanc-Latour, M., Bryan, C. & Pelling, A. E. Utilizing social media and video games to control #DIY microscopes. PeerJ Comput. Sci. 3, e139 (2017).

Patent applications & provisional patent applications

- Leblanc Latour, M., Tarar, M., Hickey, R. J., Cuerrier, C. M., Catelas, I., & Pelling, A. E. PCT/CA2020/051750 - Biomaterials for bone tissue engineering (Filed Dec 2019).
- Leblanc Latour, M., Pelling, A. E., & Tischer, C. A., US Provisional Patent Application 63/390,420 - Methods for transforming polymers into cross-linkable molecules (Filed Nov 2020).
- Holmes, J. T., Jaberansari, Z., Collins, W., Latour, M. L., Modulevsky, D. J., & Pelling, A. E. US Provisional Patent Application 63/112,712 - Porous scaffold, method of making and uses thereof (Filed Jul 2022).

Acknowledgments

First, I would like to thank Dr. Andrew Pelling. I am honored and privileged to have had the chance to be mentored by a great scientist and entrepreneur.

Un énorme merci au Dr. Charles Cuerrier de m'avoir accueilli à bras ouverts au sein du groupe de laboratoire, de m'avoir conseillé à multiples reprise.

I would also like to thank the staff, lab technicians, and professors of the Department of Physics. Special thanks to Dr. James L. Harden for all your valuable advice and teaching. Thanks also to Tama Davis, Joshua Lavigne and the entire team of the Animal Care & Veterinary Service of the University of Ottawa for their help during the animal experiments.

To all the members of the Pelling Lab, past and present, thank you for the great time we've spent together over the past years.

À ma mère, Chantal et mon père, Stéphane, les mots sont faibles pour vous remercier pour tout le support que vous m'avez apporté durant ses nombreuses années. Vous n'avez jamais cessé de croire en mes compétences et m'avez épaulé jusqu'au bout. Merci de m'avoir écouté dans les moments difficiles, vous avez toujours su m'aidé, à me relever et à voir plus clair. Merci également à mon frère William pour tout ton support et ton encouragement.

Et finalement, merci à Karina, ma conjointe. Ton support fût indispensable. Merci d'avoir cru en moi, de m'avoir conseillé et pour ta patience. Tu es une personne et une mère exceptionnelle. Merci à notre fabuleux garçon Éli d'être dans nos vies. Ton sourire, ton intelligence et ta curiosité sera toujours pour moi une source de motivation.

Table of Contents

List of Abbreviations

- 3D (Three-dimensional)
- ALP (Alkaline phosphatase)
- ANOVA (Analysis of variance)
- ARS (Alizarin red s)
- BCIP/NBT (5-bromo-4-chloro-3'-indolyphosphate/nitro-blue tetrazolium)
- BMP (Bone morphogenic protein)
- BTE (Bone tissue engineering)
- $CaCl_2$ (Calcium Chloride)
- CAD (Computer-assisted design)
- CLS (Confocal laser scanning)
- CM (Culture media)
- CNF (Cellulose nanofibril)
- DAPI (4′,6-diamidino-2-phenylindole)
- DLP (Digital light processing)
- dH2O (Deionized water)
- DMAc (Dimethylacetamide)
- DMSO (Dimethyl sulfoxide)
- ECM (Extracellular matrix)
- EDA (Ethylenediamine)
- EDC (1-ethyl-3-(3-dimethylaminopropyl) carbodiimide hydrochloride)
- EDS (Energy-dispersive spectroscopy)
- EPI (Episcopic)
- FTIR (Fourier-transform infrared spectroscopy)
- GMA (Glycidyl methacrylate)
- GTC (Goldner's Trichrome)
- H&E (Hematoxylin and eosin)
- HAP (Hydroxyapatite)
- hIPSC (human induced pluripotent stem cell)
- hMSC (Human mesenchymal stem cell)
- HP (Hydrostatic pressure)
- Hz (Hertz)
- LAP (Lithium phenyl-2,4,6-trimethylbenzoylphosphinate)
- LiCl (Lithium Chloride)
- LIPUS (Low intensity pulsed ultrasound)
- mCNF (Methacrylated nanofibrillar cellulose resin)
- MSC (Mesenchymal stem cell)
- N (Newton)
- NHS (N-hydroxysuccinimide)
- NMR (Nuclear magnetic resonance)
- OM (Osteogenic inducing media)
- Pa (Pascal)
- PBS (Phosphate buffered saline)
- PCL (Poly (ε-caprolactone))
- PEGDA (Polyethylene glycol diacrylate))
- PGA (Poly (glycolic acid))
- PLA (Poly (lactic acid))
- PLGA (Poly(lactic-co-glycolic acid))
- pNPP (p-nitrophenyl phosphate)
- ROI (Region of interest)
- SDS (Sodium dodecyl sulfate)
- SEM (Scanning electron microscopy)
- SEM (Standard error of the mean)
- TCP (Tricalcium phosphate)
- TEA (Triethylamine
- Tosyl (p-toluenesulfonyl chloride)
- UV (Ultraviolet)
- VK (Von Kossa/Van Geison)
- YM (Young's Modulus)
- α-MEM (Minimum Essential Medium)

List of Figures

Chapter 1:

Overview

In the event of a major injury or trauma, external graft could be required to help regeneration of damaged bone tissues. Significant bone defects could leave, if untreated, to the non-union of the bone tissue[1]. Thus, surgical intervention is required to enhance and guide bone tissue regeneration. Several techniques were developed over the past years to overcome this challenge, reduce operative cost and patient-related pain. This field of creating and investigating new materials for treatment of damaged bone tissue is referred as *Bone Tissue Engineering* (BTE). The principles of BTE are based on symbiotic relationship between cell biology, material engineering and biological physics. These principles are aimed to optimize regeneration of damaged bone tissue, provide adequate support during recovery, and accelerate healing. Importantly, BTE designed grafts are aimed to guide osteogenic cells, promote *de novo* bone tissue formation, and accelerate overall bone reconstruction upon implantation. The ideal biomaterial for BTE is conceived to be biocompatible, trigger little to no immune response, and have osteoinductive and osteoconductive properties. Furthermore, BTE grafts should be designed to allow vascularisation of the bone tissue, to favor cell attachment, nutrient transport, and achieve good mechanical stability. BTE grafts are designed to be either degradable or to reside permanently within the body.

The objective of this thesis is to present the development, experimentation, and use of new type of materials for BTE, fabricated from cellulose. Cellulose is a widely available polysaccharide with interesting mechanical characteristics. Its potential use for BTE applications could be, in the future, a low-cost alternative to treat bone-tissue related injuries. In the past decade, cellulose-based materials were used to create scaffolds for hosting cell culture, targeted tissue engineering and *in vivo* implants[2–20]. Following similar approach to biomaterial design, the work presented in this thesis further explore and characterise natively derived cellulose as biomaterial applied for BTE applications *in vitro* and *in vivo*.

Chapter 2: The objective of the first chapter is to present background information and introduce key concepts relevant in this work. Notions of biology relevant to bone tissue engineering are presented. Then, a review of biomaterials currently used for BTE is presented.

Chapter 3: The objective of chapter 3 is to is to provide the reader with a background review of relevant physics and biophysical concepts that are important for the following chapters. Moreover, a brief review of the tools and techniques used in the following chapters is also presented.

Chapter 4: Previous studies have shown that plant-derived cellulose can be used as a scaffold for cell culture, tissue replication, and *in vivo* scaffolds. Moreover, a recent study showed the application of plant-derived cellulose specifically for bone tissue engineering. Following the hypothesis that plant-derived cellulose can be utilised as a scaffold for bone tissue engineering, this chapter further studies the biomechanical aspect of plant-derived cellulose scaffolds for bone tissue engineering in vivo and in vitro. The aim of chapter 4 to is provide a more in-depth analysis of cell differentiation within the scaffolds and the changes in mechanical properties *in vitro* and *in vivo*. Results revealed that a discrepancy in mechanical properties exist between natively derived cellulose scaffolds and bone tissues, which may limit their use to low or non-load bearing applications. The following chapter further explores the use of plant-derive scaffolds, in a dynamic environment.

Chapter 5: The representation of environmental parameters is essential for the optimal performance of a biomaterial implant. Moreover, bone tissue is a dynamic environment where the transmission of forces due to the movement of the musculoskeletal system has a direct impact on the bone cells, their differentiation, and the mineralization of the extracellular matrix. The aim of this chapter is to measure changes in relevant osteogenic makers by applying biologically relevant forces on cell-seeded, plant-derived cellulose scaffolds. This was achieved by means of oscillating hydrostatic pressure *in vitro* on cell-seeded scaffolds. These results provided further evidence for the use of plant-derived cellulose scaffolds in BTE applications. Overall, results

revealed that the combined effect of oscillating hydrostatic pressure with osteogenic-inducing media increases the density of differentiated cells, an upregulation of alkaline phosphatase activity and an increase in scaffold mineralization. This shows that well known mechanosensitive pathways cells which regulate osteogenesis remain functional on plant-derived cellulosic biomaterials.

Chapter 6: An ideal biomaterial should adapt to the surrounding environment, the functions, and the shape of the tissue which it aims to regenerate. Recent developments in rapid prototyping and three-dimensional printing allow the production of complex geometries and potentially replicating tissues at scale. The aim of this chapter is to demonstrate the fabrication steps and the analysis of the physical characteristics of a UV-curable resin derived from cellulose nanofibers. The study of the mechanical properties reveals that the elasticity of the resulting hydrogel can be modulated with UV exposure. Aerogels can be created by a freeze-drying process, creating a porous structure. These aerogels were used as a scaffold for the culture and differentiation of pre-osteoblast cells. The results revealed a marked increase in the mineralization of the aerogels after 4 weeks of incubation in an osteogenic medium. This chapter not only demonstrates the properties of this UV-curable cellulose derivative, but also its application as a resin for 3D printing hydrogels, as well as a potential biomaterial for BTE applications.

Chapter 2:

Introduction, Background and Rationale

2.1. Bone biology

Bones provide structure, mechanical support and protect vital organs. They are essential for limb movement, structural support, organ protection and locomotion. They differentiate from other tissue by their stiffness and hardness and have unique mechanical properties that ensure mechanical integrity in vertebrate animals. Moreover, bone tissue plays an essential role in regulatory homeostasis, such as plasma mineral content and hematopoietic cells production. Hematopoiesis occurs within bone tissue. Bone tissues also act as a reservoir for essential minerals, such as calcium and phosphorus. Structurally, bones are composed of an elastic organic matter phase and a rigid, brittle inorganic phase. The combination of the organic and inorganic phases give rise to the unique mechanical properties of bones. Bone tissue is a dynamic environment where stress-responsive cells influence the addition, removal, and renewal of extracellular matrix (ECM).

2.1.1. Organic and Inorganic composition

Bone tissue is a combination of organic and inorganic content. This combination represents about 30% organic content, about 60% inorganic content, with the remaining 10% consisting of water[21–24]. The predominant component in the organic phase of bone tissue is type I collagen, representing around 90% of the total organic content, arranged in fibrillar structure[21–23]. The role of collagen fibrils is to provide elasticity and mechanical strength, resisting tensile forces[21,23]. Collagen fibrils are joined together to form a solid fiber. The fibers are assembled linearly and parallelly. Between the fiber bundles, gaps are present. These gaps will become sites of mineralization of the bone tissue[21–24] (Figure 2.1). The remaining organic component include non-collagenous proteins, glycoproteins, proteoglycans, glycosaminoglycans cytokines and growth factors. Non-collagenous proteins play an important role in bone matrix organisation, metabolic regulation, and bone mineralization, such as osteocalcin, osteonectin, osteopontin and bone sialoprotein[21,23,24]. Growth factors contribute to the metabolism, differentiation, and

development of bone tissue[24]. These include the family of bone morphogenic proteins (BMPs), transforming growth factor-β and insulin-like growth factor[1,24].

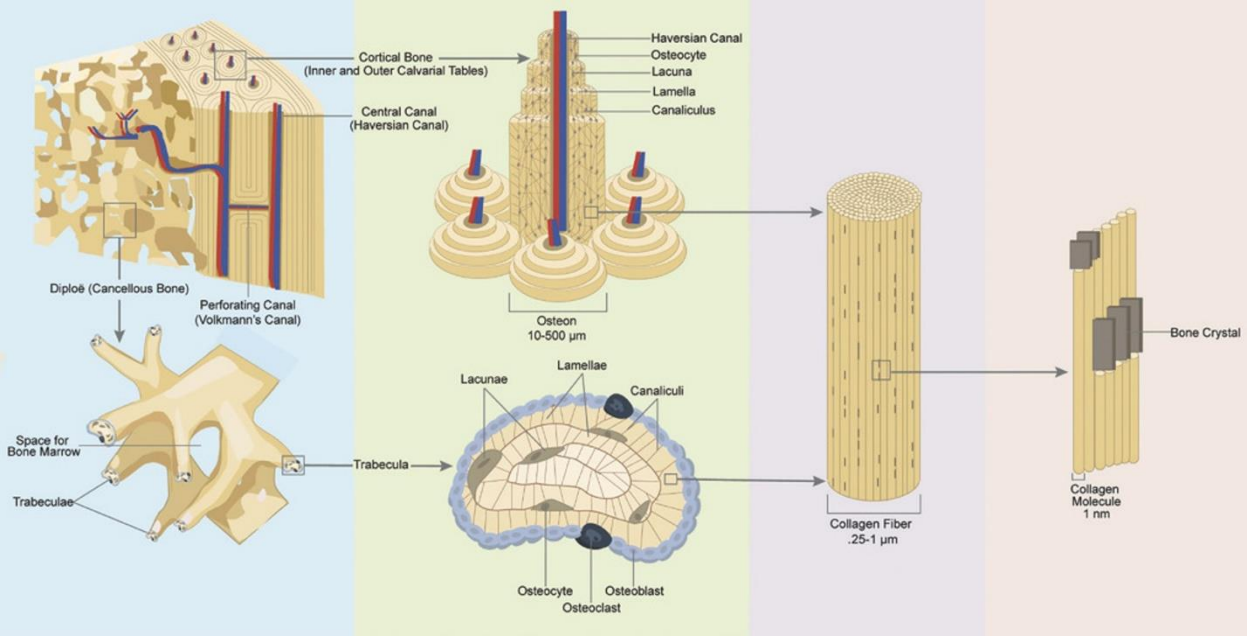

Figure 2.1: Microscopic organisation of bone tissue, illustrating trabecular and cortical bone, cell disposition and mineralised collagen fiber at different scale. Adapted with permission from[21].

The other important component of the bone matrix is the inorganic phase. Its main components are calcium and phosphate[21–24]. These ions form hydroxyapatite crystals ($Ca_{10}(PO_4)_6(OH)_2$) in the spaces between the collagen fibrils in the early stages of bone formation[21–23]. These crystals are 2 to 5 mm in thickness and 20 to 50 mm long, in the form of discrete plates between the fibrils[21,24] (Figure 2.1). Other constituents are, in smaller quantities, Carbonate, Sodium, Potassium, as well as traces of certain metals including magnesium, iron and zinc[21,22]. In addition to providing bone with hardness and resistance to compressive forces, the organic phase of the bone matrix also stores calcium, phosphorus, sodium, potassium, and other mineral ions in the human body[21,23].

2.1.2. Bone structure and organisation

The human skeleton is made up of different types of bones: flat bones (e.g., parietal, occipital), long bones (e.g., femur, tibia, humerus), irregular bones (vertebrae, maxilla), short bones (e.g., carpus) and sesamoid bones (e.g., patella)[25]. Within each bone type, at a lower scale, there are two types of bone structure in the adult skeleton: trabecular bone and cortical bone (Figure 2.1). Trabecular bone is found in the center of flat bones, as well as at the ends of long bones (epiphyses and metaphysis)[23,25]. This type of bone is porous, forming an interconnected mesh with a 50% to 90% porosity[25]. Red bone marrow is found inside the pores[23,25]. Trabecular bone has important hematopoietic and blood supply functions for the bone[23,25]. A cross section of the trabecular bone shows its organization (Figure 2.1). Trabecular bone is structured in lamellae. These consist of stacked layers of thin sheets of mineralized collagen fibrils. The lamellae are arranged in parallel, forming a fine structure called trabeculae (Figure 21)[23]. Inside the lamellae are embedded osteocytes, as well as the network of canalicular lacunae[23,25] .Cortical bone is found at the periphery of bone tissue (Figure 2.1). The structure of cortical bone, unlike trabecular bone, is compact. It is also organized in lamellae. In cortical bone, the lamellae form concentric ring-like structures called osteons (Figure 2.1)[23,25]. At the center of the concentric structure there is a short canal, containing capillaries and nerve fibers, called the haversian canal (Figure 2.1)[23,25]. Each osteon is superimposed and structurally parallel to the direction of the applied force[23]. Between the osteons, dense interstitial lamellae fill the empty space, creating a compact structure. In the interior of the lamellae, in the osteons, there are embedded osteocytes, as well as the network of canalicular lacunae, through which the osteocytes communicate (Figure 2.1) [23,25]. In terms of mechanical properties, trabecular bone is much more compliant than cortical bone, having a Young's modulus of approximately 1 GPa and 20 GPa, respectively[23].

2.1.3. Bone cells

Three types of cells are integral to bone tissue: osteoblasts, osteocytes, and osteoclasts. Each of these cell types plays a role in the maintenance, formation, and regeneration of bone tissue. Osteoblasts and osteocytes are of mesenchymal stem cell origin, while osteoclasts are of hematopoietic stem cell origin[23–25].

The main function of osteoblasts is to deposit extracellular matrix. This matrix is mainly composed of type I collagen[23–26] . They also secrete other non-collagenous proteins and bone sialoprotein[24,25]. This matrix is the foundation of the osteoid, which once mineralized will form mature bone. Once the bone matrix is established, the osteoblasts will secrete several enzymes and hormones to activate the mineralization of the matrix, including alkaline phosphatase and osteocalcin[23,25]. Osteoblasts can then incorporate into the calcified matrix and become part of the bone tissue in the lacunae. These will evolve into cytoplasmic outgrowths, forming the canaliculi[23,25]. Osteoblasts embedded in the calcified matrix are referred to as osteocytes.

Osteocytes represent the vast majority of the cell population of the bone tissue[23–25]. The osteocytes communicate with each other and with the osteoblasts at the surface of the bone tissue by gap junctions through the lacuna-canaliculi network[23–25]. Osteocyte mechanosensitivity regulates bone turnover, osteoblast and osteoclast recruitment, and the secretion of cytokines and differentiation factors[23–25]. The transmission of a force felt by osteocytes is carried out by the membrane deformation of the cells, by the activation of integrin receptors[24] and by the Wnt/β-catenin mechanosensitive pathways in the lacunar-canalicular network[27]. The mechanosensitivity of osteocytes also plays a role in the metabolism of calcium and phosphate in the body[23–25].

Unlike osteoblasts and osteocytes, osteoclasts are of hematopoietic origin, emerging from the fusion of several pre-osteoclast cells, forming a large multinucleate cellular entity[23–25] . Their role is to resorb the bone tissue, in particular by dissolving the calcified matrix (hydroxyapatite) by a proton-ATPase mechanism[23–25]. By resorbing the bone matrix, osteoclasts release calcium

and phosphate, thus influencing the homeostasis of the body's mineral content[23–25]. As they resorb the bone matrix, they occupy a cavity in the periphery of the bone called the Howship's lacunae[23–25]. It is under this cavity that the bone is resorbed.

2.1.4. Bone development

Bone tissues follow two distinct patterns of formation, depending on type of bone (i.e., long or flat bone) and stage of human development (i.e., in fetus, in children or in adults). In developing foetus, long bones are formed via endochondral ossification[28].

Endochondral ossification begins in a cartilaginous matrix (hyaline cartilage) in the fetus[22,28,29]. Around the center of the cartilage matrix, chondrocytes enlarge and become hypertrophied. Subsequently, chondrocytes start secreting alkaline phosphatase (ALP) and the matrix becomes progressively calcified[22,28]. Osteoblasts are recruited through blood vessels and capillaries adjacent to the matrix, penetrating to the center. A bone collar is formed at the periphery of the cartilaginous matrix, forming what will become the diaphysis of the bone. Subsequently, the chondrocytes die and make way for osteoblasts, which take over ossification in the empty spaces left by the chondrocytes, creating the primary ossification center[22,28]. Porous (trabecular) bone tissue forms in the primary ossification center and osteoclasts are recruited, forming the medullary cavity[22,28]. At the extremities of the matrix, secondary ossification sites start to form in the space left by the chondrocytes, which will eventually become the epiphyses[22]. At the diaphysis, the medullary cavity expands, and compact bone tissue is formed at the periphery[22]. The secondary ossification sites give way to porous (trabecular) bone tissue. At maturity, the space between the diaphysis and the epiphyses narrows as the bone grows, resulting in an epiphyseal line at each end of the bone[22].

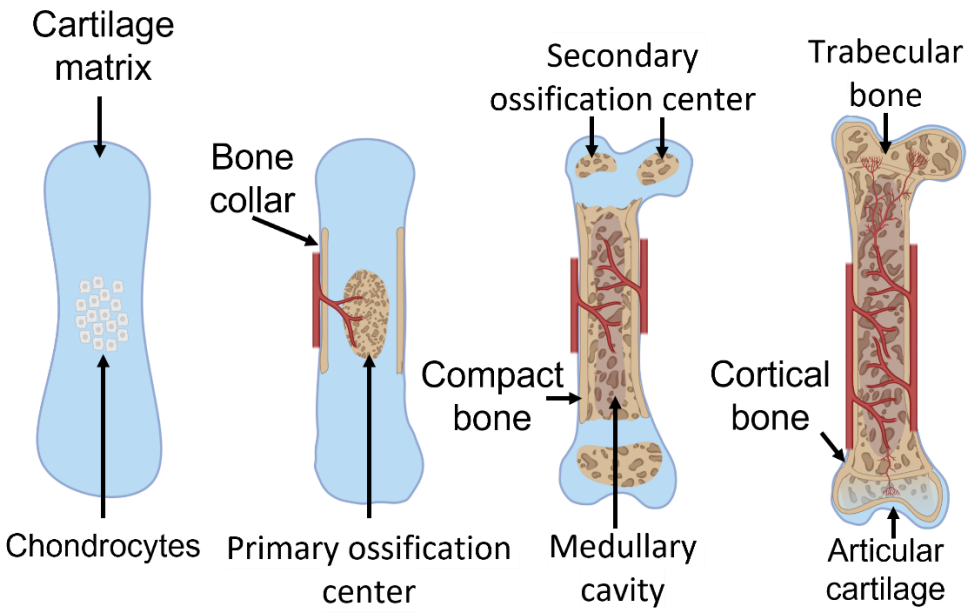

Figure 2.2: Endochondral ossification. First, chondrocytes at the center of the cartilage matrix expand, and the matrix becomes progressively mineralize. Subsequently, a bone collar is formed followed by the formation of the primary ossification center. The primary ossification center expands, forming the medullary cavity and secondary ossification at the epiphyses. Compact, cortical bone tissue is formed at the periphery of the medullary cavity. The secondary ossification sites are replaced by trabecular bone. Created with BioRender.com

The second pattern of bone formation is intramembranous ossification. Intramembranous ossification occurs in the fetal development of the cranial bones and clavicle[29]. This sequence of formation (or regeneration) is distinguished by the absence of cartilage tissue. In this process, mesenchymal stem cells condense into sheets, with blood capillaries running through them[22,28,29]. Subsequently, the mesenchymal cells differentiate into osteoblasts that will secrete a collagenous matrix[28]. Once the matrix is calcified, the osteoblasts in the center of the matrix become osteocytes, forming trabecular bone[28]. At the periphery of the bone, calcification of the matrix results in compact (cortical) bone, encompassing the trabecular portion of the bone.

2.1.5. Wolff's law and stress shielding

Bone tissue is a dynamic environment where modeling and remodeling of the tissue occurs routinely. Moreover, strain and stress on bone tissue is known to influence bone remodeling by modulating the bone density[24,25,30]. Bone tissue is highly dependent on external physical environment and thus modulate its density to accommodate for applied, or lack of, mechanical stresses. This process is referred as "Wolff's Law"[24,25,30,31]. Depending on the level of stress to which the bone is subjected, several remodeling outcomes are possible. For high and repeated levels of stress, in the limit where the bone is not fractured, we observe a gain of the bone mineral mass. In the opposite case, where stress is low or absent, a loss of bone mineral mass is observed. Osteocytes control the remodeling via mechanosensitive pathways and signaling [24,25,30]. Upon stress stimulus, cytokines and recruiting factors are sent to recruit osteoblasts and osteoclasts. Osteoblasts deposit extracellular matrix, which later mineralises to balance the effect of stress and limit strain [24,25,30]. Inversely, osteoclast resorbs bone matrix in the absence of stress (e.g., due to lack of physical exercise, injury), leaving a more fragile bone [24,25,30].

Following placement of a graft or implant to treat an injury, unwanted addition or resorption of the bone tissue can occur. This phenomenon is referred as stress shielding. Stress shielding is a manifestation where the bone density changes to correct the mechanical mismatch between the bone and the graft[32,33]. An imbalance in the stiffness between the bone and the graft at the interfaces can lead to an increase (stress hardening) or a decrease (stress softening) of the bone mineral mass surrounding the implant[32,33]. This can severely affect the implant performance and have some adverse effects, such as loosening of the implant over time and bone degradation at the interfaces.

2.2. Fracture healing

Like other tissues, bone tissue has the ability to heal itself following an injury. However, following major trauma, non-union can occur. Non-union is defined as a failure of the bone healing process in which the fracture does not fully regenerate within 6 months of injury [1,34,35]. Under normal conditions, the bone repair process occurs in several stages, and takes around 6 weeks to fully repair[1,34]. First, following the fracture, a hematoma forms around the fracture. During hematoma formation, following the coagulation cascade, osteogenic and angiogenic growth factors are released[1,34]. Inflammatory cells such as lymphocytes, macrophages and leukocytes appear in the hematoma. These in turn secrete cytokines that serve to recruit pre-osteoblast cells and stimulate blood capillary formation. There is also an elimination of damaged tissue during this stage. Subsequently, MSCs from the periosteum migrate to the fracture, forming a cellular aggregate called the granulation tissue. Angiogenesis and deposition of extracellular matrix are particularly active during this repair stage[1,34]. This is followed by the formation of a callus. Chondrocytes differentiated from MSCs deposit cartilage and become hypertrophied. This is followed by the recruitment of osteoblast progenitors, which differentiate into osteoblasts and secrete and calcify the cavities left by the hypertrophied chondrocytes[1,34]. The cartilage is gradually replaced by bone tissue, forming a hard callus. Eventually, the bony part of the callus is hardened and remodeled like healthy bone. The haversian system, as well as the lacuna-canaliculi network connecting the osteocytes are gradually restored to its near original state[1,34].

2.3. Current methodologies in Bone Tissue Engineering

Current methods for treating bone trauma include the use of autologous, allogeneic, xenogeneic, and synthetic implants[36]. Autologous implants are by far the most commonly used in orthopedic surgery to treat severe trauma resulting in bone loss and non-union of bone tissue[37]. This method, often referred to as the gold standard of implants, involves harvesting healthy bone tissue from the patient (Figure 2.3)[37,38]. Typically, this harvesting is performed primarily at the iliac

crest[37]. However, this practice has some limitations, which has motivated the use of alternative treatments. These include limitations in implant size and shape, tissue availability and morbidity[37–39]. In addition, autologous grafting procedures are prone to infection, subsequent fractures, hematoma formation at the harvest or repair site, and postoperative pain[37,40]. Allogeneic bone grafts are an alternative to autologous grafts. Allogeneic bone grafts are tissues or bone fragments harvested from a cadaver, or from a cadaver bank[37,39]. However, the disadvantages of allogeneic bone grafts are that they are prone to infection, have reduced mechanical and osteoinductive properties due to sterilization, and are more expensive than autologous implants[37]. Bone xenografts from animal bone tissue can also be used as alternative. Despite their low cost, good mechanical properties and good osteoconductivity of xenografts[37], they remain prone to infections, strong immune responses and are mostly non-osteogenic[37,39]. In addition, several ethical issues can be raised regarding the use of animal products[41]. Finally, alloplastic bone grafts, or artificial grafts, can be made from synthetic or naturally occurring material[37,39]. The use of artificially manufactured bone implants is a potential alternative to traditional methods and is intended to reduce the impact of the problems of the other types of bone implants listed above. Alloplastic biomaterials can be classified into different families: ceramics (including bone cement and inorganic materials), synthetic polymers, and polymers of natural origin (including proteins, glycoproteins and proteoglycans).

In the family of ceramics and inorganic materials, we find mainly hydroxyapatite and tricalcium phosphate (TCP)[21,37,38,42]. Hydroxyapatite is a material traditionally chosen as an alloplastic graft due to its availability, biocompatibility and composition[21,43]. Another advantage of HA is its ability to be molded, or 3D printed, and shaped to the dimensions of the implant[21]. Hydroxyapatite, and TCP, are minerals composed mainly of calcium and phosphate[37]. Hydroxyapatite, the hydrated form of apatite, has a crystalline structure, compared to TCP, which is amorphous[37]. The composition of these inorganic compounds is close to that found in human bone, which makes

these compounds interesting for use in BTE[21,37,44]. These inorganic materials have the advantage of being osteoconductive and promote osseointegration[42]. However, they show little osteogenic response[42] and have lower mechanical properties than bones, as well as a lower breaking point[44]. Due to these rather weak mechanical properties, the clinical use of HA and TCP is limited to low load applications (e.g., dentistry, maxillofacial), and as a bone filler and coating on another substrate[37,44]. These coatings can be found on metallic or synthetic implants, combined with hydrogels, or as a stand-alone material in the form of granules, porous blocks, or injectable formulations[21,37,38,42–47]. Current research on hybrid materials comprising Ca-PO_4 compounds includes collagen[48–50] and gelatin[50,51], chitosan[52–54], silk[55–57], metal coating[58–60] and polymers[61,62].

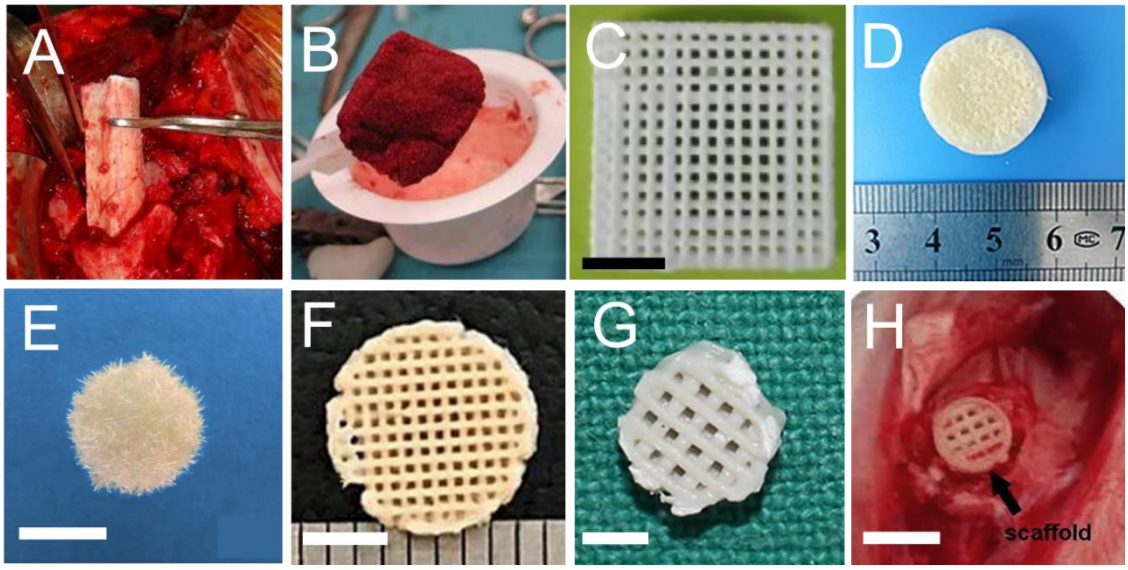

Figure 2.3: Current methodologies in bone tissue engineering research. (A) Autologous bone graft harvested from the fibula, adapted with permission from [37]. (B) Demineralized bone matrix graft, adapted with permission from [37]. (C) 3D printed tricalcium-phosphate scaffold, adapted with permission from [63], scale = 5 mm. (D) Collagen-hydroxyapatite composite scaffold cross-linked with glutaraldehyde and freeze-dried, adapted from [64]. (E) Wet-spun, non-woven Chitosan scaffold, adapted with permission from [65], scale = 5 mm. (F) 3D printed PGA-hydroxyapatite composite scaffold, adapted with permission from [66], scale = 3 mm. (G) 3D printed PLA-hydroxyapatite composite, adapted with permission from [67], scale = 2 mm. (H) 3D printed PLGA-hydroxyapatite composite in New Zealand white rabbit femoral condyle defect model, adapted with permission from [68], scale = 4 mm.

Artificially synthesized polymers are commonly used for BTE. BTE grafts from synthetic polymers come in various shape and forms, and various fabrication processes can be employed. Synthetic

polymer scaffolds can be sintered, freeze-dried, chemically polymerized, 3D printed, or UV cured[69,70]. The use of synthetic polymers has the advantages of being biocompatible with adjustable degradation rates, have the ability to be chemically modified in order to change the surface properties, and modulate the mechanical properties[69–72]. The most commonly used bone substitutes are poly(glycolic acid) (PGA), poly(lactic acid) (PLA) and poly(lactic-co-glycolic acid) (PLGA)[69,70,72]. PGA and PLA are biocompatible, FDA-approved aliphatic polyesters[70]. Their co-polymer, PLGA is also commonly used as scaffold for BTE. PGA, PLA and PLGA are degradable *in vivo*[70]. Recent studies have shown that aliphatic polyesters can be used to create porous scaffolds by 3D printing[73,74]. 3D printed PGA/Hydroxyapatite composite scaffold (Figure 2.3) were able to regenerate cranial defects up to 47% in rabbits after 8 weeks[66]. Moreover, the study reported a Young's modulus of 2.66 MPa for PGA scaffolds and up to 5.92 MPa with increasing concentration of hydroxyapatite[66]. Another group showed high viability and proliferation of human bone marrow stromal cells on 3D printed PLA scaffolds with pore size ranging from 150 to 250 µm[75]. Another group reported bone marrow stem cell proliferation and differentiation in 3D printed PLA/Hydroxyapatite composite scaffolds[67]. The group also reported a significant increase in new bone formation after 8 weeks of implantation in a rat cranial defect[67]. Porosity is known to affect the mechanical properties of 3D printed PLA scaffolds[76]. Reports shows that the Young's modulus of 3D printed PLA scaffolds range from 70 MPa to 612 MPa[76]. PLGA has the advantage of having tunable degradation rate by modulating the molecular mass of PLA and PGA in the co-polymer[74,77]. PLGA is a commonly used co-polymer for creating porous scaffolds by 3D printing[77]. PLGA/Hydroxyapatite composite scaffold was reported to promote bone regeneration in both rabbit and rat defects models[68]. Furthermore, these 3D printed scaffold were reported to have a Young's modulus of 1.7 for PLGA, and up to 1.9 GPa with the addition of hydroxyapatite[68]. Although polymers of synthetic origin present a potential of use and research for BTE, their degradation can release acidic by-products that can cause an inflammatory reaction to the surrounding tissue and decrease the efficiency of bone repair[71]. Polymers of natural origin such

as collagen, gelatin and silk, are increasingly being studied for BTE[71]. However, due to poor mechanical properties and structural stability, naturally derived materials are often used as composites with additional polymers and coatings in BTE applications[21,71,78]. Protein-derived hydrogels, such as collagen and gelatin, are used as scaffolds and drug delivery vehicles when supplemented with growth factors, bone morphogenic proteins, or hydroxyapatite [37,38,79,80]. Similar to synthetic polymers, naturally derived scaffolds can be fabricated using different techniques, such as electrospinning, sol-gel, ionic crosslinking, freeze-drying and 3D printing[81].

2.4. Cellulose for bone tissue engineering

Cellulose is widely recognized as one of the most abundant biopolymers[82]. Cellulose is a long chain polysaccharide containing thousands of D-glucose subunits[82–85]. Subunits are linearly arranged via β(1->4) glycosidic bonds[82–85] (Figure 2.4; Figure 2.5). Cellulose chains can link one another via hydrogen bonds, forming fibrillar bundles (Figure 2.4)[86]. Cellulose is a major constituent of plant cell walls, along with hemicellulose, lignin, and pectin[82,87]. These polysaccharide and organic molecule arrangement are called lignocellulosic material. In plants, lignocellulosic material of the cell wall forms the core structure of the tissue, consisting of a formation of interconnected pores, channels, or alternating layers[82,84,87]. Cellulose can be extracted and purified from trees, fruits, vegetables and plant stems. Moreover, some strains of bacteria can synthetize cellulose, without any “lignocellulosic impurities”.

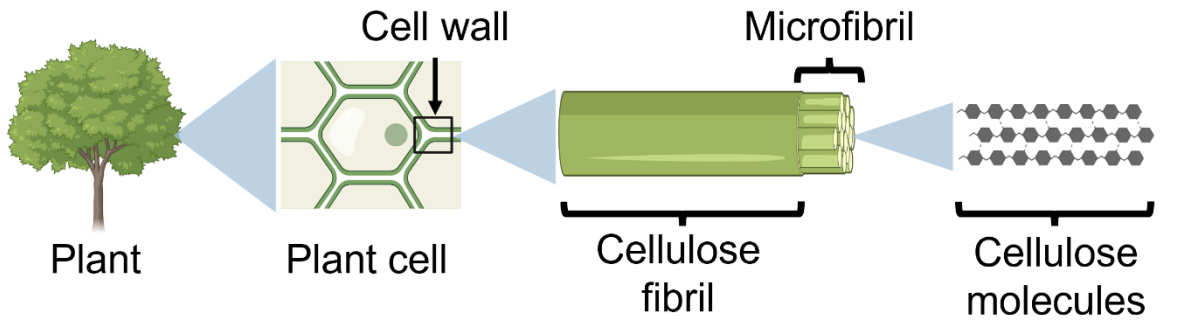

Figure 2.4: The arrangement of cellulose in plants. In plants, cell walls are made of cellulose, along with hemicellulose, lignin, and pectin. Cellulose in plant walls is linearly arranged in fibrils, composed of bundles of microfibrils. At the molecular level, cellulose microfibrils are linked together by hydrogen bonds. Created with BioRender.com

Recently, several plant-derived, cellulosic and lignocellulosic biomaterials were developed for several tissue engineering application. Due to its chemical inertness and biocompatibility, cellulose-based biomaterials are being used for applications in cell culture, soft tissue engineering, neural tissue engineering, wound healing, drug delivery and BTE[4,15–17,19,20,88–91]. Cellulose, cellulose derivatives and lignocellulosic were introduced as grafts for BTE in the past two decades[3,83,85,92]. Cellulose from bacterial origin (Figure 2.5) has the advantage of being “pure”, crystalline, easily sourced and biocompatible[3,85,92,93]. Bacteria (e.g., *Komagataeibacter* strain) secrete their biofilm, forming a network of cellulose fibers[3,85,92,93]. Bacterial cellulose shows interesting mechanical properties, rendering it suitable for BTE. Reports show pore size distribution of 1 to 300 µm, Young’s modulus ranging from 0.1 to 5.6 MPa and ultimate strength up to 47 MPa[3,93,94]. Prior to bacterial cellulose scaffold fabrication, treatment of the membrane is required. This step is usually performed with an alkaline solution to remove bacteria from the cellulose network[3]. Several methods are employed to construct scaffolds from bacterial cellulose (Figure 2.4). The bacterial film can be use directly after sterilisation, dissolved in a solution, electrospun, solvent-casted and freeze-dried[3,93,95]. Bacterial cellulose grown within wax microsphere can lead to microporous scaffolds suitable for BTE, with a reported Young’s modulus of 1.6 MPa and mean pore size of 300 µm[96]. These scaffolds were fabricated without additives

and were calcified by differentiated pre-osteoblastic cells *in vitro.* For BTE applications, components are often added to bacterial cellulose scaffolds to enhance performance. Addition of hydroxyapatite particles to bacterial cellulose can increase its rigidity, increase cell adhesion to the graft an induce osteogenic differentiation[3,93]. In vivo studies of bacterial cellulose-hydroxyapatite composite grafts in rat, dogs and rabbit bone defects models showed new bone formation and low inflammatory response[3]. Type I collagen, the principal organic constituent of bone tissue, can also be combined with bacterial cellulose to promote osteogenesis[93]. Other bone-related protein can be added to bacterial cellulose, such as BMP-2. Group have shown that bacterial-cellulose/BMP-2 composite can increase scaffold mineralisation, ALP activity and promote osteogenesis[93]. Plant-derived cellulose is also studied as a material for BTE. Similar to cellulose of bacterial origin, plant-sourced cellulose scaffolds were used as standalone scaffolds and in composite with additives to enhance performance[83,85,97]. Cellulose from cotton pulp was used to create hydrogel scaffolds for BTE[98]. Reported results shows proliferation of MG-63 cells of the scaffolds, with significant improvement by cross-linking gelatin to the scaffold with citric acid[98]. Another group have incorporated PLA to hydrolyzed cotton pulp to create a nanocrystalline-cellulose/PLA composite[99]. Their freeze-dried method yielded a highly porous scaffold (~80% porosity) and a Young's modulus in the vicinity of 200 MPa[99]. Cellulose nanofibrils (CNF) from wood pulp are another plant-sourced cellulose used in BTE. CNFs are created by mechanical separation of cellulose, resulting in fibrils ranging between 2 and 100 µm in diameter[90]. CNFs can be derived into biocompatible hydrogels or used as composites for BTE application[90]. Proteins can be added to CNF hydrogels to enhance mechanical stability and osteogenic performance[85]. Another advantage of CNF is their usability as 3D printing "ink"[85]. CNF/Alginate composite was used as hydrogel for BTE, by "printing" scaffolds in various shapes, such as cubes, cylinder and bone[100]. This particular CNF composite was reported to have strong mechanical properties, with tunable Young's modulus as a function of concentration of alginate in the mixture, ranging from 135 MPa, up to 1511 MPa[100]. Other group reported the fabrication

scaffolds by means of lyophilisation of CNF-based hydrogels[85]. Recent research using directional freezing of CNF hydrogels showed tunable porosity in the scaffolds[101]. This technique yielded scaffolds with Young's modulus ranging from 0.45 to 50.75 MPa with mean pore diameter from 0.5 to 60 μm[101]. Furthermore, authors reported attachment and proliferation of osteosarcoma-derived cells into the scaffolds[101].

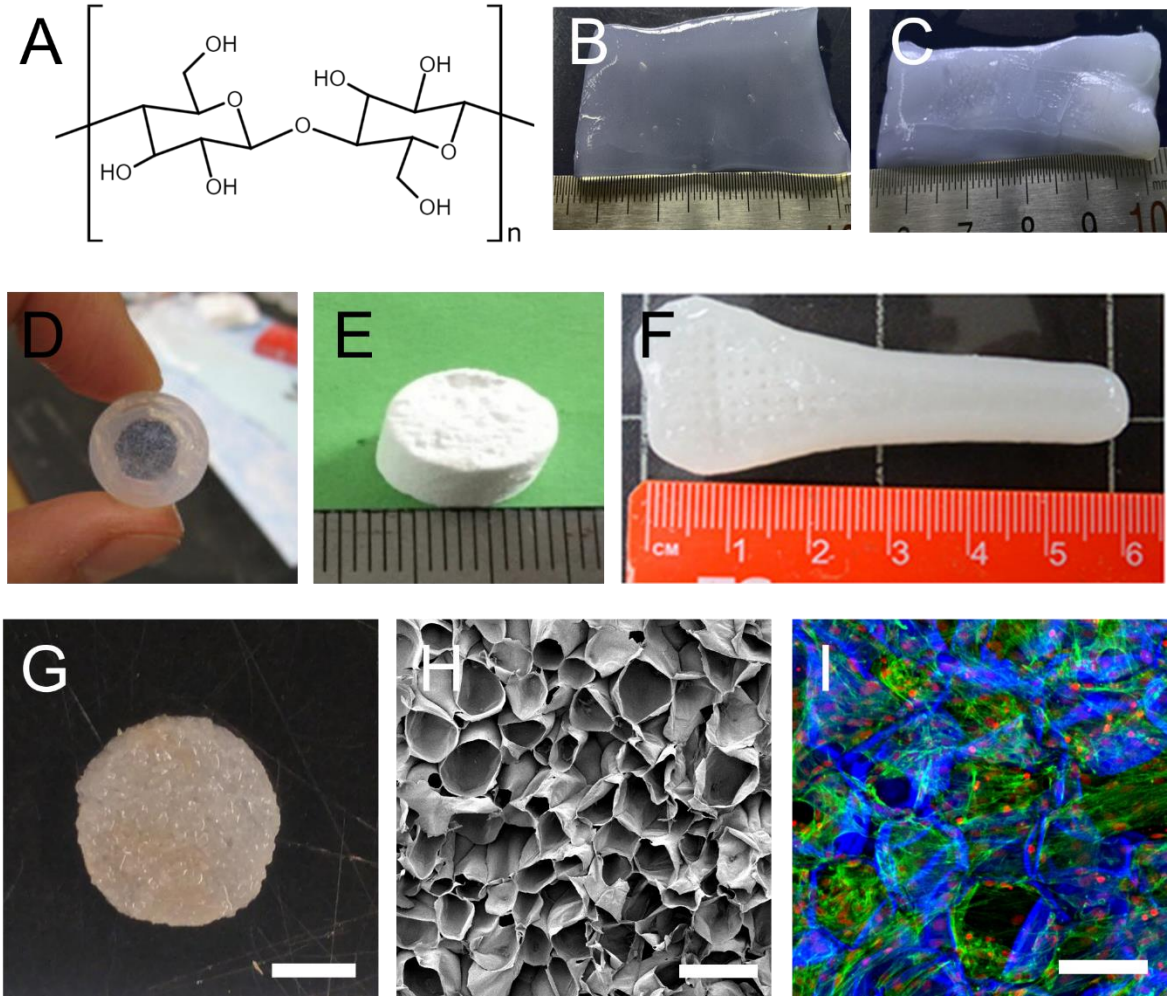

Figure 2.5: Cellulose and its uses in bone tissue engineering. (A) Cellulose chemical structure. (B) Bacterial cellulose membrane and (C) bacterial cellulose-hydroxyapatite composite membrane for BTE, adapted with permission from [102]. (D) Microporous bacterial cellulose scaffolds, adapted with permission from [96]. (E) Cellulose-PLA composite scaffold, adapted with permission from [99]. (F) 3D printed cellulose-alginate scaffold, adapted with permission from [100]. (G) Disk-shaped decellularized apple scaffold, scale = 2 mm. (H) Scanning electron microscope image from decellularized apple scaffold cross-section, scale = 100 μm. (I) Confocal laser-scanning microscope image showing decellularized apple scaffold (Blue) with proliferating MC3T3-E1 pre-osteoblastic cells (red and green are showing cell nuclei (DNA) and actin filaments, respectively), scale = 200 μm.

Another alternative to create plant-derive scaffolds is by utilising directly the natural cellulosic matrix of plants (Figure 2.4). Researchers have derived methods to remove cells and components from the cell wall with surfactants, leaving an empty matrix[4,15–17,19,20,91]. This method allows researchers to take advantage of the naturally occurring patterns and pore structure in plants, fruits and vegetables to create scaffolds with matching architecture of the targeted tissue[17]. This biomimicry approach was used in soft tissue engineering for *in vitro* and *in vivo* study of plant-derived cellulose scaffolds[15,16,20]. These groups developed scaffolds by treating fruits and vegetable tissues with a sodium dodecyl sulfate solution to remove plant cells, DNA, lipids and proteins[15,16,20]. Cell proliferation was observed in apple-derived and spinach-derived scaffolds, using myoblasts, fibroblasts, epithelial and stem cells[16,20]. Biocompatibility and blood vessel formation was observed after 4 and 8 weeks of subcutaneous implantation of apple-derived scaffolds in mice[15]. Hickey et al. demonstrated that treating the scaffold surface with a calcium chloride solution after decellularization improves cellular viability[17]. Furthermore, treatment of plant-derived cellulose scaffolds with proteins, peptides or minerals can increase cell viability, proliferation and adhesion[17,19]. Recently, research groups have employed plant-scaffolds, notably apple tissue, to generate bone-like tissues *in vitro*[4,91]. In one particular study, it was found that apple-derived scaffolds were the most suitable for the culture of human induced pluripotent stem cells (hIPSCs) and differentiation towards osteogenic linage[4]. Apple-derived scaffolds were the first plant-derived scaffold employed in tissue engineering applications. With interconnected pores ranging from 100 to 200 µm in diameter[4,16], apple-derived scaffolds share a very similar architecture to trabecular bone tissue (Figure 2.5).

Chapter 3:

Review of physical concepts & techniques

3.1. Motivation

Proper understanding of mechanical characteristics is of paramount importance in the design of materials for biomedical applications. In the field of BTE, the response to biological and external stresses, such as load bearing in bone tissue, cyclic loading, or stretching, can influence the cellular response and thus the success of the implant[32,103]. The concepts of material stiffness (or compliance), strength, and toughness should be considered when designing a biomaterial, and ideally the mechanical characteristics of the material should closely match those of the surrounding tissue[32,104]. Here a review of the basic mechanical concepts used in the following chapters is presented.

3.2. Linear elasticity

The elasticity of a material is defined by the linear deformation of a material under the effect of a force[105]. For most materials known as "elastic", we observe, during small deformation, a linear relationship between the force exerted and the resulting deformation. For example, when stretching a simple rubber band, the return force is becoming greater as the elastic is stretched. When it is released, it returns to its original length. This linear elasticity of materials is expressed by Hooke's law. This law relates the stretching (or compression) force of an object to its change in dimension in a proportional way. When a massless spring is stretched (or compressed) within the limits of linearity (i.e., small displacements), the response will be a force proportional to the total elongation[104,105]. This linear relationship, Hooke's law, can be expressed as follows:

$$F = kx \tag{1}$$

Where F is the force resulting from a deformation of distance x of an ideal spring with constant k. The constant of proportionality k expresses the capacity of a material to resist a deformation

(i.e., the "stiffness"). The vast majority of so-called "elastic" materials will obey Hooke's law, if their deformations remain small. Contrary to ideal springs, physical objects have a particular mass and shape. However, if they are subjected to small deformations, they can behave like "Hookean" springs. Let us take the example of an object of length L and cross-sectional area A, fixed at one end, under the effect of a force F (Figure 3.1). The small elongation x of the object is caused by a force F proportional to its surface area[105]. Real-life materials with arbitrary mass and shape will exhibit similar "Hookean" behavior when the applied force, deforming the material, is relatively small (i.e., in the linearity limit[105]). We can represent an arbitrary object as a set of N "Hookean" springs of constant k and section A (Figure 3.1). The force required to extend (or compress) this object is therefore:

$$F = Nkx \tag{2}$$

One can thus define the average force (or stress) per unit area as $\sigma = \frac{F}{A}$, for the whole object. As the force must be uniform at any point in the object, the stress must also be uniform[105].

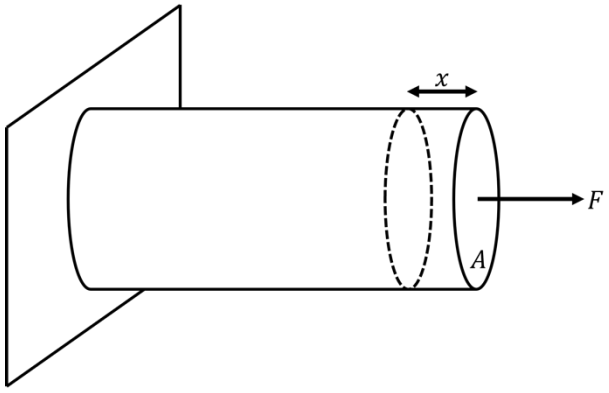

Figure 3.1: Cylindrical object of surface area A, fixed at one end and elongated to x by a force F.

Therefore, a small piece within the object will be deformed in proportion to its size. One can thus define the extension of the whole object (or strain) as $\varepsilon = \frac{\Delta L}{L_0}$. The relationship between stress and strain of the whole object is defined as:

$$\sigma = E\varepsilon \tag{3}$$

Where σ is the stress, ϵ is the strain (or deformation) and E is defined as the Young's Modulus of the object[105]. In general, for a real-life material, we can write the stress (σ), as a tensor, encompassing all the directions of stress[105]:

$$\{\sigma_{ij}\} = \begin{pmatrix} \sigma_{xx} & \sigma_{xy} & \sigma_{xz} \\ \sigma_{yx} & \sigma_{yy} & \sigma_{yz} \\ \sigma_{zx} & \sigma_{zy} & \sigma_{zz} \end{pmatrix} \tag{4}$$

Where $\{\sigma_{ij}\}$ is the Cauchy's stress tensor, and the indices i and j represents the direction of the force and the normal direction of the surface upon which the force is acting (Figure 3.2), respectively. The diagonal elements of the matrix ($i = j$) represents are compressive or tensional stress while the off-diagonal elements ($i \neq j$) represents sheer stress. The positive sign of $\sigma_{i=j}$ correspond to a tension force acting on surface element dS_i.

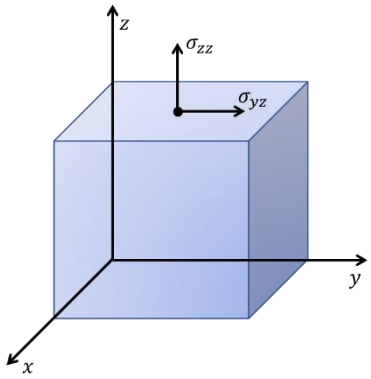

Figure 3.2: Cubic object with stress components acting σ_{zz} and σ_{yz} on surface element dS_z.

One can thus define an element of force dF_i acting on a surface element dS_i as[105]:

$$dF_i = \sum_j \sigma_{ij}\, dS_i \tag{5}$$

For deformable materials, stress will cause displacement. For small displacements, the information can be described by the Cauchy's infinitesimal strain tensor (or symmetrized displacement gradient tensor) as[105]:

$$\epsilon_{ij} = \frac{1}{2}(\nabla_i \epsilon_j + \nabla_j \epsilon_i) \tag{6}$$

For diagonal element in the strain tensor ($i = j$), the strain elements simply reduce to $\epsilon_{i=j} = \nabla_i \epsilon_i$, and the off-diagonal elements ($i \neq j$) to $\epsilon_{ij} = \epsilon_{ji}$. For isotropic deformable materials, we can thus re-write Hooke's law accounting for off-diagonal stress elements as[105]:

$$\sigma_{ij} = 2\mu\epsilon_{ij} + \lambda\delta_{ij}\sum_k \epsilon_{kk} \tag{7}$$

Where μ and λ are *Lamé* coefficients, representing the sheer modulus of the material and acting analogously as an elastic modulus, respectively, and δ_{ij} is the Kronecker delta. Deformation along one direction will cause the material to contract (or expand) in the perpendicular direction of the strain. The material's parameter that describes this behavior is called the ***Poisson's*** ratio[105]:

$$\nu = -\frac{\epsilon_{xx}}{\epsilon_{zz}} = -\frac{\epsilon_{yy}}{\epsilon_{zz}} \tag{8}$$

Assuming a uniform stretching in z of cube shape (Figure 3.2), of Young's Modulus E, due to force (e.g., as uniform pressure on surface) $F = P \cdot S$. Assuming the only force acting on the system is $\sigma_{zz} = \frac{F}{S} = P$, with all the other components of the stress tensor vanishing, one thus finds: $\epsilon_{zz} = \frac{\sigma_{zz}}{E} = \frac{P}{E}$; $\epsilon_{xx} = -\nu\epsilon_{zz} = -\frac{\nu P}{E} = \epsilon_{yy}$. With all the off-diagonal elements of the strain tensor vanishing. By using the general expression for Hooke's law (eqn. 3), one can thus write the Poisson's ratio and Young's modulus as a function of the *Lamé* parameters[105]:

$$E = \mu \frac{3\lambda + 2\mu}{\lambda + \mu} \quad (9)$$

$$\nu = \frac{\lambda}{2(\lambda + \mu)} \quad (10)$$

3.3. Hydrostatic pressure

Bones are constantly stressed by environmental factors. Locomotion and daily activities induce pressure throughout the musculoskeletal system. The pressure within long bones found can reach up to 18 MPa[106]. In the lacuna-canaliculi network of bones, these forces and stresses are transmitted to osteocytes via Wnt/β-catenin mechano-sensing pathways[27], with pressure inside the network observed to be around 280 kPa[107]. The impact of pressure on bone and bone cells is therefore an important aspect to consider for BTE. Different approaches were studied to measure the impact of stress and forces on the performance of biomaterials[108,109]. One approach is to modulate the pressure of the gas phase of bioreactor, to induce a change of hydrostatic pressure of incubation media[110–116]. More details on this approach are given in Chapter 4. In the example of a closed cylinder, filled with media (Figure 3.3), the hydrostatic pressure (at depth h in the media) can be defined as[105]:

$$P = \rho g h + P_0 \quad (11)$$

Where P is the pressure within the media, ρ is the density, g is the gravitational acceleration, h is the distance between the depth and the surface, and P_0 is the pressure above the surface.

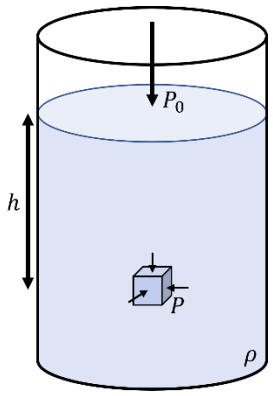

Figure 3.3: Hydrostatic pressure representation in a closed cylinder filled with media of density ρ. A volume element at distance h from the surface is under pressure P. The surface of the media is under uniform pressure P_o.

In the case of bioreactor used for BTE (see Chapter 4), one can estimate that ρgh is small relative to P_0. One can estimate that the pressure in the media $P \approx P_0$ in equation (11). In Chapter 5, the relevant forces acting on bone tissue are simulated for biomaterials using a custom-made bioreactor. For this particular bioreactor, the gas phase above the culture medium is compressed. We can estimate that the cell culture medium behaves like water, thus incompressible under the effect of a force[105]. This has the effect of translating the pressure of the gas phase into hydrostatic pressure within the culture medium. The cells under study are thus stimulated by this force ($P \approx P_0$).

3.4. Rheology

The origin of the word rheology is the combination of ancient Greek words *rhéo* and *lógos*, meaning "flow" and "under study", respectively[117]. In modern terms, one can define *rheology* as the study of a material “flowing” response due to an applied stress. In this context, “flowing” is a representation of the object’s deformation. As demonstrated in the previous section, real-life material behavior under stress is intrinsically dependant on the elastic modulus, the Poisson’s ratio and direction of applied force, either tension, compression, sheer or a combination of all three. However, this holds true for “purely elastic” materials only. Materials, especially biological

matter, will in fact respond under stress with a symbiotic combination of elastic (conservative) and viscous (dissipative) components. For purely elastic solids under applied strain only (e.g., where $\sigma_{yz} \neq 0$ and all other component of the stress tensor are 0; Figure 3.4), the material will deform elastically following Hooke's law[117]:

$$\sigma = G\gamma \tag{12}$$

Where G is the shear modulus and γ is the strain under sheer. Here, γ is simply the ratio to which the surface displaces with respect to its height ($\frac{d}{h}$). Analogously, for purely viscous "solids" (fluid to be precise), the stress can be described as a function of the *sheer rate*[117]:

$$\sigma = \eta\dot{\gamma} \tag{13}$$

Where η is the viscosity of the material and $\dot{\gamma}$ is the applied sheer rate. This stress-sheer rate relationship is called *Newtonian*, is valid for materials in which their viscosity is independent of the sheer rate[117].

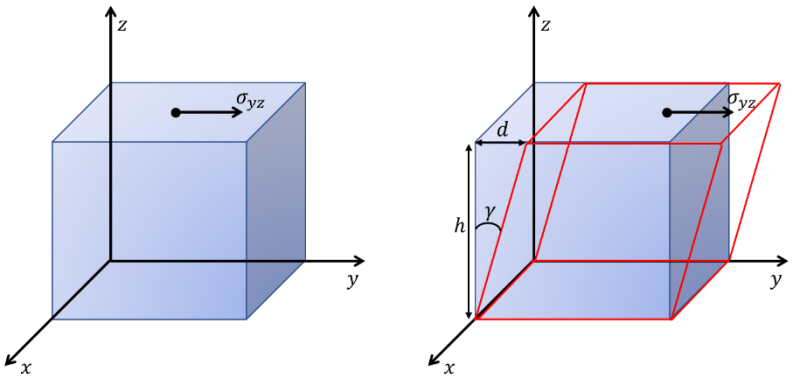

Figure 3.4: Cubic object of height h is sheared by stress σ_{yz} up to distance d. The shear strain of the object is defined by γ.

It is important to note that both Hookean and Newtonian relationship of stress are linear behaviors. On the other hand, *non-Newtonian* materials where η is dependent on $\dot{\gamma}$, interesting behavior can be observed such as *shear-thinning* materials, where the viscosity decreases as the sheer rate

increases. The opposite, s*hear-thickening* occurs with increasing sheer rate. To draw a line between linear and non-linear regimes, a viscoelastic relaxation time τ can be introduced[117]. This can be seen as a material's characteristic relaxation period when, after being subjected to stress, a material goes back to equilibrium. As real-life materials, especially biological specimens, are complex in their composition, several models were developed to characterize their viscoelastic behavior. The simplest model to describe viscoelastic fluid is the Maxwell model. This model constitutes of a spring linearly attached to a viscous damper (dashpot)[117] (Figure 3.5).

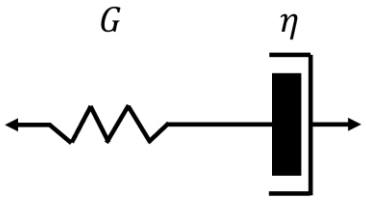

Figure 3.5: Maxwell model element consisting of a spring with elastic modulus G connected to a dashpot with viscosity η.

When attached on one end, and pulled to the other extremity, this model will elongate in series, thus the overall strain rate of the system is an addition of both components[117]:

$$\dot{\gamma} = \dot{\gamma_{viscous}} + \dot{\gamma_{elastic}} \tag{14}$$

From our definition of viscous and elastic response, we obtain the following differential equation:

$$\sigma + \frac{\eta}{G}\dot{\sigma} = \eta\dot{\gamma} \tag{15}$$

With the following solution, defining the relaxation time ($\tau = \eta/G$) for the system[117]:

$$\sigma(t) = \frac{\eta}{\tau}\int_{-inf}^{t} \dot{\gamma}(t')e^{-\frac{t-t'}{\tau}}dt' \tag{16}$$

Assuming a constant sheer rate:

$$\sigma(t) = \dot{\gamma}\eta[1 - e^{-\frac{t}{\tau}}] \tag{17}$$

A more generalized model can be viewed as a series of "Maxwell elements" arranged in parallel. The contribution of each element to the total stress is additive, with the i-th element having its own relaxation time ($\sigma(t) = \sum\sigma_i$)[117]. However, a continuum of Maxwell elements is better suited to represent the viscoelastic response of a real-life material. One can thus define a distribution function, encompassing all the relaxation times of the continuum, $H(\tau)$. Furthermore, a function dependant on $H(\tau)$ can be used to describe the shear stress relaxation modulus of the system[117]:

$$G(t) = \int_0^{inf} \frac{H(\tau)}{\tau} e^{-\frac{t}{\tau}} d\tau \tag{18}$$

Yielding to the general form of time-dependant stress of a viscoelastic material[117]:

$$\sigma(t) = \int_{-inf}^{t} \dot{\gamma}(t')G(t - t')\, dt' \tag{19}$$

Measuring $G(t)$ of a material is of great importance to understand the behavior of a material under various condition of stress and strain. Experimentally, this can be achieved using a rheometer. In an oscillating rheometer, where the sample is subjected to a rotative strain, the general stress response can be written as [117]:

$$\sigma(t) = \int_{-inf}^{t} \gamma_0 e^{-i\omega t} G(t - t')\, dt' = i\omega\gamma_0 e^{(i\omega t)} \int_0^{inf} e^{-i\omega x} G(x) dx = G^*(\omega)\gamma(t) \tag{20}$$

Here, we introduce the complex shear modulus, $G^*(\omega)$, which contains information for both conservative and dissipative components of the stress-strain response. As such, one can express $G^*(\omega)$ as a complex quantity, the real part being defined as the storage (conservative) modulus and the imaginary part as the loss (dissipative) modulus[117]:

$$G^*(\omega) = G'(\omega) + iG''(\omega) \tag{21}$$

With,

$$G^*(\omega) = i\omega \int_0^{inf} e^{-i\omega x} G(x) dx \tag{22}$$

In chapter 5 of this thesis, measuring the storage modulus with an oscillating rheometer in a plate-plate configuration gives valuable information on the cross-linking kinetics of the material and on its elastic properties.

3.5. Tools and Techniques

3.5.1. Fluorescence and confocal laser scanning microscopy

When it comes to studying biological specimens, microscopes are no doubt the most convenient tools. Over the years, several tools and advancements have been made in the light microscopy field. One major advancement for both biologist and physicist is the introduction of fluorescence microscopy. By using fluorescence microscopy, scientists can highlight a specific body within a whole specimen, using specific markers (fluorophores). For example, 4′,6-diamidino-2-phenylindole (DAPI) can be used to stain DNA and image cell nuclei. A light source (e.g., laser) with a specific wavelength (in conjunction with the target fluorophore) is focused towards a dichroic mirror (Figure 3.6) where the light is redirected through an objective. The excitation light is focused on the specimen where the fluorophore is excited to a higher energy state. When the excited fluorophore relaxes to the ground state, it emits a Stokes-shifted photon[118]. The emitted light goes back towards the objective, the dichroic mirror and through an emission filter, selecting the appropriate wavelength through the detector (Figure 3.6). The light path process is named episcopic (EPI). The EPI microscopes are useful tools for fluorescent-labeled microscopy but have some drawbacks. For instance, an EPI microscope poorly renders

three dimensional structures due to out of focus light coming to the detectors. Confocal laser scanning (CLS) microscopy was developed to overcome this issue[118]. The principle is similar to EPI microscopy, with the addition of 2 pinholes at the emission and detector. The addition of the pinhole at the emission serves to reduce the beam size in order to create point illumination[118]. The pinhole at the detector blocks all the light except the emission point in the sample. Thus, all the out-of-focus light is blocked, enhancing the signal. The laser then *scans* across the sample in a linear fashion, rendering a 2D image slice of the sample at a given focal plane. The focusing lens can be moved to change the focal plane. By collecting multiple slices of the sample, three-dimensional rendering is possible.

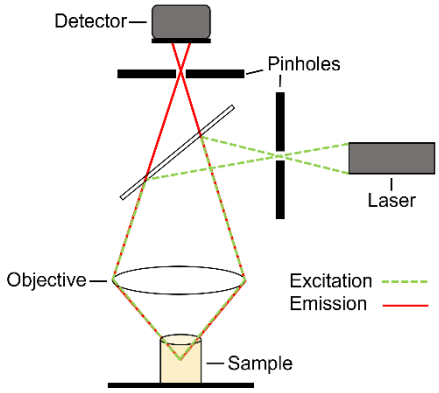

Figure 3.6: Schematic representation of components and light path in a confocal laser scanning microscope.

Fluorescent labeling of specific molecule is of great interest for biophysicists. Rendering of targeted microscopic features, such as topological features on a biomaterial and cellular density can be made in good resolution using techniques such as CLS microscopy and image processing software. Ideally, the perfect microscope is one that can resolve objects down to atomistic size (few nm). However, for light microscopes, this resolution is impossible to achieve relying simply on optics. The maximum resolution of a microscope (resolving power) is limited by the diffraction of the light that travels the path through the optical system. Thus, a microscope won't be able to resolve objects lower than the *diffraction limit* imposed by the physical assembly of its optical

system. The resolution limit (or *diffraction limit*) of microscopes was first described in the 19th century by Ernst Karl Abbe as [118,119]:

$$D = \frac{\lambda}{2NA} \tag{23}$$

where λ is the wavelength of the excitation light and NA is the numerical aperture of the optical system. The numerical aperture is defined as [118,119]:

$$NA = n \cdot sin\,(\theta) \tag{24}$$

where n is the index of refraction of the medium and θ is the maximal possible angle at which the light can enter the optical instrument. For microscopes with $NA \approx 1$ the smallest resolvable objects using blue (400 nm) light are $D \approx 200$ nm. Mammalian cells are around 30 to 100 µm in diameter[120], above the diffraction limit.

3.5.1. In vitro model

Immortalised cell lines and stem cells are commonly used as models for *in vitro* investigation. For BTE, commonly used cells include primary osteoblasts, mesenchymal stem cells (MSC), immortalised osteoblasts precursors, ST-2 cells, MLO-Y4 cells and MC3T3-E1 cells[1,26,121,122]. MC3T3-E1 (subclone 4) cells are widely used as a model to characterize bone matrix mineralization and biomineralization[26,122,123], and are the cells used for the *in vitro* models in this thesis. MC3T3-E1 are immortalised pre-osteoblasts from mice calvaria[26]. These particular cells have the ability to differentiate into osteoblasts with the addition of alkaline phosphatase and an inorganic phosphate source[26,122,123]. Upon differentiation, MC3T3-E1 can mineralize the surrounding matrix and express ALP [26,122,123], both important markers for osteoblastic differentiation and evaluation of *in vitro* performance of a biomaterial.

3.5.2. In vivo model

It is of paramount importance to use animal models that are representative of the possible use of a biomaterial. In the field of BTE, the model considered as the basic standard to evaluate the bone regeneration capabilities of a new implant is the rat critical size calvarial defect model[124]. This model consists of implanting the material to be studied in the upper part of the skull in rats. Normally, one or two circular defects are created by removing the parietal bone by trepanation (Figure 3.7).

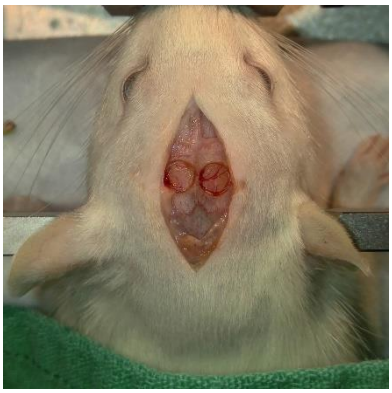

Figure 3.7: Bilateral critical size calvarial defects in Sprague Dawley rat. Circular defects (5 mm) are created on each side of the exposed parietal bones. Here, the circular bone defects have been removed, exposing the dura and the underlying brain.

A critical size defect is defined as the minimum size that a bone defect cannot regenerate by itself, without intervention, during the life of the animal[124]. In rats, a cranial defect of at least 5 mm (in diameter) is considered to be critically sized[125]. Some research groups have performed studies with critical defects ranging from 5 to 9 mm in diameter[125]. The advantage of using a 5 mm cranial defect is that it requires fewer animals to be studied, as it is possible to create two defects per animal. Also, the 5 mm defects are made only in the parietal bones, without damaging the midsagittal suture, which could affect the results[125]. Following implantation, several tests are used to evaluate the formation of new bone, usually after a period of 4, 8 or 12 weeks[124]. These results are usually compared to a control where the defect was left empty or compared to another known biomaterial[124]. A commonly used test includes histological evaluation, to assess the type of cells

present in the implant, the immunological response as well as to identify new blood vessel formation and mineralization. CT scans are also used to evaluate new bone formation. Furthermore, to evaluate the strength of the implant at the interface, a mechanical push test can also be performed.

Chapter 4:

Biomechanical study of cellulose scaffolds for bone tissue engineering in vivo and in vitro

This chapter is an adaptation of: Leblanc Latour, M., Tarar, M., Hickey, R.J., Cuerrier, C.M., Catelas, I. & Pelling, A.E. Biomechanical study of cellulose scaffolds for bone tissue engineering in vivo and in vitro. bioRxiv 2021.07.07.451476 (2021). doi:10.1101/2021.07.07.451476

This manuscript is in preparation for submission.

4.1. Motivation and Objective

Multiple studies have proven the biocompatibility and efficiency of plant-derived scaffolds for tissue engineering and, more recently, specifically to BTE. However, some questions regarding the mechanical properties of these biomaterials still remain unanswered. The objective of the present chapter to is to analyse the changes in mechanical properties and performance, *in vitro* and *in vivo* of apple-derived cellulose scaffolds applied for BTE.

4.2. Abstract

Plant-derived cellulose biomaterials have recently been utilized in several tissue engineering applications. These naturally derived cellulose scaffolds have been shown to be highly biocompatible in vivo, possess structural features of relevance to several tissues, and support mammalian cell invasion and proliferation. Recent work utilizing decellularized apple hypanthium tissue has shown that it possesses a pore size similar to trabecular bone and can successfully host osteogenic differentiation. In the present study, we further examined the potential of apple-derived cellulose scaffolds for bone tissue engineering (BTE) and analyzed their mechanical properties in vitro and in vivo. MC3T3-E1 pre-osteoblasts were seeded in cellulose scaffolds. Following chemically-induced osteogenic differentiation, scaffolds were evaluated for mineralization and for their mechanical properties. Alkaline phosphatase and Alizarin Red staining confirmed the osteogenic potential of the scaffolds. Histological analysis of the constructs revealed cell invasion and mineralization throughout the constructs. Furthermore, scanning electron microscopy demonstrated the presence of mineral aggregates on the scaffolds after culture in differentiation medium, and energy-dispersive spectroscopy confirmed the presence of phosphate and calcium. However, although the Young's modulus significantly increased after cell differentiation, it remained lower than that of healthy bone tissue. Interestingly, mechanical assessment of acellular scaffolds implanted in rat calvaria defects for 8 weeks revealed that the force required to push out the scaffolds from the surrounding bone was similar to that of native

calvarial bone. In addition, cell infiltration and extracellular matrix deposition were visible within the implanted scaffolds. Overall, our results confirm that plant-derived cellulose is a promising candidate for BTE applications. However, the discrepancy in mechanical properties between the mineralized scaffolds and healthy bone tissue may limit their use to low load-bearing applications. Further structural re-engineering and optimization to improve the mechanical properties may be required for load-bearing applications.

4.3. Introduction

Large bone defects caused by injury or disease often require biomaterial grafts to completely regenerate[126]. Current techniques designed to enhance bone tissue regeneration commonly employ autologous, allogeneic, xenogeneic, or synthetic grafts[36]. Autologous bone grafting, for which the material is derived from the patient, is considered the “gold standard” grafting practice in large bone defect repairs, but there are several drawbacks including size and shape limitations, tissue availability, and sampling site morbidity[38]. In addition, autologous grafting procedures are prone to infections, subsequent fractures, hematoma formation at the sampling or repaired site, and post-operative pain[40]. Bone tissue engineering (BTE) provides a potential alternative to traditional bone grafting methods[127]. It combines the use of structural biomaterials and cells to create new functional bone tissue. The biomaterials used for BTE should be designed with a macroporous architecture, surface chemistry for cell attachment, and mechanical properties similar to those of the native bone[128]. Previous studies have shown that the optimal pore size for biomaterials used for BTE is approximately 100-200 µm[129], and the optimal elastic modulus is 0.1 to 20 GPa depending on the grafting site[130]. Moreover, the porosity and pore interconnectivity are two important factors that affect cell migration, nutrient diffusion, and angiogenesis[130].

BTE has shown promising results with a diverse set of biomaterials developed as alternatives to bone grafts. These biomaterials include osteoinductive materials, hybrid materials, and advanced hydrogels[130]. Osteoinductive materials induce the formation of *de novo* bone structure.

Hybrid materials are made of synthetic and/or natural polymers[130]. Advanced hydrogels mimic the extracellular matrix (ECM) and deliver the required bioactive agents to promote bone tissue integration[130]. Hydroxyapatite is a traditional material choice for BTE due to its biocompatibility and composition[43]. Another type of biomaterial for BTE is bioactive glass, which stimulates specific cell responses to activate genes necessary for osteogenesis[131,132]. Biodegradable polymers such as poly(glycolic acid) and poly(lactic acid) are also widely used for BTE[133]. Finally, natural (or naturally-derived) polymers such as chitosan, chitin, and bacterial cellulose have also shown promising results for BTE[54]. Although these polymers, either natural or synthetic, show some potential for BTE, extensive protocols are usually required to obtain a functional biomaterial with a desired macrostructure. Conversely, native macroscopic cellulose structures can be derived from various plants. In a previous study, our group demonstrated that following a simple surfactant treatment, cellulose-based scaffolds derived from plants can be used as a material for various tissue reconstruction, taking advantage of the native structure of the plant[16]. Furthermore, these biomaterials can be used for *in vitro* mammalian cell culture[16], are biocompatible, and can become spontaneously vascularized subcutaneously[15–17]. Our group and others have shown that these biomaterials can be sourced from specific plants according to the intended application[15–17,19,20]. For instance, the vascular structure from plant stems and leaves displays a similar structure to the one found in animal tissues[20]. Plant-derived cellulose scaffolds can also easily be carved into specific shapes and treated to alter their surface biochemistry[17]. In a recent study, we included a salt buffer in the decellularization process, which resulted in an increase in cell attachment, both *in vitro* and *in vivo*[17]. In the same study, we showed that plant-derived cellulose can be used in composite biomaterials by casting hydrogels onto the scaffold surface. In recent studies, functionalization of plant-derived scaffolds has proven to improve their efficiency[19]. For example, Fontana et al., 2017 showed that RGD-coated decellularized stems support the adhesion of human dermal fibroblasts as opposed to non-coated stems. Furthermore, the authors also showed that decellularized plant stems can be artificially mineralized in modified simulated body

fluid. More recently, Lee et al. (2019) employed plant scaffolds to generate bone-like tissues *in vitro*. After assessing a variety of plants, the authors found that apple-derived scaffolds were the most suitable for the culture and differentiation of human induced pluripotent stem cells (hIPSCs). They also suggested that structural and mechanical properties of the apple-derived scaffolds play a key role. Apple-derived scaffolds were the first plant-derived scaffold employed in tissue engineering applications and have been demonstrated to have a very similar architecture to bone, especially with regards to their interconnected pores ranging from 100 to 200 µm in diameter[4,16].

In the present study, we further examined the potential of apple-derived cellulose scaffolds for BTE and analyzed their mechanical properties *in vitro* and *in vivo*. While the potential use of apple-derived scaffolds for BTE applications has been studied[4], the mechanical properties of the scaffolds have not been investigated systematically. Results of the present study show that scaffolds seeded with MC3T3-E1 and cultured in differentiation medium have a Young's modulus of 192 ± 17 kPa, which is significantly higher than those of cell-seeded scaffolds cultured in non-differentiation medium (24 ± 9 kPa) and acellular scaffolds (32 ± 5 kPa). Nevertheless, the Young's modulus of healthy bone tissue is typically in the range of 0.1 to 2 GPa for trabecular bone and between 15 and 20 GPa for cortical bone[130]. Moreover, after implantation for 8 weeks in a rodent calvarial defect model, the cell-seeded scaffolds were integrated into the surrounding bone, requiring a force of 114±18 N to push out the scaffolds from the surrounding bone, similar to values reported in previous studies of cortical bone displacement[134]. While these results are very promising, especially for non load-bearing applications, apple-derived cellulose scaffolds still lack the appropriate mechanical properties to match the surrounding bone tissue at an implant site. Further development is therefore required for these scaffolds to reach their full potential.

4.4. Materials and Methods

4.4.1. Scaffold preparation

Samples were prepared following established methods[17]. Briefly, McIntosh apples (Canada Fancy) were cut in 8 mm-thick slices with a mandolin slicer. The hypanthium tissue of the apple slices was cut into squares of 5 mm by 5 mm. The square tissues were decellularized in 0.1% sodium dodecyl sulfate (SDS, Fisher Scientific, Fair Lawn, NJ) for two days. Decellularized samples were then washed in deionized water, followed by an overnight incubation at room temperature in 100 mM $CaCl_2$ to remove the remaining surfactant. The samples were subsequently sterilized with 70% ethanol for 30 min, washed with deionized water, and placed in a 24-well culture plate prior to cell seeding.

4.4.2. Cell culture and scaffold seeding

MC3T3-E1 Subclone 4 cells (ATCC® CRL-2593™, Manassas, VA) were maintained at 37°C in a humidified atmosphere of 95% air and 5% CO_2. The cells were cultured in culture medium made of Minimum Essential Medium (α-MEM; ThermoFisher, Waltham, MA) supplemented with 10% fetal bovine serum (FBS; Hyclone Laboratories Inc., Logan, UT) and 1% penicillin/streptomycin (Hyclone Laboratories Inc.), before being trypsinized once they reached 80% confluency. They were then resuspended in culture medium.

A 40 μL aliquot of cell suspension containing 10^6 cells was pipetted on the scaffolds. The cells were left to adhere for 1h in cell culture conditions (i.e., at 37°C in a humidified atmosphere of 95% air and 5% CO_2). Subsequently, 2 mL of culture medium were added to each culture well. Culture medium was changed every 2-3 days, for 14 days. After this incubation, differentiation of MC3T3-E1 cells was induced by adding 50 μg/mL ascorbic acid and 4 mM sodium phosphate to the culture medium (differentiation medium). Differentiation medium was changed every 3-4 days, for 4 weeks. Scaffolds in non-differentiation culture medium (without the supplements to induce

differentiation) were incubated for the same duration, with the same medium change schedule, and served as a negative control. All subsequent analyses were conducted at the end of the 4-week incubation. Finally, the cell-seeded scaffolds were imaged after the 4-week incubation using a 12-megapixel digital camera and compared to scaffolds with no seeded cells.

4.4.3. Pore size measurements and cell distribution analysis using confocal laser scanning microscopy

To measure the scaffold pore size, decellularized apple scaffolds (prior to MC3T3-E1 cell seeding) (n=3) were thoroughly washed with phosphate buffered saline (PBS; ThermoFisher) and incubated in 1 mL of 10% (v/v) Calcofluor White solution (Sigma-Aldrich, St. Louis, MO) for 25 min in the dark and at room temperature for staining. Subsequently, the scaffolds were washed with PBS and imaged with a high-speed resonant confocal laser scanning microscope (Nikon Ti-E A1-R; Nikon, Mississauga, ON). ImageJ software was used to process and analyze the confocal images. Briefly, maximum projections in the Z axis were created and the Find Edges function was used to highlight the edge of the pores. A total of 54 pores were analyzed (6 pores in 3 randomly selected areas per scaffold, with 3 scaffolds). Pores were manually traced using the freehand selection tool in ImageJ. The selections were fit as an ellipse to output the major axis length.

To analyze MC3T3-E1 cell distribution, cell-seeded scaffolds cultured in non-differentiation or differentiation medium (n=3 for each condition) were washed with PBS (without Ca^{2+} and Mg^{2+}) and fixed with 4% paraformaldehyde for 10 min. They were then washed with deionized water prior to permeabilizing the cells with a Triton-X 100 solution (ThermoFisher) for 5 min, and washed again with PBS. Staining of the scaffolds was performed as previously described[15–17]. Briefly, the scaffolds were incubated in 1% periodic acid (Sigma-Aldrich) for 40 min. After rinsing with deionized water, they were incubated for 2h in the dark and at room temperature in 100 mM sodium metabisulphite (Sigma-Aldrich) and 0.15 M hydrochloric acid (ThermoFisher) supplemented with 100 µg/mL propidium iodide (Invitrogen, Carlsbad, CA).

Finally, they were washed with PBS, stained with 5 mg/mL DAPI (ThermoFisher) for 10 min in the dark, washed again, and stored in PBS prior to imaging. The surfaces of the cell-seeded scaffolds were imaged with the high-speed resonant confocal laser scanning microscope (Nikon Ti-E A1-R). ImageJ software was used to process the confocal images and create a maximum projection in the Z axis for image analysis.

4.4.4. Alkaline phosphatase and calcium deposition

Before staining with either 5-bromo-4-chloro-3'-indolyphosphate and nitro-blue tetrazolium (BCIP/NBT, Sigma-Aldrich) for alkaline phosphatase (ALP) activity or Alizarin Red S (ARS, Sigma-Aldrich) for calcium deposition, scaffolds were washed three times with PBS (without Ca^{2+} and Mg^{2+}) (Hyclone Laboratories Inc.) and fixed with 10% neutral buffered formalin for 30 min.

BCIP/NBT staining solution was prepared by dissolving one BCIP/NBT tablet (Sigma-Aldrich, Cat. No. B5655) in 10 mL of deionized water. After fixation, the scaffolds (n=3 for each experimental condition) were washed with a 0.05% Tween solution and stained with BCIP/NBT for 20 min at room temperature. Finally, they were washed with 0.05% Tween and stored in PBS (without Ca^{2+} and Mg^{2+}) prior to imaging. Alizarin Red S (ARS) staining was used to assess calcium deposition and therefore mineralization of the scaffolds. After fixation, the scaffolds were washed with deionized water and exposed to 2% (w/v) ARS for 1h at room temperature. They were then washed with deionized water to remove the excess ARS staining solution and stored in PBS (without Ca^{2+} and Mg^{2+}) prior to imaging. Finally, all scaffolds were imaged using a 12-megapixel digital camera.

4.4.5. Mineralization analysis using scanning electron microscopy and energy-dispersive spectroscopy

Scaffolds (n=3 for each experimental condition) were fixed in 4% paraformaldehyde for 48h and dehydrated in increasing concentrations of ethanol (from 50% to 100%), as previously

described[135]. They were then dried using a critical point dryer and gold-coated to a final coating thickness of 5 nm. Scanning electron microscopy (SEM) images were acquired with a JEOL JSM-7500F FESEM scanning electron microscope (JEOL, Peabody, MA) at 2 kV. Energy-dispersive spectroscopy (EDS) was performed on three different areas of each scaffold surface for mineral aggregate composition analysis.

4.4.6. Young's modulus measurements

The Young's modulus of the scaffolds after culture in non-differentiation or differentiation medium (n=3 for each experimental condition) was calculated following a compression test using a custom-built uniaxial compression apparatus and compared to that of decellularized apple-derived cellulose scaffolds without MC3T3-E1 seeded cells. The force and position were recorded with a 1.5 N load cell (Honeywell, Charlotte, NC) and an optical ruler, respectively. The force-displacement curves were obtained by compressing the samples (after removing them from the culture medium) at a constant rate of 3 mm min^{-1} and a maximum compressive strain of 10% of the construct height. The Young's modulus was obtained by fitting the linear portion of the stress-strain curve between 9% and 10% strain.

4.4.7. Rat calvarial defect model

Experimental protocols were reviewed and approved by the Animal Care and Use Committee of the University of Ottawa. Bilateral craniotomy was performed following an established protocol[124]. Male Sprague-Dawley rats (n=6) were anaesthetized with isoflurane, first at 3% until they were unconscious, and then at 2-3% throughout the procedure. After removing the periosteum, defects (5-mm diameter) were created in both parietal bones on each side of the sagittal suture using a dental drill equipped with a 5-mm diameter trephine, under constant irrigation of 0.9% NaCl. The surrounding bone was gently cleaned with 0.9% NaCl to remove any bone fragments. Decellularized scaffolds were prepared as described above, were cut into

circular disks (5-mm diameter) with a biopsy punch and were placed in the 5-mm defects. The overlying skin was closed with sutures. Rats were given unlimited access to food and water and were monitored daily by certified animal technicians at the Animal Care & Veterinary Service of the University of Ottawa. Rats were euthanized by CO_2 inhalation and thoracic perforation as secondary euthanasia measure, after 8 weeks post-implantation. The skin covering the skull was removed using a scalpel blade, exposing the cranium. The skull was cut at the frontal and occipital bones and on the side of both parietal bones using a dental drill, thereby completely removing the top section of the skull that was then processed for either mechanical assessment or histological analysis.

4.4.8. Push-out test

To assess the force required to push out the scaffolds from the surrounding bone, push-out tests were carried out after the 8 weeks of implantation using a uniaxial compression device (MTI Instruments, Albany, NY) and a 445N load cell (Omega Engineering, Norwalk, CT). The samples (n=7 from 4 animals) were placed on the sample holder of the instrument so that the dorsal side of the bone was facing up (Figure 4.4 C). A plunger was slowly lowered at 0.5 mm/min until slightly touching the sample. The force vs. distance were recorded until complete push-out of the scaffolds, and the maximum force was recorded at the break point on the force vs. distance curve (Figure 4.4 D).

4.4.9. Cell infiltration and mineralization analysis by histology

In vitro scaffolds (n=1 in non-differentiation medium and n=2 in differentiation medium) were fixed in 4% paraformaldehyde for 48h and stored in 70% ethanol before paraffin embedding, sectioning, and staining by the PALM Histology Core Facility of the University of Ottawa. Briefly, 5 µm-thick serial sections were stained with hematoxylin and eosin (H&E; ThermoFisher) or Von Kossa (VK; ThermoFisher), starting 1 mm inside the scaffolds. Slides were imaged using a Zeiss

AXIOVERT 40 CFL microscope (Zeiss, Toronto, ON) to evaluate cell infiltration (H&E) and mineralization (VK). Image analysis was performed using ImageJ software.

In vivo scaffolds (n=4 from 2 animals) were fixed in 10% formalin (Sigma-Aldrich) for 72h and stored in 70% ethanol (Sigma-Aldrich), and all subsequent embedding, sectioning and staining was performed by AccelLAB Inc. (Boisbriand, QC). The scaffolds were embedded in methyl methacrylate and serially cut in 6-µm thick sections, at three different levels (top, bottom, and towards the center). Sections were stained with either H&E or Goldner's Trichrome (GTC). Histological slides were imaged using a Zeiss AXIOVERT 40 CFL microscope to evaluate cell infiltration (H&E) and collagen deposition (GTC). Images were analyzed using ImageJ software.

4.4.10. Statistical analysis

All data are reported as mean ± standard error of the mean. The data were assumed to be normally distributed. The Levene's test was used to confirm that the data conformed to the assumption of homogeneity of variance. Statistical analysis was then performed using a one-way ANOVA followed by Tukey post-hoc tests for Young's moduli mean comparison. A value of $p < 0.05$ was considered to be statistically significant.

4.5. Results

4.5.1. Pore size measurement, cell distribution, and in vitro mineralization

Complete removal of native cellular components of the apple tissue was achieved after SDS and $CaCl_2$ treatments (Figure 4.1 A). The highly porous nature of the scaffolds was observed using confocal microscopy. Image quantification revealed an average pore size of 154 ± 40 µm. The pore size distribution ranged from 73 µm to 288 µm, with the majority of the pores ranging between 100 and 200 µm (Figure 4.1 C).

After 4 weeks of culture in differentiation medium, white mineral deposits were observed throughout the cell-seeded scaffolds (Figure 4.1 A). Scaffolds with cells had a distinct opaque white colour, suggesting mineralization, that was not observed in the blank scaffolds (scaffolds without cells). Finally, confocal laser scanning microscopy analysis also showed that cells were homogenously distributed in the scaffolds (Figure 4.1 B).

To analyze ALP activity and mineralization, the scaffolds were stained with BCIP/NBT and ARS, respectively (Figure 4.1 D). The BCIP/NBT staining revealed that ALP activity increased significantly (as indicated by the strong purple colour) in cell-seeded scaffolds cultured in differentiation medium compared to blank scaffolds or cell-seeded scaffolds cultured in non-differentiation medium. Similarly, cell-seeded scaffolds cultured in differentiation medium displayed a stronger red color after ARS staining, indicating a higher degree of calcium mineralization, than the blank scaffolds or the cell-seeded scaffolds cultured in non-differentiation medium. Some background staining was clearly visible in the blank scaffolds, possibly due to the use of $CaCl_2$ in the decellularization protocol.

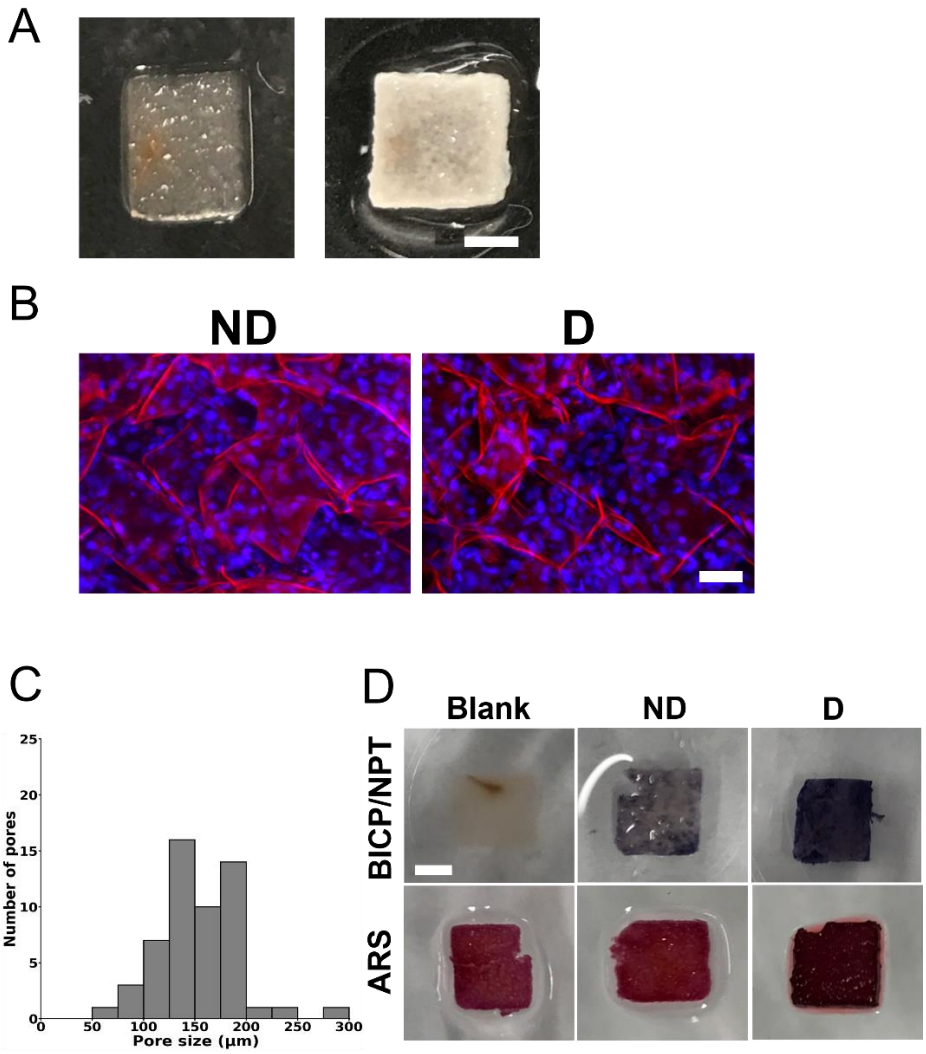

Figure 4.1: (A) Representative photographs of an apple-derived cellulose scaffold after removal of the plant cells and surfactant (left) and a MC3T3-E1-seeded scaffold after 4 weeks in osteogenic differentiation medium (right) (scale bar = 2 mm); (B) Representative confocal laser scanning microscope images showing seeded cells in a scaffold after 4 weeks of culture in non-differentiation medium ("ND") or osteogenic differentiation medium ("D") (scale bar = 50 µm). The scaffolds were stained for cellulose (red) and for cell nuclei (blue) using propidium iodide and DAPI staining, respectively; (C) Pore size distribution of decellularized apple-derived cellulose scaffolds before MC3T3-E1 cell seeding, from maximum projections in the Z axis of confocal images. A total of 54 pores were analyzed in 3 different scaffolds (6 pores in 3 randomly selected areas per scaffold); (D) Representative photographs of scaffolds stained with 5-bromo-4-chloro-3'-indolyphosphate and nitro-blue tetrazolium (BCIP/NBT) for alkaline phosphatase (ALP) activity or Alizarin Red S (ARS) for calcium deposition, to visualize mineralization (scale bar = 2 mm - applies to all). The scaffolds without cells ("Blank") did not stain with BCIP/NBT. Stronger ALP activity was visualized by stronger blue contrast in the scaffolds cultured in differentiation medium ("D"), compared to their counterparts cultured in non-differentiation medium ("ND"). For the ARS staining, the blank scaffolds and the scaffolds cultured in non-differentiation medium ("ND") displayed a lighter red color than the scaffolds cultured in differentiation medium ("D"). The calcium deposition was highlighted by a strong, dark red color in the scaffolds cultured in differentiation medium ("D"). Three different scaffolds (n=3) were analyzed for each experimental condition.

Staining (H&E and VK) as well as SEM and EDS were used to analyze cell infiltration and further evaluate mineralization. H&E staining (Figure 4.2 A) showed that the cell-seeded scaffolds cultured in either non-differentiation or differentiation medium displayed good cell infiltration, with multiple nuclei visible in the periphery and through the scaffolds. Collagen was also visible in pale pink. In addition, VK staining revealed that the pore walls of the scaffolds were stained after 4-weeks of culture in differentiation medium. The pore walls of the scaffolds cultured in non-differentiation medium only showed the presence of calcium deposition on the outside periphery of the constructs, likely because of the absorption of calcium from the decellularization treatment. SEM analysis of the cell-seeded scaffolds (Figure 4.2 B) revealed localized mineralization on the cell-seeded scaffolds cultured for 4 weeks in differentiation medium. Mineral deposits appeared as globular aggregates on the edge of the pores. No mineral aggregates were visible on the cell-seeded scaffolds cultured for 4 weeks in non-differentiation medium and on blank scaffolds. EDS spectra acquired on selected regions of interest, namely on the mineral aggregates on the cell-seeded scaffolds and on pore walls of the blank scaffolds, clearly displayed distinct characteristic signals corresponding to the deposition of phosphorous (P) and calcium (Ca) on the cell-seeded scaffolds cultured for 4 weeks in differentiation medium (Figure 4.2 B).

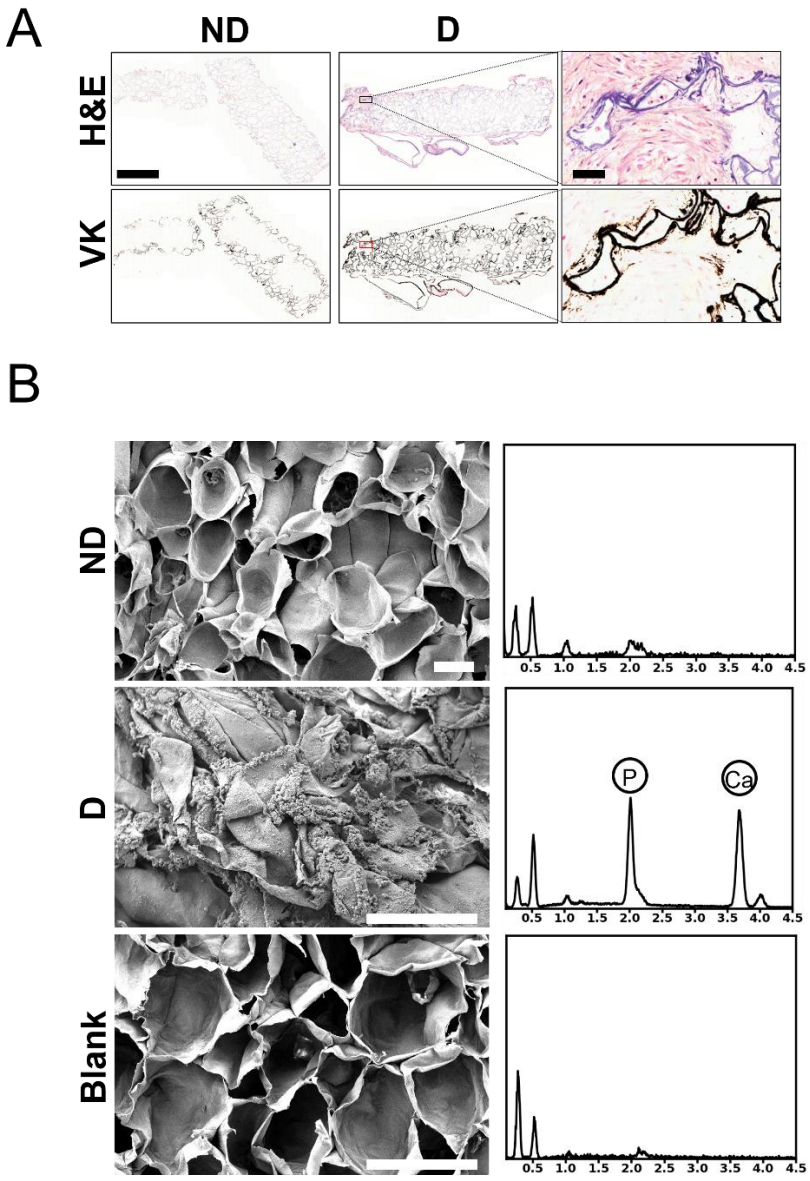

Figure 4.2: (A) Representative images of scaffold histological cross-sections. Paraffin-embedded scaffolds were cut into 5 µm-thick sections and stained with Hematoxylin and Eosin (H&E) to visualize cell infiltration or Von Kossa (VK) to visualize mineralization. Scaffolds were infiltrated with MC3T3-E1 cells with multiple nuclei and cytoplasm visible at the periphery and throughout the scaffolds (blue and pink, respectively). Collagen was also visible in pale pink. The pore walls in the scaffolds cultured in non-differentiation medium ("ND") only showed the presence of mineralization at their periphery. The pore walls in the scaffolds cultured in differentiation medium ("D") were entirely stained in black. The analysis was performed on one scaffold cultured in non-differentiation medium ("ND") and on 2 scaffolds cultured in differentiation medium ("D") (Scale bar = 1 mm for the lower magnification pictures and 50 µm for the higher magnification pictures); (B) Representative scanning electron microscopy micrographs and energy-dispersive spectra: Scaffolds were gold-coated and imaged using a JEOL JSM-7500F FESEM scanning electron microscope at 3.0 kV (scale bar= 100 µm - applies to all). Energy-dispersive spectroscopy spectra were acquired on each scaffold. Phosphorus (2.013 keV) and calcium (3.69 keV) peaks are indicated on each spectrum. Three different scaffolds were analyzed for each condition. Blank: scaffolds without seeded cells.

4.5.2. In vitro biomechanical analysis

The Young's modulus of cell-seeded scaffolds was measured after 4 weeks of incubation in either non-differentiation or differentiation medium and compared to that of the blank scaffolds without cells) (Figure 4.3). Results showed no significant difference in the Young's modulus between the blank scaffolds (32 ± 5 kPa) and the scaffolds cultured in non-differentiation medium (24 ± 9 kPa; p=0.88). On the other hand, a significant difference was observed between the blank scaffolds (31.6 ± 4.8 kPa) and the scaffolds cultured in differentiation medium (192 ± 17; p<0.001). Furthermore, the Young's moduli of the cell-seeded scaffolds cultured in non-differentiation and differentiation medium were also significantly different (p<0.001).

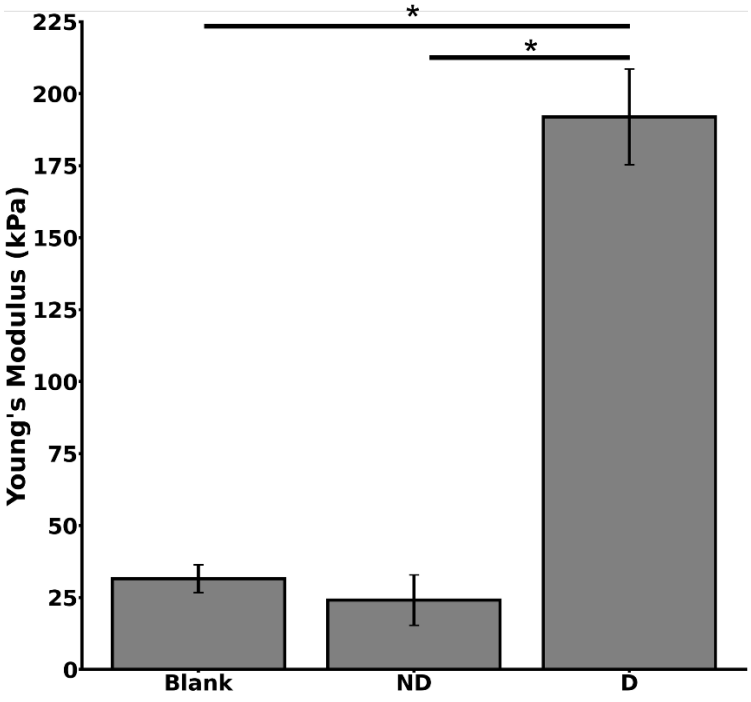

Figure 4.3: Young's modulus of scaffolds without seeded cells ("Blank") and of cell-seeded scaffolds after 4 weeks of culture in either non-differentiation ("ND") or differentiation ("D") medium. Statistical significance (* indicates p<0.05) was determined using a one-way ANOVA and Tukey post-hoc tests. Data are presented as mean ± S.E.M. of three replicate samples for each condition.

4.5.3. In vivo bone regeneration and biomechanical performance

Craniotomies were performed on Sprague-Dawley rats. Bilateral 5-mm diameter defects were created in both parietal bones, and apple-derived cellulose scaffolds (without seeded cells) were implanted in the defects (Figure 4.4 A, B). The top section of the skull was retrieved and processed for either mechanical assessment or histology after 8 weeks.

Upon visual inspection, the scaffolds appeared to have been well integrated with the surrounding tissues of the skull. Mechanical push-out tests were performed to quantitatively assess the integration. Measurements were performed using a uniaxial compression device (Figure 4.4 C) immediately after euthanasia of the animals. Results revealed that the average force required to dislodge the scaffolds from the surrounding bone was 114 ± 18 N.

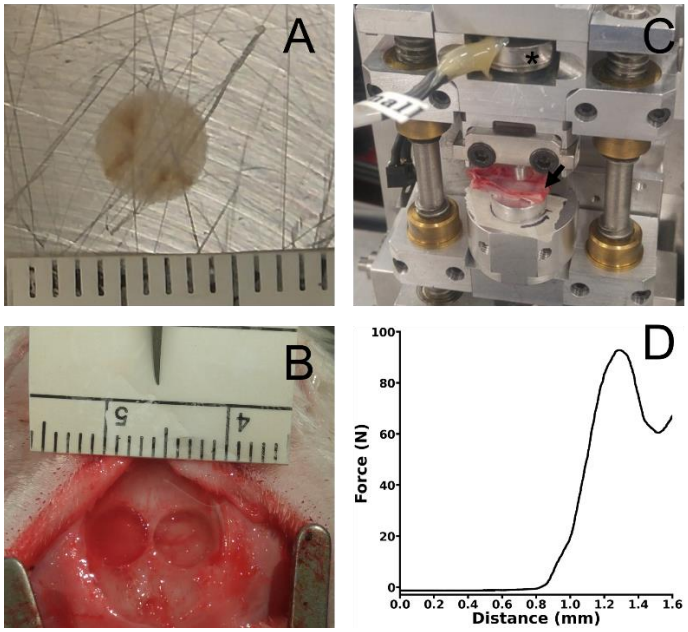

Figure 4.4: (A) Scaffolds; (B) Exposed skull with bilateral defects; (C) Photograph of uniaxial compression device for the push-out tests (the asterix (*) indicates the load cell; the arrow indicates the sample); (D) Typical force-displacement curve obtained during a push-out test.

Finally, histological analysis was performed to evaluate cell infiltration and extracellular matrix deposition within the grafted scaffolds after 8 weeks of implantation (Figure 4.5). H&E staining showed infiltration of cells within the pores of the scaffolds. Evidence of vascularization

(as depicted by blood vessels) was also observed within the scaffolds and GTC staining showed the presence of type 1 collagen within the scaffolds.

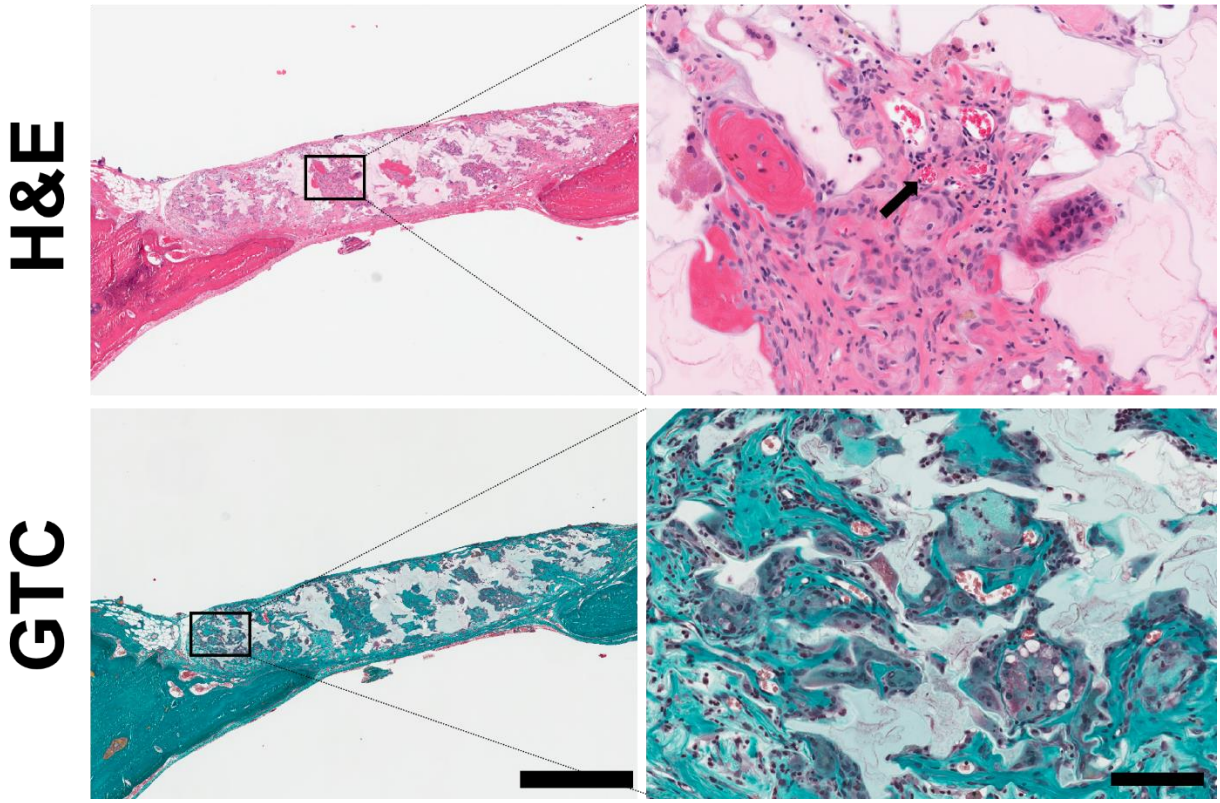

Figure 4.5: Representative images of implanted non-seeded scaffolds histological cross-sections after 8 weeks. Sections were stained with either hematoxylin and eosin (H&E) to visualize cells or Goldner's Trichrome (GTC) to visualize type-1 collagen. The arrow indicates red blood cells. Presence of collagen is visible (scale bar = 1 mm and 200 μm for the left and right insets, respectively).

4.6. Discussion and Conclusion

In vitro and *in vivo* studies have shown the biocompatibility of plant-derived cellulose and their potential use for tissue engineering[15–17,19,20]. Moreover, their uses for hosting osteogenic differentiation have been demonstrated[4]. The aim of the present study was to further examine the potential of apple-derived cellulose scaffolds for BTE applications and analyze their mechanical properties *in vitro* and *in vivo*.

For *in vitro* studies, pre-osteoblast cells (MC3T3-E1) were seeded in the scaffolds after removing the native cells from the apple tissue and were induced to undergo osteogenic

differentiation. Results showed that the cells were able to proliferate and differentiate within the scaffolds, thereby demonstrating the potential for plant-derived cellulose scaffolds to support bone formation. A large number of cell nuclei were observed throughout the scaffold pores, similarly to the observations reported in previous studies[4,15–17]. Moreover, similarly to our previous findings[16] and those of another group[4], we observed that the average diameter of the scaffold pores was ~154 µm, with the majority of the pores between 100 and 200 µm (Figure 4.1 B). These sizes are consistent with the optimum pore size for bone growth, which has been shown to be in the range of 100–200 µm[129].

Staining analysis revealed a higher expression of ALP and the presence of more calcium deposits on the surface of the cell-seeded scaffolds after 4 weeks of culture in differentiation medium than in the blank scaffolds (without seeded cells) and in the cell-seeded scaffolds cultured in non-differentiation medium. Importantly, similar results with differentiated hiPSCs in apple-derived scaffolds have been observed[4]. Histological analysis further confirmed that the constructs were mineralized by the infiltrated osteoblasts after differentiation. Of note is that the periphery of the constructs cultured in non-differentiation medium was also stained with VK. This non-specific staining may have been due to residual $CaCl_2$ in the scaffolds after the decellularization process. Mineralization was further assessed by qualitative analysis of SEM pictures. After culture in differentiation medium, cell-seeded scaffolds displayed signs of ECM mineralization, with aggregates of minerals visible on the scaffold surface, specifically at the edges of the pores, which is consistent with previous studies using ECM scaffolds[123] and plant scaffolds[4]. These aggregates were not visible on the surface of the scaffolds without cells. EDS analysis of the aggregates revealed high level of P and Ca, thereby suggesting the presence of apatite.

A significant change (approximately 8-fold increase) in the Young's modulus of the scaffolds was demonstrated after culture in differentiation medium. On the other hand, the modulus of the scaffolds cultured in non-differentiation medium was similar to that of the blank scaffolds (without

seeded cells). However, It should be noted that despite the increase in the Young's modulus of the scaffolds cultured in differentiation medium, the moduli remained much lower than that of bone (0.1 to 2 GPa for trabecular bone and 15 to 20 GPa for cortical bone)[130], cancellous allograft (3.78 GPa)[136] alloplastic grafts made of poly-ether-ether-ketone (3.84 GPa) [136], titanium (50.20 GPa)[136], and cobalt-chromium alloy (53.15 GPa)[136] implants. Disparity between the Young's modulus of the scaffolds and the surrounding bone can cause stress shielding[32]. The imbalance of stress distribution at the bone-implant interface can thus lead to bone augmentation or bone resorption around the implant and ultimately implant failure[32]. Therefore, in the current formulation, these scaffolds may not be appropriate for load-bearing applications.

Decellularized apple scaffolds were then implanted in 5 mm critical-sized cranial defects in rats. Mechanical assessment indicated an average force of 113.6 ± 18.2 N to dislodge the scaffolds from the surrounding bone. This force is similar to the force required to displace intact calvarial bone (127.1 ± 9.6 N)[134]. This indicates that the scaffolds integrated well to the surrounding bone and connective tissues. Moreover, the force is similar to the one reported after 8 weeks implantation of calcium-deficient hydroxyapatite scaffolds loaded with bone morphogenic protein-2 (119.1 ± 17.8 N)[134].

In summary, this study confirmed that pre-osteoblasts can adhere and proliferate within apple-derived cellulose scaffold constructs. Mineralization occurred within cell-seeded scaffolds after chemically inducing osteogenic differentiation of pre-seeded pre-osteoblasts, which resulted in a significant increase in the Young's modulus of the constructs, although it remained much lower than that of natural bone. Moreover, the force required to dislodge the implanted plant-derived cellulose scaffolds was similar to the one observed with calvarial bone and other type of scaffolds used for BTE. Similarly, to previous reports, cells infiltrated the scaffolds and deposited type-1 collagen. Overall, these results show that plant-derived cellulose scaffolds have potential for BTE applications, which is consistent with the findings of a previous study from a different group[4].

However, the difference in stiffness compared to trabecular or cortical bone will likely require the development of composite biomaterials to better match the mechanical properties of living bone. While interest in the use of plant-derived scaffolds for BTE has grown in recent years, this biomechanical mismatch limits their applications, especially for load-bearing conditions. Re-engineering plant-derived cellulose scaffolds through chemical modification or creating composites with other biological/synthetic polymers, as we have previously shown[17], may be required for load bearing applications.

4.7. Acknowledgments

This work was supported by a Discovery Grant from the Natural Sciences and Engineering Research Council of Canada (NSERC) and a grant from the Li Ka Shing Foundation. M.L.L. was supported by the Ontario Centers of Excellence TalentEdge program. R.J.H. was supported by an NSERC postgraduate scholarship and an Ontario Graduate Scholarship (OGS).

Chapter 5:

Mechanosensitive Osteogenesis on Native Cellulose Scaffolds for Bone Tissue Engineering.

This chapter is an adaptation of: Leblanc Latour, M. & Pelling, A. E. Mechanosensitive osteogenesis on native cellulose scaffolds for bone tissue engineering. J. Biomech. 135, 111030 (2022).

This manuscript was published in Journal of Biomechanics, in April 2022.

5.1. Motivation and Objective

Bones are constantly subjected to external forces and stresses. Proper understanding of biomaterial behavior in a representative environment is critical to its performance *in vivo*. The aim of this present chapter is to characterize the mechanosensitivity of osteoblastic cells cultured on apple-derived cellulosic scaffold triggered by external forces. As previous studies on such biomaterial were performed in static environment, this chapter aims to answer the unknown behavior of apple-derived biomaterial under cyclic stress.

5.2. Abstract

In recent years, plant-derived cellulosic biomaterials have become a popular way to create scaffolds for a variety of tissue engineering applications. Moreover, such scaffolds possess similar physical properties (porosity, stiffness) that resemble bone tissues and have been explored as potential biomaterials for tissue engineering applications. Here, plant-derived cellulose scaffolds were seeded with MC3T3-E1 pre-osteoblast cells. Moreover, to assess the potential of these biomaterials, we also applied cyclic hydrostatic pressure (HP) to the cells and scaffolds over time to mimic a bone-like environment more closely. After one week of proliferation, cell-seeded scaffolds were exposed to HP up to 270 KPa at a frequency of 1Hz, once per day, for up to two weeks. Scaffolds were incubated in osteogenic inducing media (OM) or regular culture media (CM). The effect of cyclic HP combined with OM on cell-seeded scaffolds resulted in an increase of differentiated cells. This corresponded to an upregulation of alkaline phosphatase activity and scaffold mineralization. Importantly, the results reveal that well known mechanosensitive pathways cells which regulate osteogenesis appear to remain functional even on novel plant-derived cellulosic biomaterials.

5.3. Introduction

Large defects created by either injury or disease may require graft placement to avoid non-union or malunion of the bone tissue[35]. Grafts can be derived directly from the patient (autologous grafts) and are considered the “gold standard” in regenerative orthopedics[37,38,79,137]. However, limited size grafts, donor site morbidity and infections, cost and post-operative pain at both donor and receiver site has led to the development of alternative approaches[38,79]: cadaver donors (allograft), animal sources (xenograft), or artificially derived (alloplastic). Such alternatives all have their own benefits and drawbacks, the latter however provides a potential alternative with lower risk of transmitted diseases and infections, as well as overcoming the size limitation barrier[38,79]. Alloplastic grafts are also considered a more ethical alternative to allografts and xenografts[41]. Physical properties are key parameters for graft development, such as pore size, interconnectivity and elasticity[32,37,138].

A spectrum of forces acts on different areas of the skeletal system. For instance, the pressure found in the femur head in human adults can reach 5 MPa during normal locomotion and can reach up to 18 MPa for other activities[106]. On a microscopic level, these forces are transmitted to the osteocytes through Wnt/β-catenin mechano-sensing pathways in the lacuna-canaliculi network[27]. Force-regulated mechanisms lead to formation and removal of bone tissue through bone remodeling processes[27] and the pressure inside the lacuna-canaliculi network is around 280 kPa[107]. Bioreactors have also been developed to apply stresses to replicate the native bone environment via uniaxial compression, tension, shear-stress, etc.[108,109]. Pressure modulating bioreactors using low-intensity pulsed ultrasound (LIPUS) were also developed to stimulate osteoblastic and chondrogenic differentiation[139–144]. Finally, hydrostatic pressure (HP) stimulation on cultured cells has also been achieved by compressing the gas phase above an incompressible media[110–116]. Three-dimensional (3D) culturing of the cells is also critical for better representing in

vivo conditions. With a specific scaffold structure and appropriate applied mechanical stimuli one can potentially predict the performance of a biomaterial scaffold prior to in vivo animal studies.

A variety of biomaterials have been utilized to mimic bone tissues. These include hydroxyapatite, tricalcium phosphate, bioceramics or bioactive glass[42]. These materials are osteoconductive, can promote osteointegration and provide structural support at the implant site[42]. However, they show little osteogenic response[42]. Polymer biomaterials such as poly(glycolic acid) (PGA), poly(lactic acid) (PLA) and poly(ε-caprolactone) (PCL) are also biocompatible, possess tunable degradation rates and can be chemically modified to change the surface chemistry[71]. However, in vivo degradation creates acidic biproducts which can lead to an inflammatory response and decrease the efficiency bone repair[71]. Finally, naturally occurring polymers such as collagen, chitosan and silk are also common[71]. However, due to their inherent mechanical properties and structural stability, these materials are often utilized as composites with additional polymers and coatings in BTE applications[21,71,78] . More recently, plant-derived decellularized cellulose scaffolds have been shown to be effective in BTE applications[2,4,145].

Previous studies by our group and others have shown that cellulose-based scaffolds derived from plants can be used as tissue engineering scaffolds[4–17,19,20,146]. These biomaterials are often sourced from plants with a microstructure that closely mimics the tissue to be replicated[17]. Successful experiments in vitro and in vivo showed that these biomaterials are biocompatible and support angiogenesis[4,15–17]. Other groups have successfully differentiated human pluripotent stem cells into bone-like tissues within scaffolds derived from either decellularized mushrooms[147], carrot[5], bamboo stem[12] or apple tissues[4]. The in vivo performance of the apple-derived scaffolds were further examined by implanting disk-shaped scaffolds in rat cranial defects[4]. The findings demonstrate partial bone regeneration within the implant, type 1 collagen deposition and blood vessel formation[4]. However, to date, the mechanobiology of cells cultured on plant-derived scaffolds has not been examined. It remains poorly understood how mechanical signal

transduction pathways are, or are not, impacted when cultured on plant-derived cellulosic biomaterials. Here, to further examine the potential role plant-based biomaterials can play in BTE applications, we explore how mechanical stimulation impacts the differentiation of pre-osteoblasts when cultured on plant cellulose scaffolds. In a custom-built bioreactor, we apply cyclic HP stimulation to differentiating osteoblasts and examine the regulation of key markers of osteogenesis and mineralization. The results reveal that application of HP, in combination with osteogenic inducing media, leads to enhanced differentiation for cell-seeded MC3T3-E1 native cellulose scaffolds, and no significant change in the Young's modulus of the scaffolds. This work provides further evidence that plant-derived cellulose scaffolds support osteogenesis and have potential applications in BTE.

5.4. Materials and Methods

5.4.1. Scaffold fabrication

Samples were prepared following established protocols[15–17]. MacIntosh apples were cut with a mandolin slicer to 1 mm-thick slices. A biopsy punch was used to create 5 mm-diameter disks in the hypanthium tissue. The disks were decellularized in a 0.1% sodium dodecyl sulfate solution (SDS, Fisher Scientific, Fair Lawn, NJ) for 48h. Then, the decellularized disks were washed in deionized water before incubation in 100 mM CaCl2 for 48h. The samples were sterilized with 70% ethanol and placed in a 96-well culture plate.

MC3T3-E1 Subclone 4 cells (ATCC® CRL-2593™, Manassas, VA) were cultured in Minimum Essential Medium (ThermoFisher, Waltham, MA), supplemented with 10% Fetal Bovine Serum (Hyclone Laboratories Inc., Logan, UT) and 1% Penicillin/Streptomycin (Hyclone Laboratories Inc). Scaffolds were immersed in culture media and incubated at 37°C, 5% CO_2, for 30 min. Cells were suspended and a 30 µL drop containing 5 x 10^4 cells, was pipetted on each scaffold. The cells were left to adhere for 2 hours before adding 200 µL of culture media. Culture

media was then changed every 3-4 days for 1 week. Cell seeded scaffolds were then either incubated in osteogenic media (OM) by adding 50 μg/mL of ascorbic acid and 10 mM β-glycerophosphate to the culture media or incubated in culture media (CM) for 2 weeks, with or without the application of HP.

5.4.2. Cyclic hydrostatic pressure stimulation

Cyclic HP was applied by modulating the pressure in the gas phase above the culture wells in a custom-built pressure chamber (Figure 5.1 A). The humidified incubator atmosphere was compressed using an air compressor. A Particle Photon microcontroller (Particle Industries, San Francisco, CA) was used to control the frequency of the applied pressure remotely via a custom-made cellphone application through the Blynk IoT platform (Blynk, New York, NY). Cyclic HP was applied 1 hour per day, for up to 2 weeks (Figure 5.1 B) at a frequency 1Hz, oscillating between 0 and 280 kPa with respect to ambient pressure. Pressure was monitored using a pressure transducer. Samples were removed from the pressure chamber after each cycle and kept at ambient pressure between the stimulation phases.

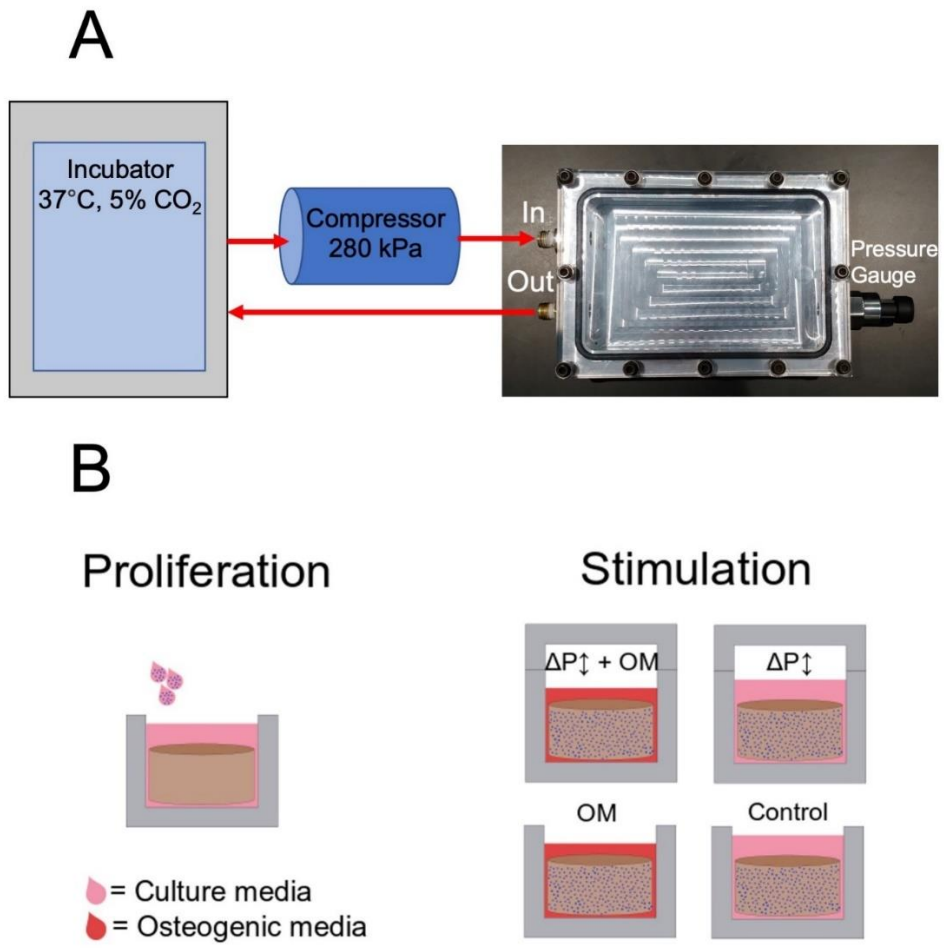

Figure 5.1: (A) Cyclic hydrostatic pressure device schematics. Hydrostatic pressure was applied by modulating the pressure in the gas phase above the culture wells in a custom-build pressure chamber. Air from incubator atmosphere was compressed using a compressor and injected in the pressure chamber using solenoid valves. (B) Experimental conditions. After 1 week of proliferation, cyclic hydrostatic pressure stimulation was applied during 1 hour per day, for up to 2 weeks at a frequency 1Hz, oscillating between 0 and 280 kPa with respect to ambient pressure. The samples were removed from the pressure chamber after each cycle and kept at ambient pressure between the stimulation phases.

Cell-seeded scaffolds were either stimulated with cyclic HP with and without the presence of OM, leading to four experimental conditions (Figure 5.1 B): Cyclic HP in regular culture media (CM-HP), cyclic HP in osteogenic culture media (OM-HP), non-stimulated in osteogenic media (OM-CTRL) and non-stimulated in regular culture media (CM-CTRL).

5.4.3. Scaffold imaging

Scaffolds were washed with PBS and fixed with 10% neutral buffered formalin for 10 min. Scaffolds were washed with PBS and incubated in a 0.01% Congo Red staining solution (Sigma-Aldrich, St. Louis, MO) for 20 min at room temperature. Cell nuclei were stained with 1:1000 Hoechst (ThermoFisher, Waltham, MA) for 30 min. Samples were washed with PBS and stored in wash buffer solution (5% FBS in PBS). The cell-seeded scaffolds were imaged with a laser scanning confocal microscope (Nikon Ti-E A1-R) equipped with a 10X objective. Maximum intensity projections were used for cell counting with ImageJ software[148]. Cells were counted on a 1.3 by 1.3 mm^2 area (N=3 per experimental conditions with 3 randomly selected area per scaffold).

5.4.4. Alkaline phosphatase activity assay

Alkaline phosphatase (ALP) activity in media was measured using an ALP assay kit (BioAssay Systems, Hayward, CA). Working solution was prepared with 5 mM magnesium acetate and 10 mM p-nitrophenyl phosphate (pNPP) in assay buffer, following manufacturer's protocol. 150 μL of working solution was pipetted in 96-well plate. 200 μL of calibrator solution and 200 μL of dH2O were pipetted in separated well, in the same 96-well plate. At 1 week and 2 weeks, 20 μL of incubation media was pipetted into the working solution's well. All wells were read at 405 nm for 10 minutes, every 30 seconds. ALP activity was calculated by taking the slope of the 405 nm readings vs time. Wells were read in triplicates (N=3 per experimental conditions).

5.4.5. Alizarin red S staining and mineral deposit quantification

Samples were fixed with 10% neutral buffered formalin for 10 min, after 1 week or 2 weeks. Calcium quantification was performed using previously published protocol[149]. Samples were transferred to a 24-well plate and carefully washed with deionized water and incubated in 1 mL of 40mM (pH=4.1) alizarin red s (ARS, Sigma-Aldrich) solution for 20 minutes at room temperature,

with light agitation. The samples were washed with deionized water and placed in 15 mL tubes filled with 10 mL dH2O. The tubes were placed on a rotary shaker at 120 rpm for 60 min and dH2O was replaced every 15 min. Thereafter, samples were incubated in 800 µL of 10% acetic acid on an orbital shaker at 60 rpm for 30 min. The eluted ARS/acetic acid solution was transferred to 1.5 mL centrifuge tubes. Tubes were centrifuged at 17 x 104 g for 15 min. 500 µL of supernatants were transferred to new centrifuge tube and 200 µL of 10% ammonium hydroxide was added. Finally, 150 µL of the solution was pipetted into a 96-well plate and the absorption at 405nm was read using a plate reader. Wells were read in triplicates (N=3 per experimental conditions).

5.4.6. Young's modulus measurements

Young's modulus measurements of the scaffolds were performed using a custom-built uniaxial compression apparatus, as previously described[17]. Briefly, scaffolds were mechanically compressed at a rate of 3 mm/min. The Young's modulus of the scaffolds under the different experimental conditions were obtained by fitting the linear region of the stress-strain curve.

5.4.7. Statistical analysis

Reported values are the average value ± standard error of the mean (SEM). Statistical significance was determined using one-way ANOVA and post hoc Tukey test. A value of $p < 0.05$ was considered to be statistically significant.

5.5. Results

5.5.1. Scaffold imaging and cell counting

The application of HP significantly increases the density of cells (Figure 5.2) after 1 week in OM compared to the static condition ($p=10^{-5}$), but the increase was not significant after 2 weeks ($p=0.07$). Conversely, in CM a non-significant increase in the density of cells was observed with

applied HP after 1 week ($p=0.21$) and 2 weeks ($p=0.92$). Importantly, we also observed a significant increase when incubated in OM compared to CM after 1 week of HP stimulation ($p=0.02$). After 2 weeks of HP stimulation, samples cultured in OM exhibited a similar density to samples cultured in CM ($p=0.23$). The results indicate that cell density increases more rapidly in the first week of stimulation in OM compared to CM media but that by two weeks the cell densities become equal. No significant difference was observed in the static cases after 1 or 2 weeks ($p=0.99$ in both cases).

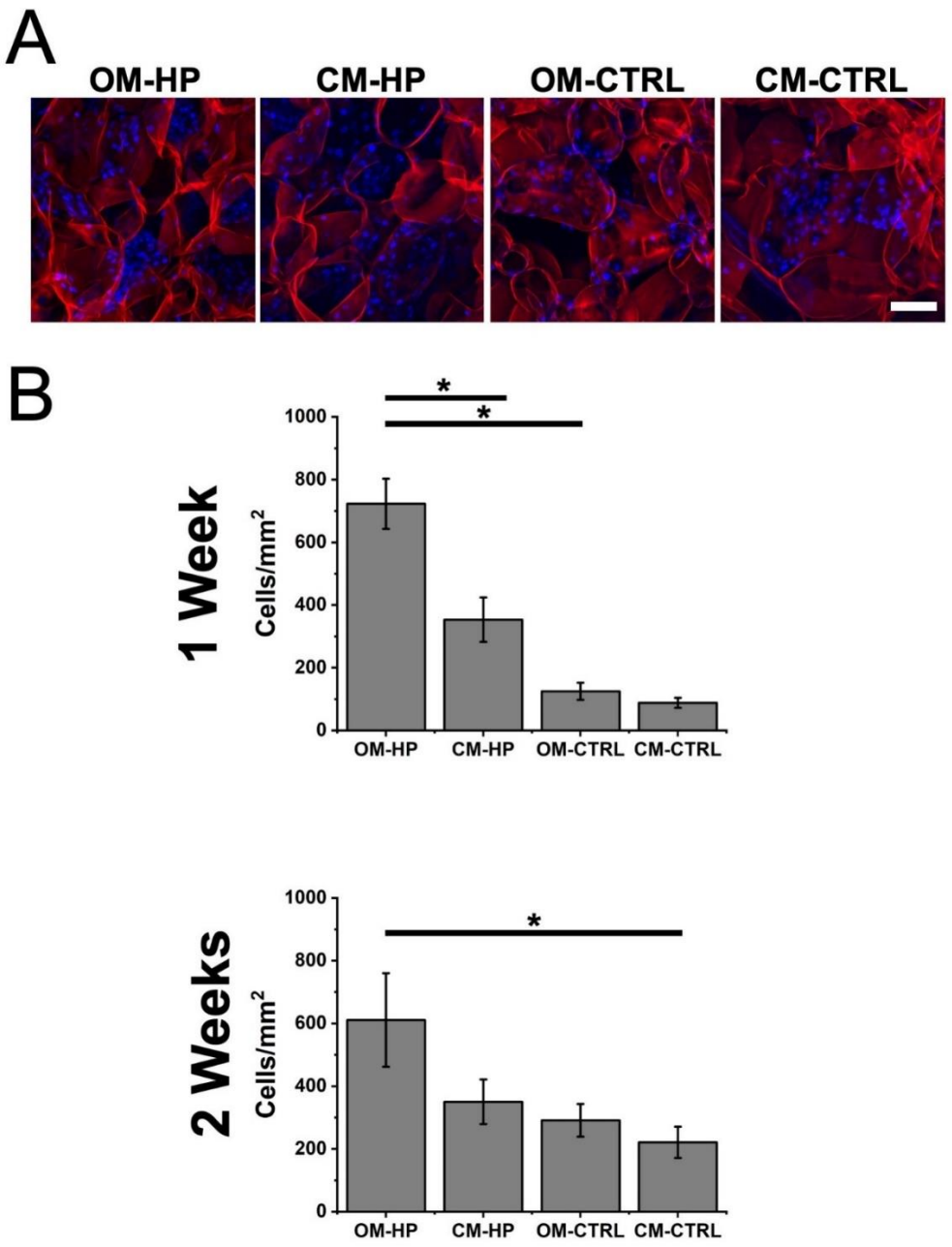

Figure 5.2: (A) Representative confocal laser scanning microscope image showing seeded cells scaffolds (scale bar = 100 µm – applies to all). The scaffolds were stained for cellulose (red) and for cell nuclei (blue). (B) Cellular density after 1 week or 2 weeks of stimulation. Statistical significance (* indicates $p<0.05$) was determined using a one-way ANOVA and Tukey post-hoc tests. Data are presented as means ± S.E.M. of three replicate samples per condition, with three areas per sample. OM-HP: Osteogenic Media – High Pressure; CM-HP: Culture Media – High Pressure; OM-CTRL: Osteogenic Media – Atmospheric Pressure; CM-CTRL: Culture Media – Atmospheric Pressure.

5.5.2. Alkaline phosphatase activity assay

The stimulation with cyclic HP significantly increased the ALP activity (Figure 5.3) in scaffolds incubated in OM after 1 and 2 weeks compared to static condition ($p=4x10^{-8}$ in both cases). A similar effect was observed in CM after 1 and 2 weeks ($p=0.03$ and $p=5x10^{-8}$ respectively). However, the incubation in OM significantly increased ALP activity when HP is applied compared to incubation in CM, after 1 week ($p<10^{-8}$) but was not significantly different after 2 weeks ($p=0.99$). Consistent with the cell density data the HP-driven increases in ALP activity are only observed during the first week and equalize by the second week of culture. In the absence of HP, the choice of incubation media did not significantly change the ALP activity after 1 or 2 weeks ($p=0.25$ and $p=0.08$ respectively).

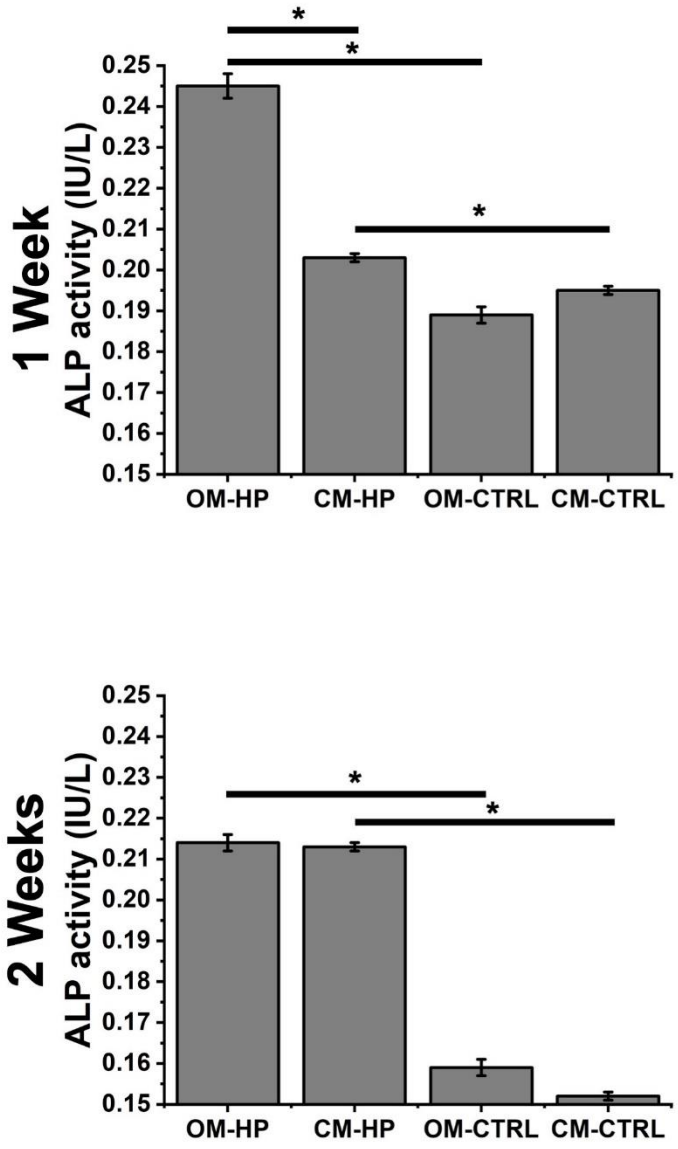

Figure 5.3: Alkaline phosphatase (ALP) activity after 1 week or 2 weeks of stimulation. Statistical significance (* indicates $p<0.05$) was determined using a one-way ANOVA and Tukey post-hoc tests. Data are presented as means ± S.E.M. of three replicate samples per condition. OM-HP: Osteogenic Media – High Pressure; CM-HP: Culture Media – High Pressure; OM-CTRL: Osteogenic Media – Atmospheric Pressure; CM-CTRL: Culture Media – Atmospheric Pressure.

5.5.3. Alizarin red S staining and mineral deposit quantification

The application of cyclic HP significantly increased mineral deposition (Figure 5.4) for samples incubated in OM compared to static condition after 1 week and 2 weeks ($p=2x10^{-7}$ and $p=2x10^{-8}$ respectively). Similarly in samples cultured in CM, cyclic HP significantly increased

mineral deposition after 1 week and 2 weeks ($p=1x10^{-6}$ and $p=2x10^{-8}$ respectively). Moreover, the incubation in OM significantly increased mineral deposition when HP is applied compared to incubation in CM, after 1 week ($p=2x10^{-4}$) but was not significant after 2 weeks (p=0.99). These results are again consistent with the findings from assays of cell density and ALP activity. Under static conditions mineralization still occurred in OM as expected and was significantly increased compared to CM after 1 week ($p=10^{-3}$) but was not significant after 2 weeks (p=0.75).

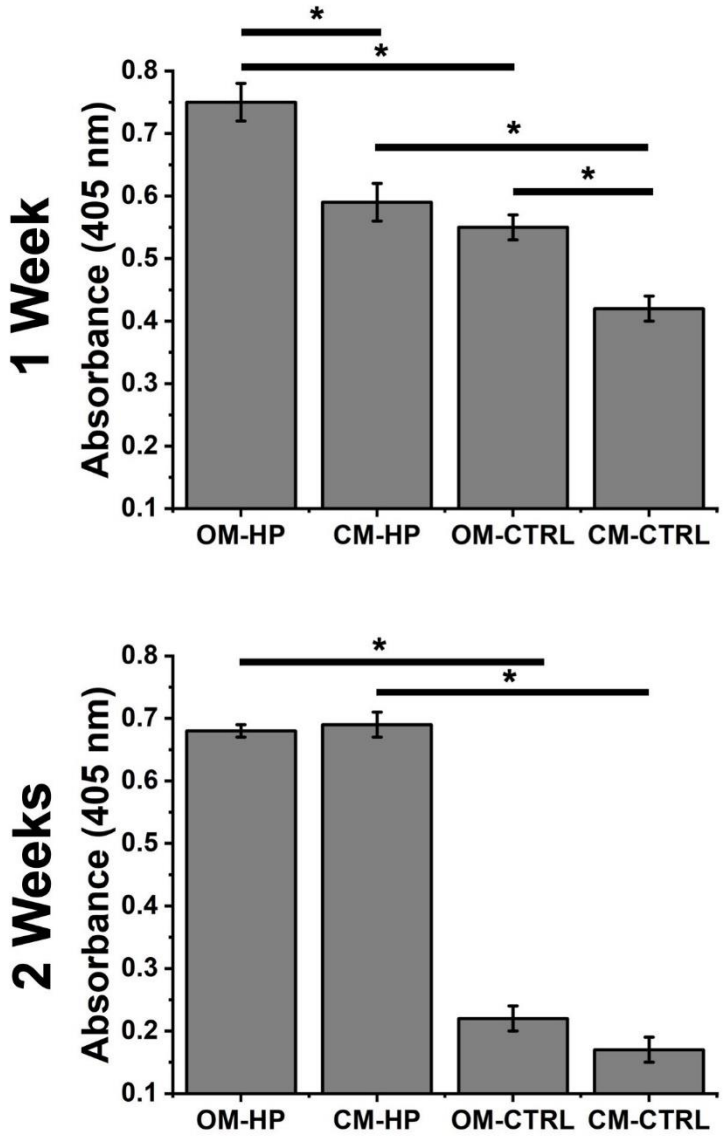

Figure 5.4: Mineral deposit quantification with Alizarin Red S (ARS) staining after 1 week or 2 weeks of stimulation. Statistical significance (* indicates $p<0.05$) was determined using a one-way ANOVA and Tukey

post-hoc tests. Data are presented as means ± S.E.M. of three replicate samples per condition. OM-HP: Osteogenic Media – High Pressure; CM-HP: Culture Media – High Pressure; OM-CTRL: Osteogenic Media – Atmospheric Pressure; CM-CTRL: Culture Media – Atmospheric Pressure.

5.5.4. Young's modulus measurements

Scaffolds were assessed for change in Young's modulus after stimulation (Figure 5.5). Data showed no significant changes between samples incubated in OM with applied HP (16.1 ± 2.1 kPa) and without applied HP (17.2 ± 3.2 kPa) after 1 week and 2 weeks (13.9 ± 0.8 kPa and 18.7 ± 0.7 kPa, respectively). Moreover, no significant change was observed in samples incubated in CM with HP or without HP, both after 1 week (14.2 ± 2.0 kPa and 13.9 ± 0.6 kPa, respectively) or 2 weeks (20.2 ± 2.3 kPa and 14.1 ± 4.7 kPa, respectively). Furthermore, no significant change was observed due to incubation in OM compared to CM, for samples under applied HP after 1 week (16.1 ± 2.1 kPa and 14.2 ± 2.0 kPa, respectively) or 2 weeks (13.9 ± 0.8 kPa and 20.2 ± 2.3 kPa, respectively). Similarly, no significant change was at atmospheric pressure comparing OM and CM at 1 week (17.2 ± 3.2 kPa and 14.2 ± 2.0 kPa, respectively) or after 2 weeks (18.7 ±.7 kPa and 14.1 ± 4.7 kPa, respectively).

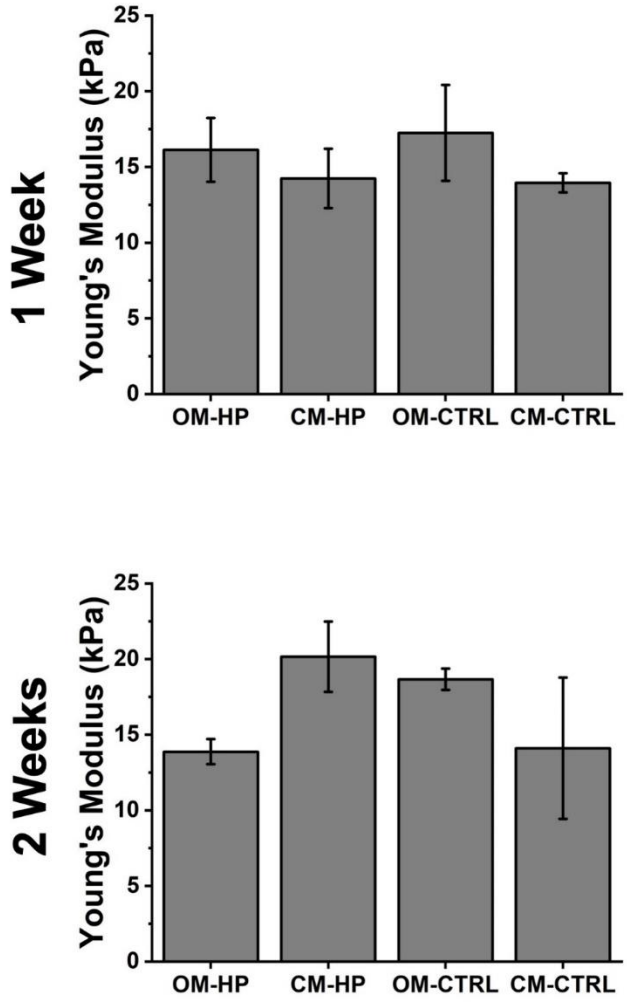

Figure 5.5: Young's modulus of scaffolds after 1 week or 2 weeks of stimulation. No statistical significance was observed between any of the conditions. Data are presented as means ± S.E.M. of three replicate samples per condition. OM-HP: Osteogenic Media – High Pressure; CM-HP: Culture Media – High Pressure; OM-CTRL: Osteogenic Media – Atmospheric Pressure; CM-CTRL: Culture Media – Atmospheric Pressure.

5.6. Discussion

Cells utilize a variety of mechanisms to sense and respond to a variety of mechanical stimuli[150]. Mechanical stimuli are known to affect cell differentiation, tissue regeneration, cytokines and protein expression and proliferation[150,151]. Bones are subjected to constant mechanical

stresses and adapt through remodeling process[27]. In vivo, HP stimulates bone cells and impacts cell differentiation, maker expression and mineralisation[110,112,152]. Plant-derived cellulose scaffolds are an emerging biomaterial in BTE[4], and therefore it is of interest to understand their performance under the mechanical conditions that are found in vivo[32,138]. Cellulose biomaterials derived from plant tissues have shown promising results in vitro and in vivo for targeted tissue engineering[15–17] and have been used to host osteoblastic differentiation[4]. In addition, apple-derived cellulose scaffolds exhibit similar morphological characteristics to trabecular bone and were previously used for BTE applications[4].

In this study, we replicated the mechanical stimuli present during human locomotion and measured the impact of differentiation markers in plant-derived cellulose scaffolds seeded with pre-osteoblast cells. External pressure was applied on the scaffolds in similar magnitude of the lacuna-canaliculi network with a frequency mimicking human locomotion[107,110]. After proliferation, our scaffolds were either cultured in standard culture media, or in osteogenic-inducing differentiation media, with or without high pressure stimulation. Other groups utilizing similar cell lines[115,153], bone marrow skeletal stem cells[112,113,116] or ex-vivo chick femur[110] have also studied the effects if cyclic HP on either 2D surfaces, biomaterial meshes or ex vivo bones. In general, our results show a sensitivity of HP during the early differentiation of the cells during the first week of stimulation. This sensitivity largely subsides during the second week of culture.

Cell counting revealed that the application of HP enhances MC3T3-E1 proliferation when cultured in OM or CM. Consistent with our work, results from previous studies in which metabolic activity has also been shown to be upregulated by mechanical stimulation in comparison to non-stimulated samples[112]. Moreover, it was shown that the application of HP accelerates cell proliferation through upregulated cell cycle initiation[113]. Similarly, reports have shown that physical stimulation of MC3T3-E1 cells induced expression of paracrine factors that leads enhancement of cell proliferation[116]. Additionally, other type of cyclic pressure stimulation, such as ultrasound

stimulation are known to increase the proliferation of MC3T3-E1 cells[139] and human mesenchymal stem cells (hMSC)[140–143]. Importantly, when cultured in OM, cell density increases more rapidly with HP compared to CM during the first week of culture, but the cell densities equalize by the end of the second week. This data is consistent with previous reports of a time-dependent increase in cell number when cultured in OM[154]. Similarly, no significant difference between incubation of MC3T3-E1 cells in similar OM after 2 weeks[155]. Our findings corroborate these studies and further suggest that the application of HP influences the replication rate at early stages of stimulation for samples cultured in OM.

ALP is an important enzyme expressed in the early stages of osteoblastic differentiation[156]. Our results indicate that the application of cyclic HP significantly increases ALP activity, compared to the static case. These findings are consistent with other studies on more conventional scaffolds[112]. For example, a significant increase in ALP activity was also reported after the incubation of scaffolds in osteogenic-inducing differentiation media, similarly to reports on 2D culture systems[154,155]. Other reports showed that ultrasound stimulation increased ALP activity in osteoblast-differentiated hMSC on polyethylene glycol diacrylate (PEGDA)[140] and polylactic acid (PLA)[143] scaffolds, after 3 weeks. The application of HP significantly increased the mineral content in the scaffolds after 1 week and 2 weeks of stimulation, in both types of incubation media. Other groups have shown that a cyclic 300 kPa pressure at 2 Hz frequency on human BMSCs promoted significant mineral deposition[116]. The increase in mineral deposition also noted in ex vivo bone samples, with similar HP force application[110]. Furthermore, the incubation in OM increased the mineral content in the scaffolds, which is consistent with other studies[154,155]. The increased in mineral content was also observed by other groups for osteoblast-differentiated hMSC stimulated with ultrasound, for up to 13% in extracellular calcium deposition[140,143]. Along with ALP expression, mineral content expression further confirms the ongoing differentiation of MC3T3-E1 onto osteoblast, either by applied HP, chemically (induction in OM) or a combination of both.

Although the measured mechanical properties of the scaffolds were consistent with previous studies[5,6,96,140,142,157–160] analysis revealed that the application of cyclic hydrostatic pressure did not impact their elastic properties. Results showed that Young's moduli of the scaffolds (13.9-20.2 kPa, Figure 5.5) are similar to previous reports using apple-derived scaffolds, at 4.17 ± 0.17 kPa[5]. Although our values are slightly higher, the small discrepancy could be due to the type of cultivar used, Golden delicious vs McIntosh. Regardless, our results fall into a broad range of reported values by other groups using other types of decellularized plant cellulose as scaffolds[6]. Similarly, our results are comparable to other cellulose-based biomaterials for BTE: Scaffolds from regenerated cellulose fibers and chitosan, with cultured MC3T3-E1 cells have a reported Young's modulus of up to 0.017 kPa[161]. Cellulose-silk hydrogel was reported to be ranging from 53-72 kPa[160]. Moreover, cellulose-based scaffolds with a higher Young's modulus (in MPa) were also reported[96,158]. Other groups also reported Young's moduli of synthetic scaffolds for BTE, in combination with ultrasound stimulation: PEG-DA, ranging from 0.84 MPa to 2.63 MPa[140,142] or PLA, 2.15 MPa[143]. One should note that the reported Young's moduli are lower than cortical and trabecular bone (15-20 GPa; 0.1-2 GPa, respectively)[130]. Thus, it may be preferrable to limit potential in vivo applications to non-load bearing BTE.

5.7. Conclusion

Plant-derived scaffolds have recently been demonstrated as an interesting alternative to autografts, xenografts and synthetics implants[4–17,19,20,146]. However, it has remained poorly understood how mechanosensitive pathways in bone precursor cells are impacted by being cultured in plant-derived biomaterials. Here, mechanical pressure-driven stimulation has allowed us to characterize the mechanosensitive behaviors of bone precursor cells on these novel scaffolds. The results reveal that application of cyclic HP, in combination with OM, leads to an increase in the number of cells, ALP activity and mineralization over time, as compared to non-stimulated, static experiments. Results showed that the elastic properties of the scaffolds were

not affected by the application of cyclic HP, nor the type of incubation media. Importantly, this work provides evidence that bone-precursor cells possess intact mechanosensing and mechanotransduction pathways when cultured on novel plant-derived scaffolds in a mechanically active environment. These results combined with past in vitro and in vivo studies using apple-derived scaffold biomaterials demonstrate their potential for some BTE applications.

5.8. Acknowledgments

This work was supported by a Discovery Grant from the Natural Sciences and Engineering Research Council of Canada (NSERC) and a grant from the Li Ka Shing Foundation.

Chapter 6:

Nanofibrillar cellulose derivative: UV curable hydrogel and aerogel for bone tissue engineering

This chapter is an adaptation of: Leblanc Latour, M., Tischer, C.A., Harden, J.L. & Pelling, A.E. Nanofibrillar cellulose derivative: UV curable hydrogel and aerogel for bone tissue engineering.

This Manuscript is in preparation for submission.

6.1. Motivation and Objective

The ability for a biomaterial to be correctly placed in a defect is one key to its success for regenerating bone tissues. As demonstrated in the previous chapters, apple-derived scaffolds can be useful for certain BTE applications but cannot be physically scaled beyond the original size of the material's source. The aim of this chapter is to develop a scalable biomaterial with cellulose as its core component, and to study it's performance for BTE applications.

6.2. Abstract

The prevention of bone tissue deformities following a traumatic accident often requires the implantation of a graft. In recent years, researchers have found that cellulose from plants can be used as a matrix for the support, culture and differentiation of bone cells. However, certain constraints, namely scalability and mechanical properties, limit the uses of plant-based biomaterials. To address these constraints, we have created a UV-curable resin that can create hydrogels and aerogels for bone tissue engineering. This resin is derived from nanofibrillar cellulose. The concentration and time of exposure to UV light directly influences the mechanical properties of hydrogels and aerogels. Due to their porosity similar to trabecular bone tissue, and their mechanical properties, aerogels were used for the culture and differentiation of pre-osteoblastic cells. Our results showed that aerogels can support differentiated cells. We also observed calcification of the scaffolds by the differentiated cells. Overall, we have demonstrated a novel way to create hydrogels and aerogels by UV curing of a cellulose fibril-based resin that can be used for bone tissue engineering applications. This cellulose-based resin could eventually be used to create complex shapes, using three-dimensional printing techniques.

6.3. Introduction

Bones are dynamic structures and can remodelled upon stress loading, fracture, or injury. In the event of a major trauma or a large defect in the bone tissue, placement of an external graft is

often required to assist tissue repair. A wide variety of materials have been developed to assist bone regrowth and prevent malunion or non-union or the bone tissue after traumatic injury[35,37]. Such material usually consists of harvested tissue (e.g., from patient's iliac crest), derived from a cadaver or artificially synthesized[35,37,38,79]. Artificially derived materials for bone tissue engineering (BTE) are required to have a porous structure and specific mechanical properties[130,162]. Among the artificially synthetized biomaterials, one can include inorganic materials such as hydroxyapatite and tricalcium phosphate (TCP)[37,38,42]. Hydroxyapatite and TCP are also used as a coating on metal implant, combined with hydrogels, or as a standalone material in forms of granules, porous blocs of injectable formulations[37,38,79]. Organic-derived materials are increasingly being studied for BTE. Protein derived hydrogels, such as collagen and gelatin are usually used as drug delivery vehicles of supplemented with growth factors, bone morphogenic protein or hydroxyapatite[37,38,79,80]. Polysaccharides are also becoming increasingly studied for tissue engineering, including BTE[80,88,89,163]. Among them, cellulose has gained recent interest in biomedical and tissue engineering[4,15–17,19,20,88–90].

Cellulose, along with hemicellulose, lignin, and pectin, forms lignocellulosic materials that constitute plants cell walls[87]. In plants, lignocellulosic material forms a complex architecture which consists of formation of interconnected pores, channels, or alternating layers[87]. Cellulose can be extracted from trees and plant or synthesised by bacteria in pure form. In recent years, several plant-based materials for tissue engineering were developed[15–17,19,20]. More specifically, apple-derived cellulose was used as scaffolds for BTE[4,164] and drew media attention[165]. However, plant derived scaffolds lack the scalability to create larger scale scaffolds, as they are limited by the size of the plant source. Moreover, plant derived scaffolds for BTE might be limited to non-load bearing applications due to their mechanical properties[164]. Chemically, cellulose is a polymer consisting of linearly repeating glucose units forming β(1->4) glycosidic bonds. Individual cellulose chains can link one another via hydrogen bonds forming fibrillar bundles ranging in the few

hundred micrometers[86]. Cellulose nanofibrils (CNF) are a type of cellulose derivative obtained from mechanical separation and homogenization of cellulose fibers, which produces fibrils of few nanometers in width and a few micrometer in length[90]. Due to their chemical inertness, biocompatibility, and availability, cellulose-based biomaterials are being used for certain BTE applications. CNFs derivatives have been used in various BTE applications as hydrogel components and proven to be biocompatible[90]. However, CNFs are insoluble in water, and can only be dissolved in certain class of solvents (e.g. ionic liquids; alkali solvents; polar aprotic solvents[166]), which limits their use for BTE. Due to the presence of hydroxyl groups within their chemical structure, CNFs can be chemically modified[86,167].

In recent years, several groups have developed scaffolds for BTE using additive manufacturing (3D printing)[168]. One of the emerging 3D printing technique is digital light processing (DLP) UV 3D printing. DLP printing consists of illuminating a photo-cross linkable resin with ultraviolet light, forming a patterned solid. This patterned solid can be custom-made using computer-assisted design (CAD). Researchers have shown the potential of UV-curable polysaccharides (e.g., starch[163]; carboxymethyl cellulose[169]) or proteins (e.g., silk[170]; gelatin[171]) that incorporate methacrylate groups in their chemical structure for bioengineering purposes. Here, we propose a method where CNF can be modified to become a water-soluble, UV curable resin using glycidyl methacrylate (GMA). This aqueous resin can be cross-linked by exposure to UV light and be used as an “ink” for DLP UV 3D printing to create structured hydrogels. The hydrogels were further processed to create aerogels and their applicability for BTE was demonstrated in a proof-of-concept *in vitro* study.

Here, we characterize some of the physio-chemical properties of this UV curable cellulose derivative (mCNF). Spectroscopic data revealed the chemical reaction of GMA with ethylenediamine-modified CNF. Furthermore, we have demonstrated that mCNF resin photo crosslinked into hydrogels, with customized shape, using casting methods and DLP UV 3D

printing. Freezing and lyophilization of hydrogels created porous aerogels. Pore size of aerogels were distributed within range of optimal pore size for BTE scaffold. This had the positive effect of aerogels being able to absorb cell culture media and fully rehydrate. Mechanical analysis revealed that modulating the resin concentration influences the storage modulus, Young's modulus and compressive strength. The higher concentration also led to a more brittle hydrogel. Creating a custom-shaped aerogel with a porous structure and modulable mechanical properties can potentially have an advantage when used as a BTE scaffold. Thus, we hypothesized that disk-shaped aerogels can be used as a scaffold for BTE applications. Aerogels were seeded with MC3T3-E1 pre-osteoblast cells and cultured to proliferate for 1 week. Thereafter, we chemically induced osteoblastic differentiation over a 4-week period. Results showed that samples cultured in osteogenic-inducing media were showing visible signs of mineralization. Histological analysis revealed that the pore walls of the scaffolds were mineralized by the differentiated cells. Mineral deposition significantly increased the Young's modulus of the aerogels up to 78.29 ± 19.46 kPa, compared to control (17.66 ± 3.55 kPa). Mineral content in the aerogels was analysed after the 4-week differentiation period and revealed that aerogels incubated with differentiated osteoblasts had a significantly higher mineral content than the control group. Moreover, elemental analysis of the mineral content revealed the increased presence of phosphorus and calcium, common elements found in apatite.

Taken all together, chemical, and mechanical characterisation of the mCNF resin shows a material with potential for DLP 3D printing applications. Moreover, interesting results shows that constructed aerogels can be use for BTE applications.

6.4. Materials and Methods

6.4.1. Reagents

Cellulose nanofibrils (CNF; Cellulose Lab, Cat no: CNF-FD); Dimethylacetamide (DMAc; Sigma, Cat no: 271012); Lithium Chloride (LiCl; Sigma, Cat no: L9650); Triethylamine (TEA: Sigma Cat no: 471283); p-toluenesulfonyl chloride (Tosyl; Sigma, Cat no: 240877); DMSO (Sigma, Cat no: 276855); Ethylenediamine (EDA; Sigma, Cat no: E26266); Glycidyl methacrylate (GMA; Sigma, Cat no: 779342); 1-ethyl-3-(3-dimethylaminopropyl)carbodiimide hydrochloride (EDC; ThermoFisher, Cat no: 22981); N-hydroxysuccinimide (NHS; ThermoFisher, Cat no: 24500); Lithium phenyl-2,4,6-trimethylbenzoylphosphinate (LAP; Sigma, Cat no: 900889).

6.4.2. Preparation of methacrylated nanofibrillar cellulose resin (mCNF)

Lyophilised CNFs were placed in a 250 ml round bottom flask with in dimethylacetamide in a 1:50 ratio, respectively. The temperature of mixture was brought to 115°C for 15min. Lithium Chloride (LiCl) was added in a 4:1 ratio with respect to CNF, under vacuum at 100°C until full dissolution of LiCl. After dissolution, the mixture was slowly cooled down to room temperature. Tosylation was performed in similar fashion as previously demonstrated by other groups[172,173]. Briefly, 2.61mM of triethylamine (TEA) and 13.11mM of Tosyl were added to the mixture. The solution was allowed to react for 24h by stirring at room temperature. The resulting solution was precipitated in 99% ethanol and filtered under vacuum to remove solvent. Five grams of solid phase was dissolved in 20 mL DMSO. Once dissolved, 44.9mM of ethylenediamine (EDA) was added and the mixture was stirred for 24h at 75°C. The resulting solution was precipitated in cold 99% ethanol and filter under vacuum to remove solvent. The solid phase was dissolved in dH_2O at a 1:10 ratio, respectively. 18.91 mM of glycidyl methacrylate (GMA), 11.27mM of EDC and 2.61mM of NHS were added. The solution was stirred at 75°C for 24h before precipitation in cold 99% ethanol and centrifugation. The resulting solid (mCNF) was dissolved in dH_20 at different

concentrations (0.1 g/mL or 0.5 g/mL). A photo initiator (LAP) was added at 0.2% w/v. The resin was kept at room in dark.

6.4.3. mCNF FTIR and NMR characterisation

Samples were frozen at -80°C overnight and lyophilized for 24h before Fourier-transform infrared spectroscopy (FTIR) and solid-state Nuclear magnetic resonance (NMR) analysis. FTIR spectrum were recorded with a Nicolet 6700 AT-FTIR from 4000 to 500 cm^{-1}. Solid state Carbon-13 Magic angle spinning NMR spectra were recorded with a Bruker Avance III 200. NMR spectra were collected at a 200 MHz frequency.

6.4.4. Hydrogels and Aerogels fabrication and surface characterisation

Hydrogels were constructed by exposing mCNF resin (0.5 g/mL) with UV light. Disk-shaped hydrogels were constructed by pipetting 50 uL of the resin into 6mm diameter Teflon molds. The constructs were exposed for 10 min with a 4 Watts, 405 nm light.

Aerogels were constructed by lyophilizing the hydrogel constructs. Disk-shape hydrogels were frozen at -80°C for 24h. Frozen hydrogels were placed in a lyophilizer at 0.015 mBar and -80°C for 24 hours, resulting in a porous aerogel. Aerogels were rehydrated by pipetting 10 μL of cell culture media on the aerogels until reabsorption.

Scanning Electronic microscopy (SEM) was performed to observe the surface features of hydrogels and aerogels. Hydrogels were serially dried in increasing concentration of ethanol, from 70% to 99%. Hydrogels in ethanol were dried in a critical point dryer following manufacturer's protocol. Hydrogels and aerogels were coated with a 9nm gold layer before SEM imaging. Images were acquired with a JEOL JSM-7500F FESEM scanning electron microscope at 85x magnification (N=3 for hydrogels; N=3 for aerogels).

Porosity measurements of aerogels was performed using histological sectioning and image analysis. Rehydrated aerogels were fixed with 10% formalin for 30 min and placed in 70% ethanol. This fixation step is meant to minimize variables by keeping the same protocol as for cell processing. Paraffin embedding and staining of the sample sectioning (4 µm thick) was performed by the PALM Histology Core Facility at the University of Ottawa. Slides were stained with Masson Trichrome and images were acquired with a Zeiss AXIOVERT 40 CFL microscope at a 40X magnification. A 555 by 555 μm^2 region of interest (ROI) was randomly selected on samples and the images were thresholded using ImageJ software to highlight pores in the samples. The pore size was registered as the major axis (N=6 samples; 3 ROI per sample).

To demonstrate the possibility of three-dimensional printing with the resin, cubes and haystack hydrogels were printed using the LumenX UV DLP printer by pipetting 1 mL of mCNF resin (0.5 g/mL) in the printing vat. Each layer was exposed for 10s with 405 nm light at maximum laser power.

6.4.5. Mechanical characterisation of mCNF, hydrogel and aerogel

Rheometric analysis was performed to evaluate crosslinking kinetics, storage modulus and yield point using a rheometer (Anton Paar GmbH) equipped with a 100mW, 405 laser diode. Oscillating sheer stress was applied to the mCNF solutions to evaluate crosslinking kinetics and storage modulus plateau after periodic UV illumination. Briefly, 60 µl of mCNF at different concentration (0.1 g/mL; 0.5 g/mL) was pipetted on the glass surface of the rheometer, equipped with parallel plates configuration. Samples were kept hydrated by pipetting the outer part of the apparatus with a 0.2% LAP solution in dH20. Samples were exposed to 405nm light for 1 min and oscillating sheer stress was applied at fixed amplitude (0.25% in 30 sec) for 210s. Then, the samples were again exposed to 405 UV light for 1 min and oscillating sheer-stress was re-applied with the same conditions. The illumination/sheer-stress cycle was repeated 5 times.

Amplitude sweep was performed in similar fashion, with sample incrementally strained until a breaking point is observed, corresponding to the yield point. Briefly, 60 μl of mCNF resin at different concentrations (0.1 g/mL; 0.5 g/mL) was pipetted on the glass surface and was illuminated with 405 nm light for 5 minutes. Samples were sheared at fixed frequency (1 Hz) with an increasing sheer amplitude until a breakpoint was observed.

Young's moduli (YM) of both hydrogels and aerogels, at different concentrations (0.1 g/mL; 0.5 g/mL) were measured in a uniaxial compression experiment. Samples ($N \geq 3$ for each experimental conditions) were compressed at 1%/sec and the resulting force-displacement was recorded using a CellScale UniVert (CellScale, Waterloo, ON). YM were obtained by fitting the linear portion of the stress-strain curve. Compressive strength was obtained by compressing the sample until brittle fracturing occurred. Compressive strength was recorded as peak force before failure.

6.4.6. Cell Culture and Differentiation

Disk-shape aerogels were constructed as previously described. Aerogels (0.5 g/mL) were used as scaffolds for pre-osteoblast cell culture and differentiation. Prior to seeding on aerogel disks, MC3T3-E1 Subclone-4 pre-osteoblast cells (ATCC® CRL-2593™) were cultured in Minimum Essential Medium with addition of 10% fetal bovine serum (FBS) and 1% penicillin/streptomycin (α-MEM). Cells were tryspinized and resuspended in a 40 μL aliquot containing 10^6 cells. Each aliquot was pipetted on the surface of the scaffolds in a 96-well plate. Cells were left to adhere for 1h in cell culture conditions. Then, 200 μL of α-MEM were added to each culture well. Culture medium was changed every 3 to 4 days, for 7 days. Osteoblastic differentiation of MC3T3-E1 cells was induced by adding 50 μg/mL of ascorbic acid and 10 mM β-glycerophosphate to α-MEM (osteogenic differentiation medium, OM). OM was changed every

3 to 4 days, for 4 weeks. Control group was cultured in α-MEM for the same period of time with similar medium renewal frequency.

Mineral deposits were assessed by histological sectioning and staining (N=3 per incubation condition). Cell-seeded aerogels were fixed after 4 weeks of incubation in either OM or α-MEM, with 10% formalin for 30 min and placed in 70% ethanol. Paraffin embedding and staining was performed as previously described. Slides were stained with Von Kossa/Van Geison (VK), which highlight calcium deposition. Images were acquired with a Zeiss AXIOVERT 40 CFL microscope at a 40X magnification.

To assess mechanical changes of the cell-seeded aerogels due to MC3T3-E1 differentiation, YM of the samples were measured after 4 weeks of incubation in either OM or α-MEM. Similarly, as previously described, samples (N=3 per incubation condition) were compressed at 1%/sec rate using the CellScale UniVert (CellScale). The resulting YM was taken by fitting the linear portion for the stress-strain curve.

6.4.7. Mineralization Analysis of cell-seeded aerogels

Mineralization of the cell-seeded aerogels were assessed by Alizarin Red S (ARS) and Energy-dispersive spectroscopy (EDS) after 4 weeks of incubation in either OM or α-MEM. Cell-seeded aerogels, after 4 weeks of incubation in either OM or α-MEM (N=3 per incubation condition) were fixed with 10% formalin for 30 min and washed with deionized water. Thereafter, samples were stained with a 2% ARS (pH=4.1) solution for 45 min at room temperature. Samples were then thoroughly washed with deionized water to remove excess staining and placed in 15 mL conical tubes with 10 mL of deionized water. Tubes were placed on an orbital shaker at 120 rpm for 1h, periodically renewing dH_2O every 15 min. Samples were imaged with a Nikon SMZ1270 stereomicroscope with dark-red staining indicating calcium deposits. Thereafter, ARS-stained samples were processed for optical calcium quantification, following established

protocol[149]. Briefly, stained samples were incubated in 800 µL of 10% acetic acid solution for 30 min with light agitation. The solution was transfer to 1.5 mL tubes and centrifuged at 17 x 10^4 g for 15 min and 500 µL of supernatants were collected and transfer to a new tube with 200 µL of 10% ammonium hydroxide. From this solution, 150 µL was collected and transfer to a 96-well plate. The 405nm absorption was read with an automated plate reader, with each sample read in triplicate.

Moreover, cell-seeded aerogels (N=3 per incubation condition) were fixed with 10% formalin for 30 min and dehydrated in increasing concentration of ethanol (from 70% to 99%). Samples were processed in a critical-point dryer and were coated with an 9nm layer of gold. Surface analysis of the samples was obtained with Energy-dispersive spectroscopy (EDS) to observe the presence of Phosphorus (P) and Calcium (Ca).

6.4.8. Statistical analysis

Data are reported as mean ± standard error of the mean. One-way ANOVA was performed as statistical followed by Tukey post-hoc tests for YM mean comparison at different concentrations. Two-sample T-test was performed for Compressive Strength and mineralisation mean comparison. A value of $p < 0.05$ was considered to be statistically significant.

6.5. Results

6.5.1. Preparation of methacrylated nanofibrillar cellulose resin (mCNF)

Methacrylated cellulose nanofibrils were first synthetized by reacting glycidyl methacrylate with ethylenediamine-modified CNFs (Figure 6.1 A). The CNFs were dissolved in a DMAc/LiCl system and were allowed to react with p-toluene sulfonyl chloride (Figure 6.1 B). The obtained solid had a tosyl group on the C-6 carbon of the cellulose chain (Figure 6.1 B). Then, the recovered solid was dissolved in DMSO and allow to react with ethylenediamine, to substitute

with the tosyl group (Figure 6.1 B). After precipitation of the mixture in ethanol, we recover a granular solid. Then, the ethylenediamine-modified CNFs were dissolved in water and allowed to react with glycidyl methacrylate. The resulting solid was dissolved in water at different concentrations, with addition of LAP, to form UV curable mCNF resin. To analyse the reaction process, each product from the intermediary and final reaction were analysed with FTIR and NMR spectroscopy.

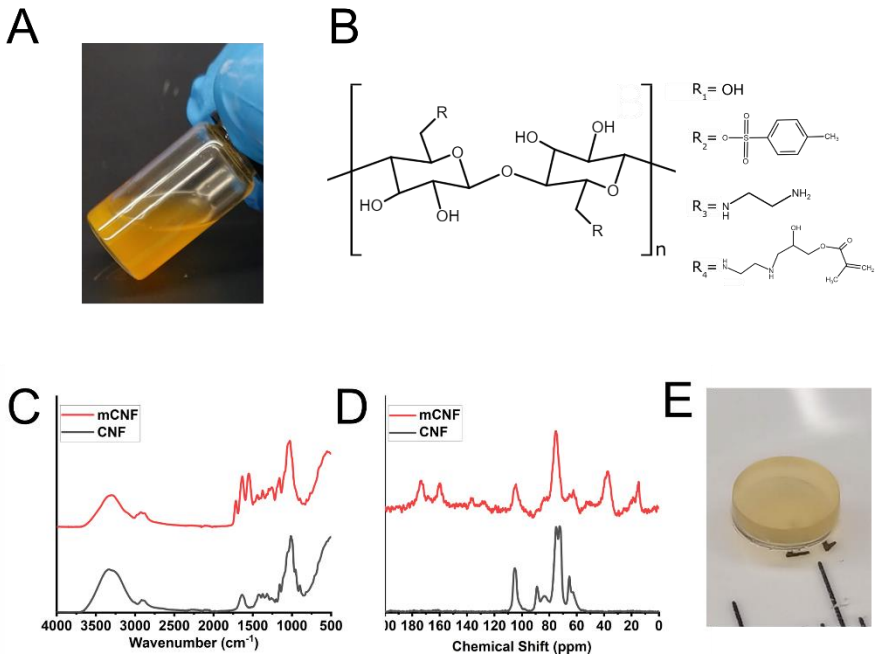

Figure 6.1: (A) mCNF in solution at 0.5 g/mL. (B) Synthesis of mCNF at different reactions (R1= pristine CNF; R2= after tosylation; R3= after substitution with ethylenediamine; R4= after reaction with GMA). (B) FTIR spectra of pristine CNF (black) and mCNF (red). FTIR spectrum were recorded from 4000 to 500 cm-1. (C) NMR spectra of pristine CNF (black) and mCNF (red). NRM Spectrum were recorded from 200 to 0 ppm. (E) Disk-shape hydrogel.

6.5.2. mCNF FTIR and NMR characterisation

We examined the synthesis of mCNF with FTIR spectroscopy and Carbon-13 NMR spectroscopy. FTIR spectra analysis was used to analyse the modification steps (Figure S6.1 A) and the reaction of glycidyl methacrylate with the ethylenediamine-modified CNF (Figure 6.1 C). Modification of pristine CNF with tosyl group by the apparition of peaks at 815 cm^{-1}, 1175 cm^{-1}

and 1350 cm^{-1}, representing C-H bending in the aromatic ring and S=O stretching. Substitution of the tosyl group by the ethylenediamine linker was confirmed by the disappearance of the tosyl peaks and the apparition of a peak at 1580 cm^{-1} indicating N-H bending vibrations (Figure S6.1 A). Peaks at 3300 cm^{-1} and 2915 cm^{-1} are visible for both mCNF resin and pristine CNF, showing characteristic alcohol group and alkane stretching vibrations, respectively. At 1012 cm^{-1}, characteristic C–C stretching vibrations of pyranose rings of cellulose nanofibrils are shifted towards 1025 cm^{-1} for mCNF (Figure 6.1 C). Alcohol group bending is also visible for both curves at around 1632 cm^{-1}. New absorption peaks are visible for the mCNF curve at 1714 cm^{-1} and 1550 cm^{-1}.

To further confirmed the chemical modifications of mCNF, we performed Carbon-13 solid-state NMR spectroscopy for the modification steps (Figure S6.1 B) and the reaction of glycidyl methacrylate with the ethylenediamine-modified CNF (Figure 6.1 D). Spectra of pristine CNF is showing characteristic carbon chemical shifts of cellulose at 105.2 ppm; 88.9 ppm; 75.0 ppm, 72.5 ppm and 65.3 ppm; 62.7 ppm, representing C-1; C-4; C-2, C-3, C-4; C-6 on the cellulose chain. Spectra showed that the replacement of the hydroxyl group by a tosyl group occurred mainly at Carbon-6 of the cellulose chain, represented by a decrease in intensity of the 62.7 ppm signal and apparition of aromatic signals at 129.9 ppm and 146.7 ppm, and a methyl group at 21.9 ppm (Figure S6.1 B). Furthermore, substitution of the tosyl group by ethylenediamine was confirmed with the diminution of aromatic and methyl signals, and the addition of CH_2 chemical shift at 40.6 ppm and 49.6 ppm (Figure S6.1 B). At 173.33 ppm and 160.12 ppm of the mCNF spectra (Figure 6.1 D), peaks of methacrylate carboxylic acid and carbon-oxygen double bonds are visible, respectively. Carbon-carbon double bond doublet is visible in the mCNF NMR spectra at 136.61 ppm and 127.75 ppm. Additionally, CH_2 signal from the attached ethylenediamine is visible at 37.17 ppm. Finally, methyl signal from the methacrylate group is visible at 14.78 ppm. FTIR and NMR data demonstrate the chemical modification of ethylenediamine-modified CNF

with GMA. Hydrogels and aerogels were created by exposing mCNF resin to ultraviolet light. Surface characterisation and porosity measurements were performed on the hydrogels and aerogels.

6.5.3. Hydrogel and aerogel fabrication and surface characterisation

Hydrogels were created in disk shape by casting the resin in molds (Figure 6.1 E). After pipetting mCNF resin (0.5 g/mL) into a Teflon mold and a 10 min exposure to 405 nm UV light, hydrogels were extracted to form disks of 6mm in diameter by 2 mm in height, which is suitable for critical-sized cranial defect for bone regeneration model[124].

Disk-shape aerogels were constructed by freezing the hydrogels at -80C for 24h and lyophilized for 24h at 0.015 mBar and -80C. This resulted in a porous construct (Figure 6.2 A). Aerogels were rehydrated by adding a droplet of culture media (Figure 6.2 A). Over a period of 30 seconds, the culture media completely infiltrated and rehydrated the aerogels.

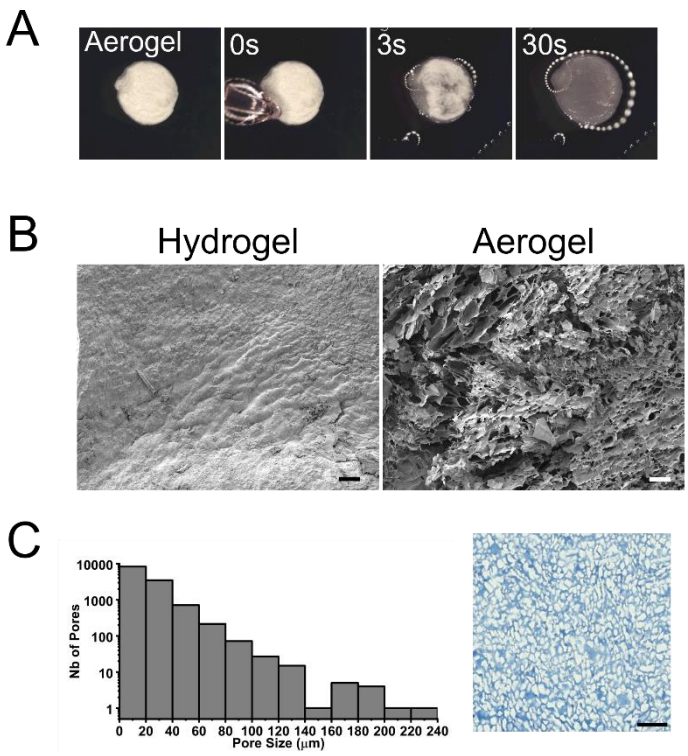

Figure 6.2: (A) Rehydration of mCNF aerogel over 30s: A drop of α-MEM is pipetted on the scaffold and which progressively absorbs the fluid. (B) Scanning electron microscopy micrographs of hydrogel and aerogel surface (Scale = 100 µm, applies for both). (C) Pore size distribution of aerogel, from histological section images (Scale = 50 µm).

SEM image analysis was used to evaluate the surface of the hydrogels and to observe the pore formation of the aerogels (Figure 6.2 B). Hydrogels are displaying an opaque, uneven surface. Freezing at -80°C and lyophilization of the hydrogels created a distinct porous structure that resulted in aerogels, with the removal of water from the constructs.

The internal porosity of the aerogels was quantified using histological sections and staining (Figure 6.2 C). Results showed an average pore size of 20.5 ± 0.1 µm, with a distribution of pore size between 6.5 µm and 228.8 µm. We observed a median pore size of 16 µm.

6.5.4. Mechanical characterisation of mCNF hydrogels and aerogels

A rheological study of mCNF resin was performed to evaluate crosslinking kinetics, storage modulus and yield point as a function of concentration and UV exposure. Storage

modulus and cross-linking kinetics were measured with a rheometer equipped with a 100 mW, 405nm laser diode (Figure 6.3 A). After the first 405 nm exposure, the storage modulus of the sample at 0.5 g/mL (31.5 ± 0.4 kPa) was significantly higher than at 0.1 g/mL (0.272 ± 0.002 kPa). This significant difference remained for all the exposures. We observed a significant increase (49-fold) in the final storage modulus of the 0.5 g/mL sample (71.5 ± 0.4 kPa) compared to the 0.1 g/mL sample (1.449 ± 0.002 kPa).

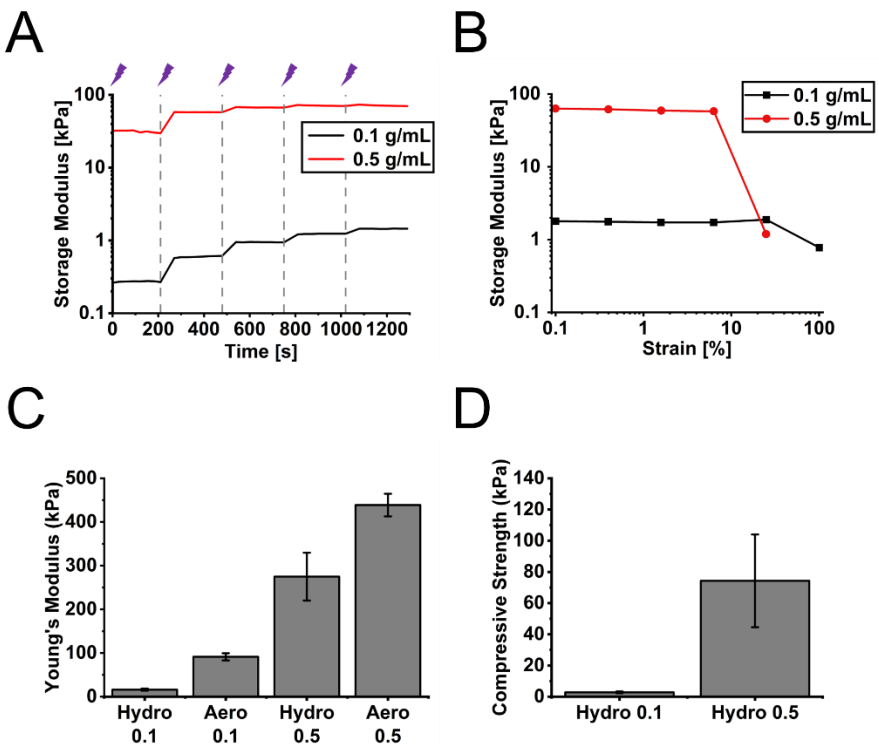

Figure 6.3: (A) Storage modulus as a function of time, with fixed sheer-stress amplitude (0.25% for 30 sec) for mCNF resin at 0.1g/mL (black) and 0.5g/mL (red) concentrations. Dotted lines represent 1 min illumination at 405nm. (B) Storage modulus as a function of applied strain of mCNF at 0.1g/mL (black) and 0.5g/mL (red) concentrations. (C) Young's modulus of hydrogels at 0.1g/mL and 0.5g/ml (Hydro 0.1 and Hydro 0.5, respectively) and aerogels at 0.1g/mL and 0.5g/ml (Aero 0.1 and Aero 0.5, respectively). (D) Compressive strength of hydrogels at 0.1g/mL and 0.5g/ml (Hydro 0.1 and Hydro 0.5, respectively).

Amplitude sweeps were measured after UV exposure for different concentration of mCNF until a yield point was observed (Figure 6.3 B). Results revealed a plateau in the storage modulus for both concentration of mCNF, below 5% strain. At 0.1 g/mL concentration of mCNF, we

observed a yield point at 25% strain. Alternatively, the increase of concentration resulted in a lower yield point: a brittle fracturing occurred at 6% strain for the 0.5 g/mL mCNF.

The uniaxial compression of mCNF hydrogels and aerogels at different concentrations was performed to measure the YM of the constructs (Figure 6.3 C). Results showed a significant increase in YM of the hydrogels with increasing concentration of mCNF (274.88 ± 54.8 kPa and 16.2 ± 2.2 kPa for 0.5 g/mL and 0.1 g/mL, respectively). Similarly, this significant increase in YM due to concentration was also observed for aerogels (438.70 ± 25.8 kPa and 91.36 ± 8.2 kPa, respectively). Results showed a non-significant increase in the YM between the hydrogels at 0.1 g/mL medium (16.2 ± 2.2 kPa) and the aerogels at 0.1 g/mL (91.36 ± 8.2 kPa; p=0.45). A significant increase in the YM was between the hydrogels and aerogels at 0.5 g/mL (274.88 ± 54.8 kPa and 438.70 ± 25.8 kPa, respectively). The compressive strength of hydrogels was measured as maximum stress before brittle fracturing, for 0.1 g/ml and 0.5 g/mL (Figure 6.3 D). Data showed a significant increase in the compressive strength of the 0.5 g/mL (74.30 ± 29.72 kPa) hydrogels compared to the 0.1 g/mL (2.78 ± 0.54 kPa) hydrogels. Due to their compliant nature, no compressive strength was observed in the aerogels, which deformed plastically until 100% strain. With higher YM and porous nature, aerogels were selected for cell culture and differentiation of MC3T3-E1 pre-osteoblast cells.

6.5.5. Cell Culture and Differentiation

Cell culture and differentiation was performed on disk-shaped aerogels. MC3T3-E1 cells are widely used as a model to characterize bone matrix mineralization and biomineralization[123] and were previously used to characterize mechanosensitive behavior on apple-derived scaffolds[164]. Cell culture suspension of MC3T3-E1 cells was pipetted directly on the aerogels. The scaffolds completely absorbed the cell suspension and cells were left to adhere for 1h. Osteoblastic differentiation of MC3T3-E1 cells was chemically induced by adding ascorbic acid and β-glycerophosphate to culture media and cells were allowed to differentiate for a period of 4

weeks. Cell-seeded aerogels cultured in osteogenic-inducing media displayed a white opaque coating, compared to the samples in regular culture media (Figure 6.4 A). This coloring could be attributed to signs of mineralization on the constructs by the differentiation of MC3T3-E1 cells. Further confirmation of mineralization was obtained with histological sectioning of the scaffolds after 4 weeks. VK staining for calcium revealed mineral deposits on pore walls of the samples incubated in OM (Figure 6.4 A). On the contrary, no mineral deposits were visible on pores walls for samples incubated in regular culture media and were only displaying pale pink coloring (Figure 6.4 A). Furthermore, differentiation of MC3T3-E1 cells had an impact on the YM of the aerogels.

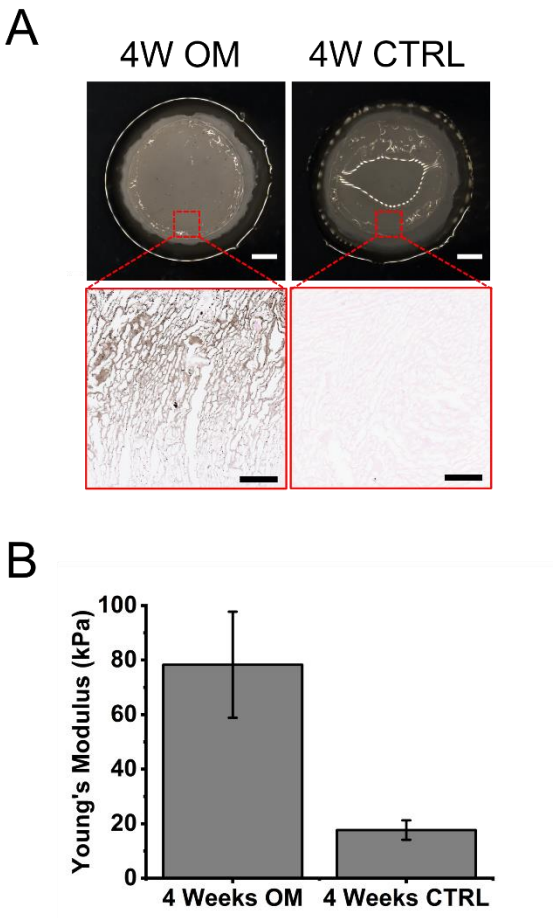

Figure 6.4: (A) Representative photographs of MC3T3-E1 seeded aerogels after 4 weeks of incubation in either osteogenic-inducing media (OM) or α-MEM (CTRL) (Scale = 1mm, applies for both). Histological sections of MC3T3-E1 cell seeded aerogels after 4 weeks of incubation in osteogenic-inducing media (OM) α-MEM (CTRL). Samples were stained with Von Kossa (VK) to highlight mineralization of the constructs

(Scale = 100 µm, applies for histological sections). (B) Young's modulus of MC3T3-E1 seeded aerogels after 4 weeks of incubation in either osteogenic-inducing media (OM) or α-MEM (CTRL).

The YM of the cell-seeded aerogels were measured after 4 weeks of incubation in either osteogenic-inducing medium (OM) or α-MEM (CTRL) (Figure 6.4 B). Results showed significant increase of the YM between the samples cultured in OM (78.29 ± 19.46 kPa) and the samples cultured in α-MEM (CTRL) (17.66 ± 3.55 kPa). Mineralisation of the scaffolds did have a significant influence on the YM of the hydrogels. Further investigation of the MC3T3-E1 differentiation was performed with ARS staining and EDS analysis

6.5.6. Mineralization Analysis of cell-seeded aerogels

Mineralization of cell-seeded aerogels was further evaluated by ARS staining, mineral quantification, and EDS analysis, after 4 weeks of incubation. Aerogels cultured in OM displayed strong, dark red coloration with ARS staining on localised aeras of the scaffolds (Figure 6.5 A). The other areas of the scaffolds stained also in red, but with less opacity. On the contrary, aerogels cultured in regular culture media did not display dark-red coloration after ARS staining (Figure 6.5 A). Mineral deposition was further evaluated by eluting the ARS-stained aerogels in an acetic acid solution. Results showed that samples incubated in OM had a significantly higher mineral content than samples incubated in α-MEM after 4-weeks (Figure 6.5 B, $p=2x10^{-6}$).

Furthermore, elemental analysis with EDS on the surface of cell-seeded aerogels was performed after 4 weeks incubation (Figure 6.5 C). Samples cultured in OM were displayed characteristic emission signals for phosphorus (2.0134 keV, P) and calcium (3.6905 keV, Ca). P and Ca signals were not observed for samples cultured in α-MEM, indicating that MC3T3-E1 were mineralizing the aerogels only when incubated in OM. These results on mineralisation revealed that mCNF aerogels can support osteoblastic differentiation.

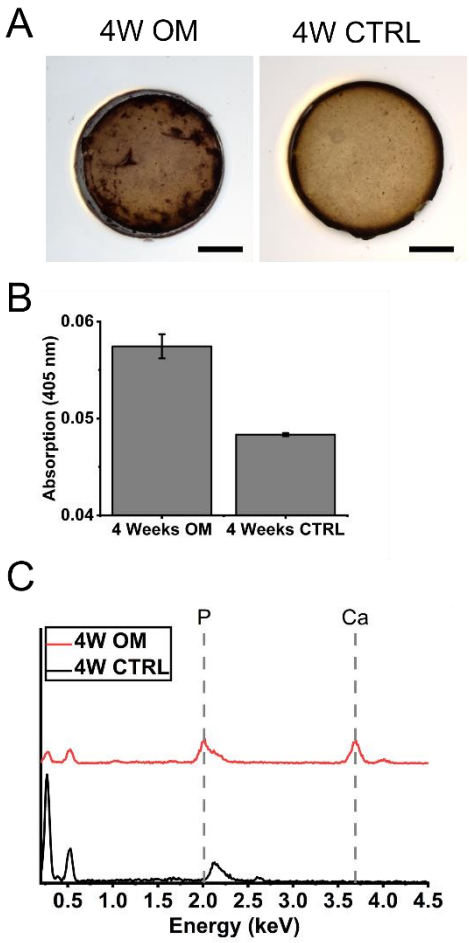

Figure 6.5: (A) Alizarin red S (ARS) staining of MC3T3-E1 seeded aerogels, after 4 weeks of incubation in either osteogenic-inducing media (OM) or α-MEM (CTRL). Calcium deposition (mineralization) of the constructs was highlighted by a red coloration (Scale = 2 mm, apply for both). (B) Mineral deposition was quantified with Alizarin Red S (ARS) staining after 4 weeks of incubation in either osteogenic-inducing media (OM) or α-MEM (CTRL). Values reported are the absorption at 405 nm. (C) Energy-dispersive spectroscopy spectra highlight the elemental composition of the surface of the cell-seeded mCNF hydrogels, in their respective culture media after 4 weeks of incubation. Peaks of phosphorus (2.0134 keV, P) and palcium (3.6905 keV, Ca) are indicated by dotted lines on the spectra.

6.6. Discussion

Cellulose, more precisely native plant cellulose, is a recent and disruptive type of material used for bioengineering[2,15–17,19,20]. Our group and others have shown that chemical removal of cellular components in plant tissues creates biocompatible and implantable scaffolds[4,15–17,19,20]. These scaffolds can also be tuned for tissue-specific applications[17], more specifically recent studies showed the potential use of apple-derived cellulose scaffolds as potential candidates for

BTE implants[4,164]. However, these types of scaffolds might be limited to non-clinical applications as they lack scalability and fine customization of mechanical properties. Currently, molecules harboring acrylate or methacrylate groups are commonly used as photo-curable solution, such as polyethylene glycol-diacrylate and methacrylated silk or gelatin[170,174,175]. In this study, we demonstrate the method of producing a novel cellulose derivative by highlighting some of its mechanical characteristics and application in a BTE. This cellulose derivative (mCNF) consists of methacrylated CNFs, where GMA is anchored to ethylenediamine-modified CNF (Figure 6.1 A). We have created hydrogels by exposing different concentrations of mCNF to UV light. Freezing and lyophilising the hydrogels lead to porous scaffolds.

Chemical modification of CNFs with glycidyl methacrylate was observed by FTIR spectroscopy (Figure 6.1 B). Results showed (Figure S6.1 A) the modification of CNF by tosylation and subsequent substitution with ethylenediamine was consistent with previous studies[176,177]. The presence of the methacrylate in mCNF is shown at 1025 cm^{-1}, highlighting the C-O-C linkages (Figure 6.1 C)[178]. This peak, and the slight signal shift compared to pristine CNF might be due to substitution of -OH group in the mCNF. Bending vibrations peak of alcohol group at 1632 cm^{-1} is visible for both curves. However, the increase in absorption seen in mCNF could be attributed to carbon-carbon stretching vibrations in the methacrylate group[179]. Further confirmation of the attachment of methacrylate group is seen by the carbon-oxygen stretching vibration in mCNF at 1714 cm^{-1} [180]. Moreover, linkage of the methacrylate group to the amino group is seen by the amine II band at 1550 cm^{-1} and amino bending vibrations 1580 cm^{-1} [180]. Taken altogether, the observation of the amino peaks, C=C and C=O peaks confirms the attachment of the glycidyl methacrylate to the CNF through the ethylenediamine link.

To further confirm the chemical modification, NMR spectroscopic analysis was performed (Figure 6.1 D). Typical chemical shifts of the cellulose carbons can be seen in the pristine CNF spectra. Spectral data was consistent with other studies where addition of ethylenediamine linker

is grafted to cellulose via tosyl substitution[172]. Addition of methacrylate group on the ethylenediamine linker was confirmed by the apparition of peaks of carbon-oxygen, carbon-carbon doublet and CH_3 (Figure 6.1 D). Furthermore, methylene signal from the amino linker also appeared in the spectra.

Hydrogels in different shapes were created by exposing mCNF resin to UV light. Disk-shape hydrogels were created by casting mCNF solution in teflon molds (Figure 6.1 E). This particular disk shape and size is commonly assessed in the rat critical-sized cranial defect for bone regeneration model[124]. Freeze-drying of hydrogel is a common technique to create pores[181]. Freezing at low temperature leads to the formation of ice crystals within the hydrogels[181]. The ice is removed by lyophilisation, which results in porous aerogels (Figure 6.2 A). Complete shape recovery of the initial hydrogel was observed once rehydrated with α-MEM (Figure 6.2 A). The α-MEM absorption by the aerogel was observed over 30s and displayed a sponge-like behavior. Furthermore, SEM images for both hydrogels and aerogels revealed the surface differences between the two constructs (Figure 6.2 B). Hydrogels possessed a flat, opaque surface with some surface topography. On the contrary, SEM imaging clearly demonstrate the porosity within the aerogels. With sectioning and histological staining, we measured an average pore diameter of 20.5 µm (Figure 6.2 C) in the aerogels. Creating voids in implant constructs for bioengineering, especially for bone tissue engineering is important because of increased surface area, ability for nutrient transport and increased mechanical properties[162]. Optimal pore diameter has been reported to be in the vicinity of 100 µm for BTE implants[129]. However, it has been demonstrated that smaller pore size can enhance osteoinductive properties of BTE scaffolds, by optimizing the surface area available for protein adsorption and improve cell attachment[129,182]. We observed a distribution ranging up to 229 µm, within the optimal range for BTE scaffolds. Other groups have shown results for BTE constructs with a broad range of pore sizes (few µm to mm range)[183]. In

comparison, the average pore size diameter observed in apple-derived cellulose scaffolds was observed to range from 73 µm to 288 µm, with an average pore diameter of 154 µm[184].

Rheological analysis was performed to evaluate cross-linking kinetics at different concentrations of mCNF. The storage modulus was significantly affected by the concentration of mCNF. Periodic irradiation with 405 nm UV light for 1 min resulted in a partial cross-linking, as illustrated by a stepwise increase in the storage modulus, for both concentrations (Figure 6.3 A). The step increase in the storage modulus was stronger for the first and second UV exposure, but the influence on cross-linking diminishes after a few exposures and reached a plateau for the 0.5 g/mL concentration. Similar behavior was observed in methacrylated starch hydrogels, cross-linked by UV light exposure[163], reaching similar magnitude in storage modulus as our cross-linked mCNF solution at highest concentration (10^4 Pa). Amplitude sweep revealed that the 0.5 g/mL mCNF hydrogels were more brittle compared to the lower concentration (Figure 6.3 B). Yield point was observed after 6% strain, as compared to 25% strain for the more compliant, lowest concentration. This result was comparable to co-polymer hydrogels of dimethyl aminoethyl methacrylate used for BTE[185]

Elastic and mechanical properties are an important factor in biomaterial design[186,187]. Results showed that mCNF hydrogels, at 0.1 g/mL, has a similar YM (Figure 6.3 C) to what has been reported in UV cured methacrylated starch[163], methacrylated silk[170] and methacrylated gelatin[174]. Moreover, results showed similar YM to UV curable hydrogels from gelatin-bone meal powder composite for BTE[188]. However, at 0.5g/mL, YM was significantly higher. These values fall within range of synthetic hydrogels like Poly(n-butyl-acrylate) and Poly(dimethyl siloxane), commonly used in bone bioengineering[187]. Compared to native cellulose scaffolds derived from apple tissue, hydrogels at 0.1g/mL shared a similar YM (31.6 ± 4.8 kPa [184]). At higher concentration, YM of the hydrogel is around 8-fold higher compared to these plant-derived scaffolds. This control over the YM is advantageous as it could be tuned for the desired tissue to replicate. Moreover, YM of

mCNF was increased after lyophilization. This increase was only significant for the higher concentration of aerogel. This discrepancy could be due to increased availability of cross-linking groups in the 0.5 g/mL, and, once exposed to UV light, a higher concentration of mCNF is crosslinked. This creates a hydrogel with a stronger crosslinked network of mCNF, thus having less non-crosslink mCNF in solution. Changes in the compressive strength values were observed by modulating the hydrogel concentration. The higher concentration yields a significantly higher compressive strength (Figure 6.3 D). Moreover, hydrogels underwent a brittle fracturing, as opposed to aerogels which did not fracture after full compression and deformed plastically.

As aerogels possessed a porous structure and better mechanical properties than the hydrogels, we decided to perform an *in vitro* cell culture proof-of-concept study with pre-osteoblast cells. We have cultured MC3T3-E1 cells on aerogels. Cell-seeded aerogels cultured in OM displayed white mineral deposits after 4 weeks of incubation, as compared to the control group (Figure 6.4 A). This observation of opaque mineral deposits was similar to previously demonstrated results using apple-derived cellulose scaffolds [184]. On a microscopic level, histological analysis and Von Kossa/Van Geisen staining for calcium deposits showed the mineralization of the samples by MC3T3-E1 cells. Samples cultured in OM showed positive, dark-brown staining (Figure 6.4 A), indicating the presence of calcium deposits within the scaffolds. The samples cultured in α-MEM only displayed a pale-pink coloration. This mineralisation of the scaffolds by the MC3T3-E1 cells also influenced the Young's modulus of the aerogels. Osteoblastic differentiation significantly increased (4-fold) the YM of the hydrogels (Figure 6.4 B). This increase might be due to the mineral deposits within the scaffolds, which directly results from differentiation of MC3T3-E1 cells. We observed a decrease in the YM between the standalone aerogel and the aerogels used for cell culture. This decrease can be attributed to the rehydration of the aerogel and the incubation period.

Further clue of MC3T3-E1 cells differentiation on cell-seeded aerogels constructs was observed by ARS staining (Figure 6.5 A). ARS stains calcium deposits, and is used as an indicator of osteoblastic differentiation[189]. Red-color staining was observed on the cell-seeded aerogels in OM compared to samples incubated in α-MEM (Figure 6.5 A). These appeared as isolated clumps on the scaffold. To assess the mineral deposition on the aerogels, residual ARS staining on the scaffolds was quantified using established methods[149]. We observed a significant increase in the mineral content in the cell-seeded aerogels incubated in OM compared to controls. This increase in mineral content was also noted by other groups using differentiated MC3T3-E1 on regenerated cellulose nanofiber[157]**,** differentiated human bone marrow stromal cells on 3D printed cellulose-base hydrogels[190] and differentiated human-induced pluripotent stem cells (hiPSCs) on apple-derive cellulose scaffold[4]. In addition to the strong red staining observed by ARS staining and quantification, EDS spectra was used to confirm the presence of calcium and phosphate on the surface of the aerogels (Figure 6.5 C). These signals are common for apatite-like mineralization, deposited by MC3T3-E1 cells after differentiation[123]. These signals were not observed on samples incubated in α-MEM. Similar data were observed by other groups using differentiated MC3T3-E1 cells[123]. Moreover, other group have observed phosphorus and calcium signals with differentiated hiPSCs on apple-derive cellulose scaffolds[4].

Tools such as DLP UV 3D printing could be used to create implantable devices that closely match the desired tissue to repair or replace. As this cellulose-based resin can be cured under UV light, we propose the idea that it can also be used for three-dimensional printing. We used UV DLP 3D printing to demonstrate the possibility of creating multiple shape at once, or complex shapes such as hydrogel cubes or haystack pattern (Figure S6.2). Shapes were printed using the LumenX UV DLP printer by pipetting 1 mL of mCNF resin (0.5 g/mL) in the printing vat. Each layer was exposed for 10s to 405 nm light. The printed resin resulted in solid shapes, resembling the original computer-assisted drawings (Figure S6.2). This type of printing is seen as the future tool

in regenerative medicine and tissue replacement, as it provides high resolution, scalability and can be used with a variety of resins (i.e., bio-inks)[175]. However future work will be required to assess the optimal printing parameters, mechanical properties and biological performance of the mCNF resin as a bio-ink.

6.7. Conclusion

Research on the development of plant-based biomaterials has demonstrated their applicability for BTE. However, some limitations with biomaterials directly sourced from plants have led us to develop an alternative that can be scaled up and allows for modulation of the mechanical properties. Here, we have developed a method to create hydrogels and aerogels with a UV curable cellulose nanofibril derivative. Culture and cell differentiation of MC3T3-E1 pre-osteoblast cells was performed with disk-shape aerogels. Results shows signs of mineralisation on the constructs by the cells. With the advancement of 3D printing technology there's a growing interest in developing curable inks for BTE. The UV curable mCNF resin presented in this study could eventually be used for rapid printing of bone implant, due to the mechanical properties and porosity of the resulting porous scaffold. Future work could investigate the *in vivo* biocompatibility and efficiency of porous mCNF aerogels, created by UV DLP 3D printing, in a rat critical size calvarial defect model, with the addition of bone-specific growth factors.

6.8. Acknowledgments

This work was supported by a Discovery Grant from the Natural Sciences and Engineering Research Council of Canada (NSERC) and a grant from the Li Ka Shing Foundation.

6.9. Supplementary figures

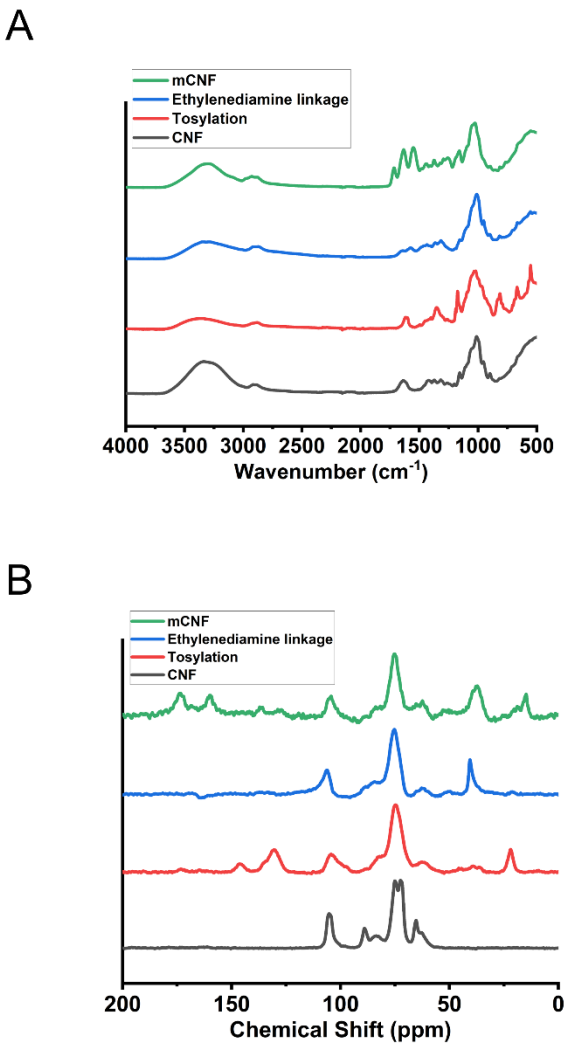

Figure S6.1: (A) FTIR spectra of pristine CNF (black), CNF after tosylation (red), after substitution with ethylenediamine (blue) and mCNF (green). (B) NMR spectra of pristine CNF (black), CNF after tosylation (red), after substitution with ethylenediamine (blue) and mCNF (green).

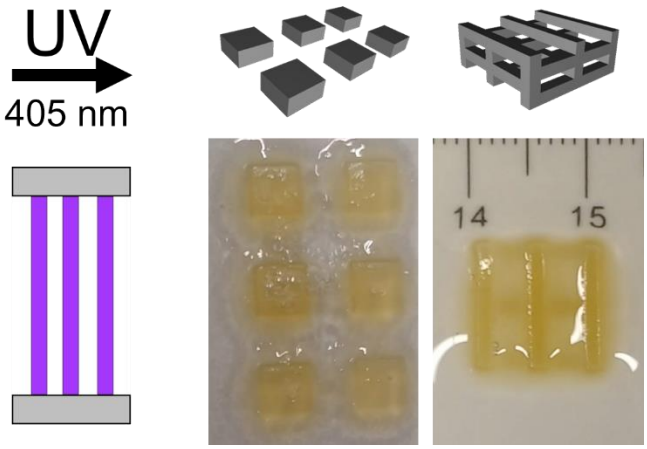

Figure S6.2: 3D printed: mCNF hydrogels in different shapes: Array of cubes; Three-dimensional grid.

Chapter 7:

Conclusion and future directions

The results presented in this work demonstrate once again the usefulness of plant-derived cellulose as a biomaterial. Moreover, they can be used for more specific applications, including BTE. In the fourth chapter of this thesis, it was demonstrated that apple-derived cellulose scaffolds can favorably accommodate the differentiation of pre-osteoblast cells, but due to their mechanical properties, their clinical use may be limited to non-loading conditions. In the fifth chapter, these same biomaterials were subjected to a cyclic force, similar to the stress due to human locomotion. The results, once again, demonstrate their potential for certain BTE applications. Finally, the sixth chapter proposes a different approach in the fabrication of cellulose-based biomaterial for BTE. In order to solve the scaling problem, as well as to gain control over the mechanical properties, hydrogel and aerogel scaffolds were created from cellulose derivative, reactive to ultraviolet light.

However, there are still some unanswered questions regarding the efficiency and scaling of the two types of cellulosic biomaterials presented in this work. In future studies, it would be interesting to review the re-engineering of apple-derived cellulose scaffolds. As demonstrated by previous studies, the functionalization of these biomaterials is possible and can improve cell adhesion and proliferation[17,19]. For example, it would be of interest to functionalize apple-derived cellulose scaffolds with proteins that promote stem cell differentiation into osteoblast cells (e.g., BMP-2). This could have the benefit of obtaining an increased cell density following *in vivo* implantation. Another point of interest would be the pre-mineralization of apple-derived cellulose scaffolds. Mineralization of the implant would have the advantage of positively modifying their mechanical properties, thus expanding the range of possible applications. Immersion in simulated body fluid is a common way to mineralize biomaterials for BTE applications, by depositing a layer of HA[191]. As demonstrated in Chapter 4, mineralized scaffolds (in situ) have a higher Young's modulus. It is therefore possible to hypothesize that pre-mineralized scaffolds will have more attractive mechanical properties, thereby reducing the risk of stress shielding and increasing bone regeneration *in vivo*.

Another relevant line of investigation, which is a continuation of Chapter 4, would be to study apple-derived cellulose scaffolds in a dynamic *in vivo* model. Although the conclusions of Chapter 4 recommend that the use of such biomaterials *in vivo* be limited to non-loading applications, some animal models, where stresses are present but relatively low, may provide more information on performance and efficiency. For example, unlike the cranial defect model presented in Chapter 4, implantation of a graft into a femoral condyle defect in rabbits is a procedure where physical constraint are present[192]. In addition, this model does not require an implant that supports the animal's weight, nor does it require an external fixator[192].

Finally, the results presented in Chapter 6 serve as a baseline for a new type of CNF-derived scaffold. Although the demonstration of their construction by 3D printing was briefly discussed in chapter 5, several questions remain unanswered. Future studies on this type of biomaterial could focus on the optimization of 3D printing. An optimistic hypothesis is to propose that an implant could be printed from medical imagery, to perfectly reproduce the original bone tissue. Although the biocompatibility and support for osteoblast cell differentiation was confirmed in this chapter, the in vivo efficacy remains to be demonstrated. The logical next step would be to study the aerogels presented in chapter 6 in a critical size cranial defect model in rat, similar to the protocol presented in chapter 4.

The safety of mammalian-derived biomaterials with respect to the risk of infection and transmission of infectious diseases is still a concern. Although health and safety requirements for bone implants have evolved in recent years to protect the well-being of the patient, risks of transmitted illness are always present. No surgical procedure is free of risk for the patient. However, risks of transmission of infectious diseases from human or animal strains are significantly reduced by the use of alternative implants, including those of cellulosic origin as presented in this work.

In terms of the ethical aspect of biomaterials, plant-based scaffolds offer a substantial alternative to their human and animal-based counterparts. Access to quality health care may be limited for vulnerable populations and developing countries. In particular, cost and accessibility of efficient biomaterials can be prohibitive in some developing regions. It would be of interest to establish a cost ratio of cellulose-derived biomaterials for BTE applications, and to do a comparison with commonly used materials and methods in orthopedic. Illegal organ trafficking is an ongoing problem in many parts of the world[193,194]. This includes the trafficking of bone tissue[194]. Although this problem is rooted in several social and economic factors, the availability of high-performance biomaterials at low cost may limit the use of illegally trafficked tissues and organs. From this perspective, cellulose-derived materials appear to be a viable option. Ethical issues are certainly of interest with the use of animal-sourced biomaterials. Animal welfare and health, the use of agricultural land as feedstock, and environmental impact are at the heart of this ethical questioning. It would be of future interest to produce a life cycle assessment report of cellulose-derived biomaterials for use in BTE. This would establish the economic and environmental cost-benefits compared to the use of animal by-products. Following the results demonstrated in this thesis, cellulose-derived biomaterials will definitely offer an interesting alternative in BTE in the future.

Chapter 8:

References

1. S, T., N, B. & J, B. Nonunion fractures, mesenchymal stem cells and bone tissue engineering. *J Biomed Mater Res A* **106**, 2552–2562 (2018).

2. Hickey, R. J. & Pelling, A. E. Cellulose biomaterials for tissue engineering. *Frontiers in Bioengineering and Biotechnology* vol. 7 45 Preprint at https://doi.org/10.3389/fbioe.2019.00045 (2019).

3. Torgbo, S. & Sukyai, P. Bacterial cellulose-based scaffold materials for bone tissue engineering. *Applied Materials Today* vol. 11 34–49 Preprint at https://doi.org/10.1016/j.apmt.2018.01.004 (2018).

4. Lee, J., Jung, H., Park, N., Park, S. H. & Ju, J. H. Induced Osteogenesis in Plants Decellularized Scaffolds. *Sci Rep* **9**, 1–10 (2019).

5. Contessi Negrini, N., Toffoletto, N., Farè, S. & Altomare, L. Plant Tissues as 3D Natural Scaffolds for Adipose, Bone and Tendon Tissue Regeneration. *Front Bioeng Biotechnol* **8**, (2020).

6. Harris, A. F., Lacombe, J. & Zenhausern, F. The Emerging Role of Decellularized Plant-Based Scaffolds as a New Biomaterial. *Int J Mol Sci* **22**, (2021).

7. Zhu, Y. Zhang, Q., Wang, S., Zhang, J., Fan, S., & Lin, X. Current Advances in the Development of Decellularized Plant Extracellular Matrix. *Front Bioeng Biotechnol* **9**, 650 (2021).

8. Bilirgen, A. C., Toker, M., Odabas, S., Yetisen, A. K., Garipcan, B., & Tasoglu, S. Plant-Based Scaffolds in Tissue Engineering. *ACS Biomater Sci Eng* **7**, 926–938 (2021).

9. Wang, Y., Dominko, T. & Weathers, P. J. Using decellularized grafted leaves as tissue engineering scaffolds for mammalian cells. *In Vitro Cellular and Developmental Biology - Plant* **56**, 765–774 (2020).

10. Cheng, Y. W., Shiwarski, D. J., Ball, R. L., Whitehead, K. A. & Feinberg, A. W. Engineering Aligned Skeletal Muscle Tissue Using Decellularized Plant-Derived Scaffolds. *ACS Biomater Sci Eng* **6**, 3046–3054 (2020).

11. Toker, M., Rostami, S., Kesici, M., Gul, O., Kocaturk, O., Odabas, S., & Garipcan, B. Decellularization and characterization of leek: a potential cellulose-based biomaterial. *Cellulose* **27**, 7331–7348 (2020).

12. S. H, A., Mohan, C. C., P.S, U., Krishnan, A. G. & Nair, M. B. Decellularization and oxidation process of bamboo stem enhance biodegradation and osteogenic differentiation. *Materials Science and Engineering: C* **119**, 111500 (2021).

13. Robbins, E. R., Pins, G. D., Laflamme, M. A. & Gaudette, G. R. Creation of a contractile biomaterial from a decellularized spinach leaf without ECM protein coating: An in vitro study. *J Biomed Mater Res A* **108**, 2123 (2020).

14. Dikici, S., Claeyssens, F. & MacNeil, S. Decellularised baby spinach leaves and their potential use in tissue engineering applications: Studying and promoting neovascularisation. *J Biomater Appl* **34**, 546–559 (2019).

15. Modulevsky, D. J., Cuerrier, C. M. & Pelling, A. E. Biocompatibility of Subcutaneously Implanted Plant-Derived Cellulose Biomaterials. *PLoS One* **11**, e0157894 (2016).

16. Modulevsky, D. J., Lefebvre, C., Haase, K., Al-Rekabi, Z. & Pelling, A. E. Apple derived cellulose scaffolds for 3D mammalian cell culture. *PLoS One* **9**, e97835 (2014).

17. Hickey, R. J., Modulevsky, D. J., Cuerrier, C. M. & Pelling, A. E. Customizing the Shape and Microenvironment Biochemistry of Biocompatible Macroscopic Plant-Derived Cellulose Scaffolds. *ACS Biomater Sci Eng* **4**, 3726–3736 (2018).

18. Modulevsky, D. J., Cuerrier, C. M., Leblanc Latour, M., Hickey, R. J., Obhi, R.-J. K., Shore, I., Galuta, A., Walker, K. L. A., Tsai, E. C., & Pelling, A. E. Plant Scaffolds Support Motor Recovery and Regeneration in Rats after Traumatic Spinal Cord Injury. *bioRxiv* 2020.10.21.347807 (2022) doi:10.1101/2020.10.21.347807.

19. Fontana, G., Gershlak, J., Adamski, M., Lee, J.-S., Matsumoto, S., Le, H. D., Binder, B., Wirth, J., Gaudette, G., & Murphy, W. L. Biofunctionalized Plants as Diverse Biomaterials for Human Cell Culture. *Adv Healthc Mater* **6**, 1601225 (2017).

20. Gershlak, J. R., Hernandez, S., Fontana, G., Perreault, L. R., Hansen, K. J., Larson, S. A., Binder, B. Y. K., Dolivo, D. M., Yang, T., Dominko, T., Rolle, M. W., Weathers, P. J., Medina-Bolivar, F., Cramer, C. L., Murphy, W. L., & Gaudette, G. R. Crossing kingdoms: Using decellularized plants as perfusable tissue engineering scaffolds. *Biomaterials* **125**, 13–22 (2017).

21. Lee, J. C. & Volpicelli, E. J. Bioinspired Collagen Scaffolds in Cranial Bone Regeneration: From Bedside to Bench. *Advanced Healthcare Materials* vol. 6 Preprint at https://doi.org/10.1002/adhm.201700232 (2017).

22. Mohan Iyer, K. Anatomy of Bone, Fracture, and Fracture Healing. *General Principles of Orthopedics and Trauma* 1–17 (2019) doi:10.1007/978-3-030-15089-1_1.

23. Bates, P., Moller-Madsen, B., Noorani, A. & Ramachandran, M. Basics of Bone. *Basic Orthopaedic Sciences* 193–203 (2018) doi:10.1201/9781315117294-13.

24. Morgan, E. F., Barnes, G. L. & Einhorn, T. A. The Bone Organ System: Form and Function. *Osteoporosis: Fourth Edition* 3–20 (2013) doi:10.1016/B978-0-12-415853-5.00001-7.

25. Fuchs, R. K., Warden, S. J. & Turner, C. H. *Bone anatomy, physiology and adaptation to mechanical loading*. *Bone Repair Biomaterials* (Elsevier Inc., 2009). doi:10.1533/9781845696610.1.25.

26. Kodama, H., Amagai, Y., Sudo, H., Kasai, S. & Yamamoto, S. Establishment of a clonal osteogenic cell line from newborn mouse calvaria. *Japanese Journal of Oral Biology* **23**, 899–901 (1981).

27. Bonewald, L. F. & Johnson, M. L. Osteocytes, mechanosensing and Wnt signaling. *Bone* vol. 42 606–615 Preprint at https://doi.org/10.1016/j.bone.2007.12.224 (2008).

28. Doro, D. H., Grigoriadis, A. E. & Liu, K. J. Calvarial Suture-Derived Stem Cells and Their Contribution to Cranial Bone Repair. *Front Physiol* **8**, 956 (2017).

29. Brown, R., Sanghrajka, A. & Eastwood, D. Skeletal Embryology and Limb Growth. *Basic Orthopaedic Sciences* 35–49 (2018) doi:10.1201/9781315117294-3.

30. van der Meulen, M. C. H. & Hernandez, C. J. Adaptation of skeletal structure to mechanical loading. in *Marcus and Feldman's Osteoporosis* 337–356 (Academic Press, 2021). doi:10.1016/B978-0-12-813073-5.00015-0.

31. Wolff, J. The Law of Bone Remodelling. *The Law of Bone Remodelling* (1986) doi:10.1007/978-3-642-71031-5.

32. Gao, X., Fraulob, M. & Haïat, G. Biomechanical behaviours of the bone-implant interface: A review. *J R Soc Interface* **16**, 20190259 (2019).

33. Huiskes, R., Weinans, H. & van Rietbergen, B. The relationship between stress shielding and bone resorption around total hip stems and the effects of flexible materials. *Clin Orthop Relat Res* **274**, 124–134 (1992).

34. Pountos, I. & Giannoudis, P. v. Fracture healing: Back to basics and latest advances. *Fracture Reduction and Fixation Techniques: Upper Extremities* 3–17 (2018) doi:10.1007/978-3-319-68628-8_1/FIGURES/4.

35. Andrzejowski, P. & Giannoudis, P. v. The 'diamond concept' for long bone non-union management. *Journal of Orthopaedics and Traumatology* vol. 20 Preprint at https://doi.org/10.1186/s10195-019-0528-0 (2019).

36. Yu, X., Tang, X., Gohil, S. v & Laurencin, C. T. Biomaterials for Bone Regenerative Engineering. *Adv Healthc Mater* **4**, 1268–1285 (2015).

37. Campana, V., Milano, G., Pagano, E., Barba, M., Cicione, C., Salonna, G., Lattanzi, W., & Logroscino, G. Bone substitutes in orthopaedic surgery: from basic science to clinical practice. *J Mater Sci Mater Med* **25**, 2445–2461 (2014).

38. Parikh, S. N. Bone graft substitutes: past, present, future. *J Postgrad Med* **48**, 142–148 (2002).

39. Bates, P., Yeo, A. & Ramachandran, M. Bone Injury, Healing and Grafting. *Basic Orthopaedic Sciences* 205–222 (2018) doi:10.1201/9781315117294-14.

40. Silber, J. S., Anderson, D. G., Daffner, S. D., Brislin, B. T., Leland, J. M., Hilibrand, A. S., Vaccaro, A. R., & Albert, T. J. Donor site morbidity after anterior iliac crest bone harvest for single-level anterior cervical discectomy and fusion. *Spine (Phila Pa 1976)* **28**, 134–139 (2003).

41. Fernández, R. F., Bucchi, C., Navarro, P., Beltrán, V. & Borie, E. Bone grafts utilized in dentistry: an analysis of patients' preferences. *BMC Med Ethics* **16**, 71 (2015).

42. Wang, W. & Yeung, K. W. K. Bone grafts and biomaterials substitutes for bone defect repair: A review. *Bioactive Materials* vol. 2 224–247 Preprint at https://doi.org/10.1016/j.bioactmat.2017.05.007 (2017).

43. Yoshikawa, H. & Myoui, A. Bone tissue engineering with porous hydroxyapatite ceramics. *Journal of Artificial Organs* **8**, 131–136 (2005).

44. Haugen, H. J., Lyngstadaas, S. P., Rossi, F. & Perale, G. Bone grafts: which is the ideal biomaterial? *J Clin Periodontol* **46**, 92–102 (2019).

45. Dorati, R., DeTrizio, A., Modena, T., Conti, B., Benazzo, F., Gastaldi, G., & Genta, I. Biodegradable Scaffolds for Bone Regeneration Combined with Drug-Delivery Systems in Osteomyelitis Therapy. *Pharmaceuticals* **10**, (2017).

46. Ghiasi, B., Sefidbakht, Y., Mozaffari-Jovin, S., Gharehcheloo, B., Mehrarya, M., Khodadadi, A., Rezaei, M., Ranaei Siadat, S. O., & Uskoković, V. Hydroxyapatite as a biomaterial–a gift that keeps on giving. *Drug Dev Ind Pharm* **46**, 1035–1062 (2020).

47. Arcos, D. & Vallet-Regí, M. Substituted hydroxyapatite coatings of bone implants. *J Mater Chem B* **8**, 1781–1800 (2020).

48. Sobczak-Kupiec, A., Drabczyk, A., Florkiewicz, W., Głąb, M., Kudłacik-Kramarczyk, S., Słota, D., Tomala, A., & Tyliszczak, B. Review of the Applications of Biomedical Compositions Containing Hydroxyapatite and Collagen Modified by Bioactive Components. *Materials 2021, Vol. 14, Page 2096* **14**, 2096 (2021).

49. Veiga, A., Castro, F., Rocha, F. & Oliveira, A. L. An update on hydroxyapatite/collagen composites: What is there left to say about these bioinspired materials? *J Biomed Mater Res B Appl Biomater* **110**, 1192–1205 (2022).

50. Kuttappan, S., Mathew, D. & Nair, M. B. Biomimetic composite scaffolds containing bioceramics and collagen/gelatin for bone tissue engineering - A mini review. *Int J Biol Macromol* **93**, 1390–1401 (2016).

51. Echave, M. C., Sánchez, P., Pedraz, J. L. & Orive, G. Progress of gelatin-based 3D approaches for bone regeneration. *J Drug Deliv Sci Technol* **42**, 63–74 (2017).

52. Costa-Pinto, A. R., Lemos, A. L., Tavaria, F. K. & Pintado, M. Chitosan and Hydroxyapatite Based Biomaterials to Circumvent Periprosthetic Joint Infections. *Materials 2021, Vol. 14, Page 804* **14**, 804 (2021).

53. Venkatesan, J. & Kim, S. K. Chitosan Composites for Bone Tissue Engineering—An Overview. *Marine Drugs 2010, Vol. 8, Pages 2252-2266* **8**, 2252–2266 (2010).

54. Venkatesan, J., Vinodhini, P. A. & Sudha, P. N. Chitin and Chitosan Composites for Bone Tissue Regeneration. *Adv Food Nutr Res* **73**, 59–81 (2014).

55. Farokhi, M., Mottaghitalab, F., Samani, S., Shokrgozar, M. A., Kundu, S. C., Reis, R. L., Fatahi, Y., & Kaplan, D. L. Silk fibroin/hydroxyapatite composites for bone tissue engineering. *Biotechnol Adv* **36**, 68–91 (2018).

56. Saleem, M., Rasheed, S. & Yougen, C. Silk fibroin/hydroxyapatite scaffold: a highly compatible material for bone regeneration. *http://www.tandfonline.com/action/journalInformation?show=aimsScope&journalCode=tsta20#.VmBmuzZFCUk* **21**, 242–266 (2020).

57. Bhattacharjee, P., Kundu, B., Naskar, D., Kim, H. W., Maiti, T. K., Bhattacharya, D., & Kundu, S. C. Silk scaffolds in bone tissue engineering: An overview. *Acta Biomater* **63**, 1–17 (2017).

58. Sun, L., Berndt, C. C., Gross, K. A. & Kucuk, A. Material fundamentals and clinical performance of plasma-sprayed hydroxyapatite coatings: A review. *J Biomed Mater Res* **58**, 570–592 (2001).

59. Zhang, A. M., Lenin, P., Zeng, R. C. & Kannan, M. B. Advances in hydroxyapatite coatings on biodegradable magnesium and its alloys. *Journal of Magnesium and Alloys* **10**, 1154–1170 (2022).

60. Asri, R. I. M., Harun, W. S. W., Hassan, M. A., Ghani, S. A. C. & Buyong, Z. A review of hydroxyapatite-based coating techniques: Sol–gel and electrochemical depositions on biocompatible metals. *J Mech Behav Biomed Mater* **57**, 95–108 (2016).

61. Ramesh, N., Moratti, S. C. & Dias, G. J. Hydroxyapatite–polymer biocomposites for bone regeneration: A review of current trends. *J Biomed Mater Res B Appl Biomater* **106**, 2046–2057 (2018).

62. Anita Lett, J., Sagadevan, S., Fatimah, I., Hoque, M. E., Lokanathan, Y., Léonard, E., Alshahateet, S. F., Schirhagl, R., & Oh, W. C. Recent advances in natural polymer-based hydroxyapatite scaffolds: Properties and applications. *Eur Polym J* **148**, 110360 (2021).

63. Zhang, Y., Shao, H., Lin, T., Peng, J., Wang, A., Zhang, Z., Wang, L., Liu, S., & Yu, X. Effect of Ca/P ratios on porous calcium phosphate salt bioceramic scaffolds for bone engineering by 3D gel-printing method. *Ceram Int* **45**, 20493–20500 (2019).

64. Chen, L., Wu, Z., Zhou, Y., Li, L., Wang, Y., Wang, Z., Chen, Y., & Zhang, P. Biomimetic porous collagen/hydroxyapatite scaffold for bone tissue engineering. *J Appl Polym Sci* **134**, 45271 (2017).

65. Heinemann, C., Brünler, R., Kreschel, C., Kruppke, B., Bernhardt, R., Aibibu, D., Cherif, C., Wiesmann, H. P., & Hanke, T. Bioinspired calcium phosphate mineralization on Net-Shape-Nonwoven chitosan scaffolds stimulates human bone marrow stromal cell differentiation. *Biomedical Materials* **14**, 045017 (2019).

66. Yeo, T., Ko, Y. G., Kim, E. J., Kwon, O. K., Chung, H. Y., & Kwon, O. H. Promoting bone regeneration by 3D-printed poly(glycolic acid)/hydroxyapatite composite scaffolds. *Journal of Industrial and Engineering Chemistry* **94**, 343–351 (2021).

67. Zhang, H., Mao, X., Du, Z., Jiang, W., Han, X., Zhao, D., Han, D., & Li, Q. Three dimensional printed macroporous polylactic acid/hydroxyapatite composite scaffolds for promoting bone formation in a critical-size rat calvarial defect model. *http://www.tandfonline.com/action/journalInformation?show=aimsScope&journalCode=tsta20#.VmBmuzZFCUk* **17**, 136–148 (2016).

68. Yang, Y., Chu, L., Yang, S., Zhang, H., Qin, L., Guillaume, O., Eglin, D., Richards, R. G., & Tang, T. Dual-functional 3D-printed composite scaffold for inhibiting bacterial infection and promoting bone regeneration in infected bone defect models. *Acta Biomater* **79**, 265–275 (2018).

69. Zhang, Y., Liu, X., Zeng, L., Zhang, J., Zuo, J., Zou, J., Ding, J., & Chen, X. Polymer Fiber Scaffolds for Bone and Cartilage Tissue Engineering. *Adv Funct Mater* **29**, 1903279 (2019).

70. Liu, X. & Ma, P. X. Polymeric Scaffolds for Bone Tissue Engineering. *Annals of Biomedical Engineering 2004 32:3* **32**, 477–486 (2004).

71. Wei, S., Ma, J. X., Xu, L., Gu, X. S. & Ma, X. L. Biodegradable materials for bone defect repair. *Military Medical Research* vol. 7 Preprint at https://doi.org/10.1186/s40779-020-00280-6 (2020).

72. Battafarano, G., Rossi, M., de Martino, V., Marampon, F., Borro, L., Secinaro, A., & Fattore, A. del. Strategies for Bone Regeneration: From Graft to Tissue Engineering. *International Journal of Molecular Sciences 2021, Vol. 22, Page 1128* **22**, 1128 (2021).

73. Donate, R., Monzón, M. & Alemán-Domínguez, M. E. Additive manufacturing of PLA-based scaffolds intended for bone regeneration and strategies to improve their biological properties. *E-Polymers* **20**, 571–599 (2020).

74. Li, Y., Liao, C. & Tjong, S. C. Synthetic Biodegradable Aliphatic Polyester Nanocomposites Reinforced with Nanohydroxyapatite and/or Graphene Oxide for Bone Tissue Engineering Applications. *Nanomaterials 2019, Vol. 9, Page 590* **9**, 590 (2019).

75. Grémare, A., Guduric, V., Bareille, R., Heroguez, V., Latour, S., L'heureux, N., Fricain, J. C., Catros, S., & le Nihouannen, D. Characterization of printed PLA scaffolds for bone tissue engineering. *J Biomed Mater Res A* **106**, 887–894 (2018).

76. Zhao, H., Li, L., Ding, S., Liu, C. & Ai, J. Effect of porous structure and pore size on mechanical strength of 3D-printed comby scaffolds. *Mater Lett* **223**, 21–24 (2018).

77. Sun, F., Sun, X., Wang, H., Li, C., Zhao, Y., Tian, J., & Lin, Y. Application of 3D-Printed, PLGA-Based Scaffolds in Bone Tissue Engineering. *International Journal of Molecular Sciences 2022, Vol. 23, Page 5831* **23**, 5831 (2022).

78. di Martino, A., Sittinger, M. & Risbud, M. v. Chitosan: A versatile biopolymer for orthopaedic tissue-engineering. *Biomaterials* vol. 26 5983–5990 Preprint at https://doi.org/10.1016/j.biomaterials.2005.03.016 (2005).

79. Wang, W. & Yeung, K. W. K. Bone grafts and biomaterials substitutes for bone defect repair: A review. *Bioactive Materials* vol. 2 224–247 Preprint at https://doi.org/10.1016/j.bioactmat.2017.05.007 (2017).

80. Yue, S., He, H., Li, B. & Hou, T. Hydrogel as a Biomaterial for Bone Tissue Engineering: A Review. *Nanomaterials* **10**, 1–25 (2020).

81. Amiryaghoubi, N., Fathi, M., Barar, J. & Omidi, Y. Hydrogel-based scaffolds for bone and cartilage tissue engineering and regeneration. *React Funct Polym* **177**, 105313 (2022).

82. Klemm, D., Heublein, B., Fink, H. P. & Bohn, A. Cellulose: Fascinating Biopolymer and Sustainable Raw Material. *Angewandte Chemie International Edition* **44**, 3358–3393 (2005).

83. Murizan, N. I. S., Mustafa, N. S., Ngadiman, N. H. A., Yusof, N. M. & Idris, A. Review on Nanocrystalline Cellulose in Bone Tissue Engineering Applications. *Polymers (Basel)* **12**, 1–22 (2020).

84. Gibson, L. J. The hierarchical structure and mechanics of plant materials. *J R Soc Interface* **9**, 2749–2766 (2012).

85. Janmohammadi, M., Nazemi, Z., Salehi, A. O. M., Seyfoori, A., John, J. v., Nourbakhsh, M. S., & Akbari, M. Cellulose-based composite scaffolds for bone tissue engineering and localized drug delivery. *Bioact Mater* **20**, 137–163 (2023).

86. Li, T., Chen, C., Brozena, A. H., Zhu, J. Y., Xu, L., Driemeier, C., Dai, J., Rojas, O. J., Isogai, A., Wågberg, L., & Hu, L. Developing fibrillated cellulose as a sustainable technological material. *Nature* **590**, 47–56 (2021).

87. Ansari, F., Sjöstedt, A., Larsson, P. T., Berglund, L. A. & Wågberg, L. Hierarchical wood cellulose fiber/epoxy biocomposites – Materials design of fiber porosity and nanostructure. *Compos Part A Appl Sci Manuf* **74**, 60–68 (2015).

88. Sood, A., Gupta, A. & Agrawal, G. Recent advances in polysaccharides based biomaterials for drug delivery and tissue engineering applications. *Carbohydrate Polymer Technologies and Applications* **2**, 100067 (2021).

89. Witzler, M., Büchner, D., Shoushrah, S. H., Babczyk, P., Baranova, J., Witzleben, S., Tobiasch, E., & Schulze, M. Polysaccharide-based systems for targeted stem cell differentiation and bone regeneration. *Biomolecules* **9**, (2019).

90. Seddiqi, H., Oliaei, E., Honarkar, H., Jin, J., Geonzon, L. C., Bacabac, R. G., & Klein-Nulend, J. Cellulose and its derivatives: towards biomedical applications. *Cellulose 2021 28:4* **28**, 1893–1931 (2021).

91. Leblanc Latour, M. & Pelling, A. E. Mechanosensitive osteogenesis on native cellulose scaffolds for bone tissue engineering. *J Biomech* **135**, 111030 (2022).

92. Dugan, J. M., Gough, J. E. & Eichhorn, S. J. Bacterial cellulose scaffolds and cellulose nanowhiskers for tissue engineering. *Nanomedicine* **8**, 287–299 (2013).

93. Pang, M., Huang, Y., Meng, F., Zhuang, Y., Liu, H., Du, M., Ma, Q., Wang, Q., Chen, Z., Chen, L., Cai, T., & Cai, Y. Application of bacterial cellulose in skin and bone tissue engineering. *Eur Polym J* **122**, 109365 (2020).

94. Jankau, J., Błażyńska-Spychalska, A., Kubiak, K., Jędrzejczak-Krzepkowska, M., Pankiewicz, T., Ludwicka, K., Dettlaff, A., & Pęksa, R. Bacterial Cellulose Properties Fulfilling Requirements for a Biomaterial of Choice in Reconstructive Surgery and Wound Healing. *Front Bioeng Biotechnol* **9**, 1492 (2022).

95. Chahal, S., Kumar, A. & Hussian, F. Development of biomimetic electrospun polymeric biomaterials for bone tissue engineering. A review. *Journal of biomaterials science.* **30**, 1308–1355 (2019).

96. Zaborowska, M., Bodin, A., Bäckdahl, H., Popp, J., Goldstein, A., & Gatenholm, P. Microporous bacterial cellulose as a potential scaffold for bone regeneration. *Acta Biomater* **6**, 2540–2547 (2010).

97. Dutta, S. D., Patel, D. K. & Lim, K. T. Functional cellulose-based hydrogels as extracellular matrices for tissue engineering. *Journal of Biological Engineering 2019 13:1* **13**, 1–19 (2019).

98. Singh, S., Dutt, D. & Mishra, N. C. Cotton pulp for bone tissue engineering. *J Biomater Sci Polym Ed* 2094–2113 (2020) doi:10.1080/09205063.2020.1793872.

99. Luo, W., Cheng, L., Yuan, C., Wu, Z., Yuan, G., Hou, M., Chen, J. Y., Luo, C., & Li, W. Preparation, characterization and evaluation of cellulose nanocrystal/poly(lactic acid) in situ nanocomposite scaffolds for tissue engineering. *Int J Biol Macromol* **134**, 469–479 (2019).

100. Abouzeid, R. E., Khiari, R., Beneventi, D. & Dufresne, A. Biomimetic Mineralization of Three-Dimensional Printed Alginate/TEMPO-Oxidized Cellulose Nanofibril Scaffolds for Bone Tissue Engineering. *Biomacromolecules* **19**, 4442–4452 (2018).

101. Courtenay, J. C., Filgueiras, J. G., Deazevedo, E. R., Jin, Y., Edler, K. J., Sharma, R. I., & Scott, J. L. Mechanically robust cationic cellulose nanofibril 3D scaffolds with tuneable biomimetic porosity for cell culture. *J Mater Chem B* **7**, 53–64 (2018).

102. Ran, J., Jiang, P., Liu, S., Sun, G., Yan, P., Shen, X., & Tong, H. Constructing multi-component organic/inorganic composite bacterial cellulose-gelatin/hydroxyapatite double-network scaffold platform for stem cell-mediated bone tissue engineering. *Materials Science and Engineering: C* **78**, 130–140 (2017).

103. Skerry, T. M. The response of bone to mechanical loading and disuse: Fundamental principles and influences on osteoblast/osteocyte homeostasis. *Arch Biochem Biophys* **473**, 117–123 (2008).

104. Reit, R., di Prima, M. & Voit, W. E. Overview of Mechanical Behavior of Materials. *Biomaterial Mechanics* 2–24 (2017) doi:10.1201/9781315152585-1/OVERVIEW-MECHANICAL-BEHAVIOR-MATERIALS-RADU-REIT-MATTHEW-DI-PRIMA-WALTER-VOIT.

105. Lautrup, B. Physics of Continuous Matter : Exotic and Everyday Phenomena in the Macroscopic World. *Physics of Continuous Matter* (2011) doi:10.1201/9781439894200.

106. Morrell, K. C., Hodge, W. A., Krebs, D. E. & Mann, R. W. Corroboration of in vivo cartilage pressures with implications for synovial joint tribology and osteoarthritis causation. *Proc Natl Acad Sci U S A* **102**, 14819–14824 (2005).

107. Zhang, D., Weinbaum, S. & Cowin, S. C. Estimates of the peak pressures in bone pore water. *J Biomech Eng* **120**, 697–703 (1998).

108. Brunelli, M., Perrault, C. & Lacroix, D. A Review of Bioreactors and Mechanical Stimuli. in 1–22 (Springer, Singapore, 2019). doi:10.1007/978-981-10-8075-3_1.

109. Pörtner, R., Nagel-Heyer, S., Goepfert, C., Adamietz, P. & Meenen, N. M. Bioreactor design for tissue engineering. *Journal of Bioscience and Bioengineering* vol. 100 235–245 Preprint at https://doi.org/10.1263/jbb.100.235 (2005).

110. Henstock, J. R., Rotherham, M., Rose, J. B. & el Haj, A. J. Cyclic hydrostatic pressure stimulates enhanced bone development in the foetal chick femur in vitro. *Bone* **53**, 468–477 (2013).

111. Reinwald, Y., Leonard, K. H. L., Henstock, J. R., Whiteley, J. P., Osborne, J. M., Waters, S. L., Levesque, P., & el Haj, A. J. Evaluation of the growth environment of a hydrostatic force bioreactor for preconditioning of tissue-engineered constructs. *Tissue Eng Part C Methods* **21**, 1–14 (2015).

112. Reinwald, Y. & el Haj, A. J. Hydrostatic pressure in combination with topographical cues affects the fate of bone marrow-derived human mesenchymal stem cells for bone tissue regeneration. *J Biomed Mater Res A* **106**, 629–640 (2018).

113. Zhao, Y. H., Lv, X., Liu, Y. L., Zhao, Y., Li, Q., Chen, Y. J., & Zhang, M. Hydrostatic pressure promotes the proliferation and osteogenic/chondrogenic differentiation of mesenchymal stem cells: The roles of RhoA and Rac1. *Stem Cell Res* **14**, 283–296 (2015).

114. Liu, C. Zhao, Y., Cheung, W. Y., Gandhi, R., Wang, L., & You, L. Effects of cyclic hydraulic pressure on osteocytes. *Bone* **46**, 1449–1456 (2010).

115. Gardinier, J. D., Majumdar, S., Duncan, R. L. & Wang, L. Cyclic hydraulic pressure and fluid flow differentially modulate cytoskeleton re-organization in MC3T3 osteoblasts. *Cell Mol Bioeng* **2**, 133–143 (2009).

116. Stavenschi, E., Corrigan, M. A., Johnson, G. P., Riffault, M. & Hoey, D. A. Physiological cyclic hydrostatic pressure induces osteogenic lineage commitment of human bone marrow stem cells: A systematic study. *Stem Cell Res Ther* **9**, (2018).

117. Oswald, Patrick. *Rheophysics : the deformation and flow of matter*. (Cambridge University Press, 2009).

118. Inoué, S. Foundations of confocal scanned imaging in light microscopy. in *Handbook of Biological Confocal Microscopy: Third Edition* 1–19 (Springer US, 2006). doi:10.1007/978-0-387-45524-2_1.

119. Lipson, A., Lipson, S. G. & Lipson, H. Optical Physics. *Optical Physics* (2010) doi:10.1017/CBO9780511763120.

120. Ginzberg, M. B., Kafri, R. & Kirschner, M. On being the right (cell) size. *Science* vol. 348 1245075 Preprint at https://doi.org/10.1126/science.1245075 (2015).

121. Owen, R. & Reilly, G. C. In vitro models of bone remodelling and associated disorders. *Front Bioeng Biotechnol* **6**, 134 (2018).

122. Wang, D., Christensen, K., Chawla, K., Xiao, G., Krebsbach, P. H., & Franceschi, R. T. Isolation and Characterization of MC3T3-E1 Preosteoblast Subclones with Distinct In Vitro and In Vivo Differentiation/Mineralization Potential. *Journal of Bone and Mineral Research* **14**, 893–903 (1999).

123. Addison, W. N., Nelea, V., Chicatun, F., Chien, Y.-C., Tran-Khanh, N., Buschmann, M. D., Nazhat, S. N., Kaartinen, M. T., Vali, H., Tecklenburg, M. M., Franceschi, R. T., & McKee, M. D. Extracellular matrix mineralization in murine MC3T3-E1 osteoblast cultures: An ultrastructural, compositional and comparative analysis with mouse bone. *Bone* **71**, 244–256 (2015).

124. Spicer, P. P., Kretlow, J. D., Young, S., Jansen, J. A., Kasper, F. K., & Mikos, A. G. Evaluation of bone regeneration using the rat critical size calvarial defect. *Nat Protoc* **7**, 1918–1929 (2012).

125. Vajgel, A., Mardas, N., Farias, B. C., Petrie, A., Cimões, R., & Donos, N. A systematic review on the critical size defect model. *Clin Oral Implants Res* **25**, 879–893 (2014).

126. Schmitz, J. P. & Hollinger, J. O. The critical size defect as an experimental model for craniomandibulofacial nonunions. *Clin Orthop Relat Res* 299–308 (1986).

127. Amini, A. R., Laurencin, C. T. & Nukavarapu, S. P. Bone tissue engineering: recent advances and challenges. *Crit Rev Biomed Eng* **40**, 363–408 (2012).

128. Butler, D. L., Goldstein, S. A. & Guilak, F. Functional tissue engineering: the role of biomechanics. *J Biomech Eng* **122**, 570–575 (2000).

129. Karageorgiou, V. & Kaplan, D. Porosity of 3D biomaterial scaffolds and osteogenesis. *Biomaterials* **26**, 5474–5491 (2005).

130. Bose, S., Roy, M. & Bandyopadhyay, A. Recent advances in bone tissue engineering scaffolds. *Trends Biotechnol* **30**, 546–554 (2012).

131. Fu, Q., Saiz, E., Rahaman, M. N. & Tomsia, A. P. Bioactive glass scaffolds for bone tissue engineering: state of the art and future perspectives. *Mater Sci Eng C Mater Biol Appl* **31**, 1245–1256 (2011).

132. Xynos, I. D., Edgar, A. J., Buttery, L. D. K., Hench, L. L. & Polak, J. M. Ionic Products of Bioactive Glass Dissolution Increase Proliferation of Human Osteoblasts and Induce Insulin-like Growth Factor II mRNA Expression and Protein Synthesis. *Biochem Biophys Res Commun* **276**, 461–465 (2000).

133. Kroeze, R., Helder, M., Govaert, L. & Smit, T. Biodegradable Polymers in Bone Tissue Engineering. *Materials* **2**, 833–856 (2009).

134. Zhao, J., Shen, G., Liu, C., Wang, S., Zhang, W., Zhang, X., Zhang, X., Ye, D., Wei, J., Zhang, Z., & Jiang, X. Enhanced Healing of Rat Calvarial Defects with Sulfated Chitosan-Coated Calcium-Deficient Hydroxyapatite/Bone Morphogenetic Protein 2 Scaffolds. *Tissue Eng Part A* **18**, 185–197 (2012).

135. Murtey, M. Das & Ramasamy, P. Sample Preparations for Scanning Electron Microscopy – Life Sciences. in *Modern Electron Microscopy in Physical and Life Sciences* 161–186 (InTech, 2016). doi:10.5772/61720.

136. Heary, R. F., Parvathreddy, N., Sampath, S. & Agarwal, N. Elastic modulus in the selection of interbody implants. *Journal of Spine Surgery* **3**, 163–167 (2017).

137. Sakkas, A., Wilde, F., Heufelder, M., Winter, K. & Schramm, A. Autogenous bone grafts in oral implantology—is it still a "gold standard"? A consecutive review of 279 patients with 456 clinical procedures. *Int J Implant Dent* **3**, (2017).

138. Nukavarapu, S. P., Freeman, J. W. & Laurencin, C. T. *Regenerative Engineering of Musculoskeletal Tissues and Interfaces*. *Regenerative Engineering of Musculoskeletal Tissues and Interfaces* (Elsevier Inc., 2015). doi:10.1016/C2014-0-02826-2.

139. Katiyar, A., Duncan, R. L. & Sarkar, K. Ultrasound stimulation increases proliferation of MC3T3-E1 preosteoblast-like cells. *J Ther Ultrasound* **2**, 1 (2014).

140. Zhou, X., Castro, N. J., Zhu, W., Cui, H., Aliabouzar, M., Sarkar, K., & Zhang, L. G. Improved Human Bone Marrow Mesenchymal Stem Cell Osteogenesis in 3D Bioprinted Tissue Scaffolds with Low Intensity Pulsed Ultrasound Stimulation. *Scientific Reports 2016 6:1* **6**, 1–12 (2016).

141. Aliabouzar, M., Zhang, L. G. & Sarkar, K. Lipid Coated Microbubbles and Low Intensity Pulsed Ultrasound Enhance Chondrogenesis of Human Mesenchymal Stem Cells in 3D Printed Scaffolds. *Scientific Reports 2016 6:1* **6**, 1–11 (2016).

142. Aliabouzar, M., Lee, S. J., Zhou, X., Zhang, G. L. & Sarkar, K. Effects of scaffold microstructure and low intensity pulsed ultrasound on chondrogenic differentiation of human mesenchymal stem cells. *Biotechnol Bioeng* **115**, 495–506 (2018).

143. Osborn, J., Aliabouzar, M., Zhou, X., Rao, R., Zhang, L. G., & Sarkar, K. Enhanced Osteogenic Differentiation of Human Mesenchymal Stem Cells Using Microbubbles and Low Intensity Pulsed Ultrasound on 3D Printed Scaffolds. *Adv Biosyst* **3**, (2019).

144. Minto, J., Zhou, X., Osborn, J., Zhang, L. G., Sarkar, K., & Rao, R. D. Three-Dimensional Printing: A Catalyst for a Changing Orthopaedic Landscape. *JBJS Rev* **8**, e0076–e0076 (2020).

145. Torgbo, S. & Sukyai, P. Bacterial cellulose-based scaffold materials for bone tissue engineering. *Appl Mater Today* **11**, 34–49 (2018).

146. Holmes, J. T., Jaberansari, Z., Collins, W., Leblanc Latour, M., Modulevsky, D. J., & Pelling, A. E. Homemade bread: Repurposing an ancient technology for in vitro tissue engineering. *Biomaterials* **280**, 121267 (2022).

147. Balasundari, R., Bishi, D. K., Mathapati, S., Naser, S. B., Cherian, K. M., & Guhathakurta, S. Nanocoated botanical scaffold in salvage for human tissue regeneration. *J Biomater Tissue Eng* **2**, 330–335 (2012).

148. Schindelin, J., Arganda-Carreras, I., Frise, E., Kaynig, V., Longair, M., Pietzsch, T., Preibisch, S., Rueden, C., Saalfeld, S., Schmid, B., Tinevez, J.-Y., White, D. J., Hartenstein, V., Eliceiri, K., Tomancak, P., & Cardona, A. Fiji: an open-source platform for biological-image analysis. *Nat Methods* **9**, 676–682 (2012).

149. Gregory, C. A., Gunn, W. G., Peister, A. & Prockop, D. J. An Alizarin red-based assay of mineralization by adherent cells in culture: Comparison with cetylpyridinium chloride extraction. *Anal Biochem* **329**, 77–84 (2004).

150. Vining, K. H. & Mooney, D. J. Mechanical forces direct stem cell behaviour in development and regeneration. *Nature Reviews Molecular Cell Biology* vol. 18 728–742 Preprint at https://doi.org/10.1038/nrm.2017.108 (2017).

151. Martino, F., Perestrelo, A. R., Vinarský, V., Pagliari, S. & Forte, G. Cellular mechanotransduction: From tension to function. *Frontiers in Physiology* vol. 9 Preprint at https://doi.org/10.3389/fphys.2018.00824 (2018).

152. Huang, C. & Ogawa, R. Effect of Hydrostatic Pressure on Bone Regeneration Using Human Mesenchymal Stem Cells. *Tissue Eng Part A* **18**, 2106–2113 (2012).

153. Gardinier, J. D., Gangadharan, V., Wang, L. & Duncan, R. L. Hydraulic pressure during fluid flow regulates purinergic signaling and cytoskeleton organization of osteoblasts. *Cell Mol Bioeng* **7**, 266–277 (2014).

154. Quarles, L. D., Yohay, D. A., Lever, L. W., Caton, R. & Wenstrup, R. J. Distinct proliferative and differentiated stages of murine MC3T3-E1 cells in culture: An in vitro model of osteoblast development. *Journal of Bone and Mineral Research* **7**, 683–692 (1992).

155. Hong, D., Chen, H. X., Yu, H. Q., Liang, Y., Wang, C., Lian, Q. Q., Deng, H. T., & Ge, R. S. Morphological and proteomic analysis of early stage of osteoblast differentiation in osteoblastic progenitor cells. *Exp Cell Res* **316**, 2291–2300 (2010).

156. Golub, E. E. & Boesze-Battaglia, K. The role of alkaline phosphatase in mineralization. *Curr Opin Orthop* **18**, 444–448 (2007).

157. Maharjan, B., Park, J., Kaliannagounder, V. K., Awasthi, G. P., Joshi, M. K., Park, C. H., & Kim, C. S. Regenerated cellulose nanofiber reinforced chitosan hydrogel scaffolds for bone tissue engineering. *Carbohydr Polym* **251**, 117023 (2021).

158. Kim, M., Yeo, M., Kim, M. & Kim, G. Biomimetic cellulose/calcium-deficient-hydroxyapatite composite scaffolds fabricated using an electric field for bone tissue engineering. *RSC Adv* **8**, 20637–20647 (2018).

159. Osborn, J., Aliabouzar, M., Zhou, X., Rao, R., Zhang, L. G., & Sarkar, K. Enhanced Osteogenic Differentiation of Human Mesenchymal Stem Cells Using Microbubbles and Low Intensity Pulsed Ultrasound on 3D Printed Scaffolds. *Adv Biosyst* **3**, (2019).

160. Burger, D., Beaumont, M., Rosenau, T. & Tamada, Y. Porous Silk Fibroin/Cellulose Hydrogels for Bone Tissue Engineering via a Novel Combined Process Based on Sequential Regeneration and Porogen Leaching. *Molecules 2020, Vol. 25, Page 5097* **25**, 5097 (2020).

161. Maharjan, B., Park, J., Kaliannagounder, V. K., Awasthi, G. P., Joshi, M. K., Park, C. H., & Kim, C. S. Regenerated cellulose nanofiber reinforced chitosan hydrogel scaffolds for bone tissue engineering. *Carbohydr Polym* **251**, 117023 (2021).

162. Mohammadi, H., Sepantafar, M., Muhamad, N. & Sulong, A. B. How Does Scaffold Porosity Conduct Bone Tissue Regeneration? *Adv Eng Mater* 2100463 (2021) doi:10.1002/ADEM.202100463.

163. Noè, C., Tonda-Turo, C., Chiappone, A., Sangermano, M. & Hakkarainen, M. Light Processable Starch Hydrogels. *Polymers 2020, Vol. 12, Page 1359* **12**, 1359 (2020).

164. Leblanc Latour, M. & Pelling, A. E. Mechanosensitive Osteogenesis on Native Cellulose Scaffolds for Bone Tissue Engineering. *bioRxiv* 2021.05.26.444470 (2022) doi:10.1101/2021.05.26.444470.

165. Kulbatski, I. Apples Lay the Foundation for Regenerating Bone. *The Scientist Magazine*® (2022).

166. Heinze, T. Cellulose: Structure and properties. *Advances in Polymer Science* **271**, 1–52 (2015).

167. Wang, J., Wang, L., Gardner, D. J., Shaler, S. M. & Cai, Z. Towards a cellulose-based society: opportunities and challenges. *Cellulose 2021 28:8* **28**, 4511–4543 (2021).

168. Bose, S., Koski, C. & Vu, A. A. Additive manufacturing of natural biopolymers and composites for bone tissue engineering. *Mater Horiz* **7**, 2011–2027 (2020).

169. Varma, D. M., Gold, G. T., Taub, P. J. & Nicoll, S. B. Injectable carboxymethylcellulose hydrogels for soft tissue filler applications. *Acta Biomater* **10**, 4996–5004 (2014).

170. Kim, S. H., Yeon, Y. K., Lee, J. M., Chao, J. R., Lee, Y. J., Seo, Y. B., Sultan, M. T., Lee, O. J., Lee, J. S., Yoon, S. il, Hong, I. S., Khang, G., Lee, S. J., Yoo, J. J., & Park, C. H. Precisely printable and biocompatible silk fibroin bioink for digital light processing 3D printing. *Nat Commun* **9**, 1–14 (2018).

171. Xiao, S., Zhao, T., Wang, J., Wang, C., Du, J., Ying, L., Lin, J., Zhang, C., Hu, W., Wang, L., & Xu, K. Gelatin Methacrylate (GelMA)-Based Hydrogels for Cell Transplantation: an Effective Strategy for Tissue Engineering. *Stem Cell Reviews and Reports 2019 15:5* **15**, 664–679 (2019).

172. Groszewicz, P. B., Mendes, P., Kumari, B., Lins, J., Biesalski, M., Gutmann, T., & Buntkowsky, G. N-Hydroxysuccinimide-activated esters as a functionalization agent for amino cellulose: synthesis and solid-state NMR characterization. *Cellulose* **27**, 1239–1254 (2020).

173. Schmidt, S., Liebert, T. & Heinze, T. Synthesis of soluble cellulose tosylates in an eco-friendly medium. *Green Chemistry* **16**, 1941–1946 (2014).

174. Celikkin, N., Mastrogiacomo, S., Jaroszewicz, J., Walboomers, X. F. & Swieszkowski, W. Gelatin methacrylate scaffold for bone tissue engineering: The influence of polymer concentration. *J Biomed Mater Res A* **106**, 201–209 (2018).

175. Li, W., Mille, L. S., Robledo, J. A., Uribe, T., Huerta, V., & Zhang, Y. S. Recent Advances in Formulating and Processing Biomaterial Inks for Vat Polymerization-Based 3D Printing. *Adv Healthc Mater* **9**, 2000156 (2020).

176. El Hamdaoui, L., Talbaoui, A. & El Moussaouiti, M. Nucleophilic Displacement Reaction on Tosyl Cellulose by L-Methionine to the Synthesis of Novel Water-Soluble Cellulose Derivative and Its Antibacterial Activity. *Int J Polym Sci* **2021**, (2021).

177. Schmidt, S., Liebert, T. & Heinze, T. Synthesis of soluble cellulose tosylates in an eco-friendly medium. *Green Chemistry* **16**, 1941–1946 (2014).

178. F, S., A, E., UR, T., MA, H., M, A., & F, A. Preparation and characterization of pH sensitive crosslinked Linseed polysaccharides-co-acrylic acid/methacrylic acid hydrogels for controlled delivery of ketoprofen. *Des Monomers Polym* **20**, 485–495 (2017).

179. Guilherme, M. R., Reis, A. v., Takahashi, S. H., Rubira, A. F., Feitosa, J. P. A., & Muniz, E. C. Synthesis of a novel superabsorbent hydrogel by copolymerization of acrylamide and cashew gum modified with glycidyl methacrylate. *Carbohydr Polym* **61**, 464–471 (2005).

180. Jaiswal, S., Dutta, P. K., Kumar, S., Koh, J. & Pandey, S. Methyl methacrylate modified chitosan: Synthesis, characterization and application in drug and gene delivery. *Carbohydr Polym* **211**, 109–117 (2019).

181. Grenier, J., Duval, H., Barou, F., Lv, P., David, B., & Letourneur, D. Mechanisms of pore formation in hydrogel scaffolds textured by freeze-drying. *Acta Biomater* **94**, 195–203 (2019).

182. Zhang, K., Fan, Y., Dunne, N. & Li, X. Effect of microporosity on scaffolds for bone tissue engineering. *Regen Biomater* **5**, 115–124 (2018).

183. QL, L. & C, C. Three-dimensional scaffolds for tissue engineering applications: role of porosity and pore size. *Tissue Eng Part B Rev* **19**, 485–502 (2013).

184. Leblanc Latour, M., Tarar, M., Hickey, R. J., Cuerrier, C. M., Catelas, I., & Pelling, A. E. Biomechanical study of cellulose scaffolds for bone tissue engineering in vivo and in vitro. *bioRxiv* 2021.07.07.451476 (2021) doi:10.1101/2021.07.07.451476.

185. Kuang, L., Ma, X., Ma, Y., Yao, Y., Tariq, M., Yuan, Y., & Liu, C. Self-Assembled Injectable Nanocomposite Hydrogels Coordinated by in Situ Generated CaP Nanoparticles for Bone Regeneration. *ACS Appl Mater Interfaces* **11**, 17234–17246 (2019).

186. Engler, A. J., Sen, S., Sweeney, H. L. & Discher, D. E. Matrix Elasticity Directs Stem Cell Lineage Specification. *Cell* **126**, 677–689 (2006).

187. Han, F., Zhu, C., Guo, Q., Yang, H. & Li, B. Cellular modulation by the elasticity of biomaterials. *J Mater Chem B* **4**, 9–26 (2015).

188. Lantigua, D., Wu, X., Suvarnapathaki, S., Nguyen, M. A. & Camci-Unal, G. Composite Scaffolds from Gelatin and Bone Meal Powder for Tissue Engineering. *Bioengineering 2021, Vol. 8, Page 169* **8**, 169 (2021).

189. Jeon, J., Lee, M. S. & Yang, H. S. Differentiated osteoblasts derived decellularized extracellular matrix to promote osteogenic differentiation. *Biomaterials Research 2018 22:1* **22**, 1–9 (2018).

190. Dutta, S. D., Hexiu, J., Patel, D. K., Ganguly, K. & Lim, K. T. 3D-printed bioactive and biodegradable hydrogel scaffolds of alginate/gelatin/cellulose nanocrystals for tissue engineering. *Int J Biol Macromol* **167**, 644–658 (2021).

191. Yilmaz, B., Pazarceviren, A. E., Tezcaner, A. & Evis, Z. Historical development of simulated body fluids used in biomedical applications: A review. *Microchemical Journal* **155**, 104713 (2020).

192. Guo, J. L., Kim, Y. S., Orchard, E. A., van den Beucken, J. J. J. P., Jansen, J. A., Wong, M. E., & Mikos, A. G. A Rabbit Femoral Condyle Defect Model for Assessment of Osteochondral Tissue Regeneration. *Tissue Eng Part C Methods* **26**, 554–564 (2020).

193. Stammers, T. Organ Trafficking: Why Do Healthcare Workers Engage in It? *Cambridge Quarterly of Healthcare Ethics* **31**, 368–378 (2022).

194. Gonzalez, J., Garijo, I. & Sanchez, A. Organ Trafficking and Migration: A Bibliometric Analysis of an Untold Story. *Int J Environ Res Public Health* **17**, 3204 (2020).